

INSTITUTE FOR FUSION STUDIES

DOE/ET-53088-580

IFSR #580

Drift Wave Coherent Vortex Structures
in Inhomogeneous Plasmas

XIANG NING SU
Institute for Fusion Studies
The University of Texas at Austin
Austin, Texas 78712

(THESIS)

November 1992

THE UNIVERSITY OF TEXAS



AUSTIN

DRIFT WAVE COHERENT VORTEX STRUCTURES
IN INHOMOGENEOUS PLASMAS

APPROVED BY

DISSERTATION COMMITTEE:

Wendell Horton

Philip J. Morrison

Al C

J B Swift

Darryl L. Winney

W. L. ...

**DRIFT WAVE COHERENT VORTEX STRUCTURES
IN INHOMOGENEOUS PLASMAS**

APPROVED BY
DISSERTATION COMMITTEE:

Claude W. Horton, Jr.

Philip J. Morrison

Toshiki Tajima

Jack B. Swift

Harry L. Swinney

Victor G. Szebehely

Dedicated to my parents and brothers

**DRIFT WAVE COHERENT VORTEX STRUCTURES
IN INHOMOGENEOUS PLASMAS**

by

XIANG NING SU, B.A.

DISSERTATION

Presented to the Faculty of the Graduate School of
The University of Texas at Austin
in Partial Fulfillment
of the Requirements
for the Degree of

DOCTOR OF PHILOSOPHY

THE UNIVERSITY OF TEXAS AT AUSTIN

December, 1992

Acknowledgments

I gratefully thank Professor Wendell Horton and Professor Philip J. Morrison for their guidance and assistance throughout the years of my study at the Institute for Fusion Studies. It has been a great privilege and rewarding experience to collaborate with and learn from them. I have greatly benefited from their expertise and experience, and I deeply appreciate their time and effort that made this dissertation possible.

I would like to thank Professors Jack Swift, Harry Swinney, Toshiaki Tajima and Victor Szebehely for offering their precious time to read my dissertation and serve as my committee members.

I wish to express special thanks to my friends Lois Fangyi Cai, Tom Chang in Los Angeles, Chris Kueny in IFS of UT, and Xiaolin Wang in EE department of UT for their warm friendship, generous helps, and many interesting and useful talking and discussions on various subjects over the years that have made my life much interesting and easier.

I wish to express my gratitude to my friends, colleagues and/or fellow graduate students at the Institute for Fusion Studies: R. Acevedo, Dr. S. Cable, M. Calvin, D. del Castillo, Bo Chen, Dr. X.L. Chen, J.Q. Dong, Dr. G.Y. Fu, J. Hernandez, R. Kinney, Dr. J. Koga, Dr. W.Q. Lee, Dr. J.X. Liu, M.G. Prahovic, H. Xiao, Dr. H.C. Ye, X.D. Zhang, and Dr. Y.Z. Zhang for many useful discussions over the years.

I would like to thank the faculty and/or staff members at the Institute

of Fusion Studies, especially, Dr. James Van Dam, Professor R. D. Hazeltine, Professor H. L. Berk and the secretaries D. Allen, S. Crumley, J. Gillette, J. Patton, S. Stewart, and C. Valentine for providing me various conveniences during my stay in Austin.

I would also like to thank L. Lee and D. Lindberg for many helps and assistance on numerical computation and A.Y. Aydemir, J. Dibble, A. Macmahon, and W.H. Miner for computer advice.

I want to acknowledge financial support from the Institute for Fusion Studies.

I thank my uncle, aunt and cousins for their helps and support during my years of study in Los Angeles.

Finally, I wish to thank my parents, and my brothers and their families for their love, support and understanding throughout all these years.

Xiang Ning Su

The University of Texas at Austin

December, 1992

DRIFT WAVE COHERENT VORTEX STRUCTURES IN INHOMOGENEOUS PLASMAS

Publication No. _____

Xiang Ning Su, Ph.D.

The University of Texas at Austin, 1992

Supervisor: Wendell Horton

Nonlinear drift wave vortex structures in magnetized plasmas are studied theoretically and numerically in the various physical environments.

The effects of density and temperature gradients on drift wave vortex dynamics are analyzed using a fully nonlinear model with the Boltzmann density distribution. The equation, based on the full Boltzmann relation, possesses no localized monopole solution in the short wavelength ($\sim \rho_s$) region, while in the longer wavelength ($\sim (\rho_s r_n)^{1/2}$) region the density profile governs the existence of monopole-like solutions. In the longer wavelength regime, however, the monopoles can not be localized sufficiently to avoid coupling to propagating drift waves due to the inhomogeneity of the plasma. Thus, the monopole vortex is a long lived coherent structure, but it is not precisely a stationary structure since the coupling results in a “flapping” tail. The tail causes energy

of the vortex to leak out, but the effect of the temperature gradient is to reduce the leaking of this energy.

Nonlinear coherent structures governed by the coupled drift wave – ion acoustic mode equations in sheared magnetic field are studied analytically and numerically. A solitary vortex equation that includes the effects of density and temperature gradients and magnetic shear is derived and analyzed. The results show that for a plasma in a sheared magnetic field, there exist the solitary vortex solutions; however, the solutions are not exponentially localized due to the presence of oscillating tail that connects to the core of the vortex. The new vortex structures are dipole-like in their symmetry, but not the modon type of dipoles. The numerical simulations are performed in 2-D with the coupled vorticity and parallel mass flow equations.

The vortex structures in an unstable drift wave system driven by parallel shear flow are studied. The linear instability is analyzed. The nonlinear solitary vortex solutions are given and the formation of the vortices from a turbulent state is observed from the numerical simulations. A scenario for the self-organization processes in the turbulent state has been established. The effect of magnetic shear on the self-organization process is also investigated.

Table of Contents

Acknowledgments	iv
Table of Contents	viii
List of Tables	xi
List of Figures	xii
Chapter 1. Introduction	1
§1.1 Historical Review and Overview	1
§1.2 Analogy between Rossby Waves and Drift Waves	5
§1.3 The Drift Wave Mechanism and Vortex	7
Chapter 2. Effect of Temperature Gradient Induced KdV Non-linearity on the Modon Vortex Solution	11
§2.1 Introduction	11
§2.2 Model Equation and Conservation Laws	13
§2.3 Exact Monopole Solutions	16
§2.4 Dipole Vortex Splitting into Monopoles	21
§2.5 Summary and Conclusions	29
Chapter 3. Drift Wave Vortices in a Plasma with Temperature Gradient and Drift Velocity Shear	31
§3.1 Introduction	31
§3.2 Model Equation of Drift Wave in Inhomogeneous Plasma	33

§3.3	Traveling Wave Equation and Solutions	36
§3.4	Interaction of Vortices with Drift Sheared Flow and the Formation of Monopole Vortices	47
§3.5	Radiation Damping of Solitary Drift Wave Vortex in Inhomogeneous Plasmas	50
§3.6	Numerical Simulations	56
§3.7	Summary and Conclusions	62
 Chapter 4. Nonlinear Drift Wave Coherent Structures in a Sheared Magnetic Field		64
§4.1	Introduction	64
§4.2	Theoretical Model and Conservations	66
§4.3	Analytical Stationary Solitary Wave Solutions	69
§4.4	Properties of the Coherent Structures in Sheared Magnetic Field	81
§4.5	Numerical Simulation Results	86
§4.6	Conclusion	94
 Chapter 5. Formation of Drift Wave Vortices in Parallel Shear Flow Driven Turbulence		96
§5.1	Introduction	96
§5.2	Dynamical Equations and Analysis of Linear Instability	98
§5.3	Solitary Vortex Solutions	101
§5.4	The Simulations	110
§5.4.1	Local case	110
§5.4.2	Nonlocal case	120
§5.5	Summary and Discussion	126
 Appendix A. Noncanonical Hamiltonian Structure		128

List of Tables

1.1	Analogy between drift wave and Rossby wave	6
-----	--	---

List of Figures

1.1	The demonstration of drift wave mechanism.	8
1.2	Dispersion and self-binding of a drift wave monopole vortex . .	10
2.1	Plot of the solitary wave solution of Eq. (2.9)	19
2.2	Solution of Eq. (2.9) with $\psi'(0) = 0$	20
2.3	Splitting drift wave dipole vortex into monopoles	25
2.4	Splitting dipole vortex without vector nonlinearity	27
2.5	One-dimensional solitary wave traveling along the y -axis tears with finite k_x and forms two-dimensional solitary waves.	28
3.1	Stationary monopole solution given in Eq. (3.26) for $v'_{a0} = 0.05$ and $u = 1.5$	42
3.2	Nearly elastic overtaking collision of a strong monopole vortex with a weaker monopole vortex.	44
3.3	Point vortex type of interaction of two strong monopole vortices.	45
3.4	Interaction of dipole vortex with drift shear flow.	49
3.5	Configuration of sheared flow.	50
3.6	Interaction of vortex with sheared flow	51
3.7	Contour plot of the electrostatic potential $\varphi(x, y, t)$ with strong radiation damping.	59

3.8	Contour plot of the electrostatic potential $\varphi(x, y, t)$ with weak damping.	60
3.9	Monopole vortex with a radiation wake.	61
4.1	Evolution of effective potential $V_{\text{eff}}(\Psi, t)$ with the “time” t	74
4.2	Evolution of the separatrix in phase space corresponding to the effective potential $V_{\text{eff}}(\Psi, t)$	75
4.3	A typical nonlinear eigenfunction with magnetic shear.	78
4.4	Spectrum of critical $d\Psi(t = 0)/dt$ versus the effective shear s from 0 to 0.1.	80
4.5	Comparison between the 1-D and 2-D numerical solutions with $s = 1$	82
4.6	Drift wave – Ion acoustic wave vortex in a sheared magnetic field for $s = 1$	83
4.7	Contour plots of the electrostatic potential $\varphi(x, y, t)$ and parallel velocity $v_{\parallel}(x, y, t)$ with magnetic shear parameter $S_m = 0.1 (s \simeq 0.07)$, drift velocity gradient $v'_{d0} = 0$ and $R_E \sim 7$	90
4.8	Contour plots of the electrostatic potential $\varphi(x, y, t)$ and parallel velocity $v_{\parallel}(x, y, t)$ with the parameters same as in Fig. 4.7, but $R_E \ll 1$	91
4.9	Interaction of the new dipole vortex presented in Sec. 4.3 with drift sheared flow.	92
4.10	Radiation damping of the new vortex structure when $s \sim 1$ or $ u/v_d - 1 \sim S_1$	93

5.1	The growth rates $\gamma(k)(r_n/c_s)$ versus $k_y\rho_s$ for given $k_x\rho_s = 0-5$ in the case of $v'_{0\parallel} = 0, 7$, $S_0 = 0.2$ and $\sigma = 0.01$	102
5.2	The stable and unstable regions in $S_0-v'_{0\parallel}$ space for the mode $k_x\rho_s = 0$, $k_y\rho_s = 2.6$ with $\sigma = 0.01$	103
5.3	3-D and contour plots of the stationary dipole vortex solutions given in Eqs. (5.19) and (5.23) for $u = -0.4$, $r_0 = 16$, $v'_{0\parallel} = 0.7$ and $S_0 = 0.2$	107
5.4	Plot of speed u versus S_0 for $v'_{0\parallel} = 0.7$	108
5.5	Plot of speed u versus $v'_{0\parallel}$ for $S_0 = 0.2$	109
5.6	The time evolution of the contours of electric potential $\delta\varphi(x, y, t)$ for $v'_{0\parallel} = 0.7$, $B_y/B_0 = S_0 = 0.2$, $\mu_{\perp} = 0.01$, and $\nu_{\perp} = 0.02$	113
5.7	The time evolution of the contours of parallel velocity $\delta v_{\parallel}(x, y, t)$ for $v'_{0\parallel} = 0.7$, $B_y/B_0 = S_0 = 0.2$, $\mu_{\perp} = 0.01$, and $\nu_{\perp} = 0.02$	114
5.8	The time evolution of the contours of electric potential $\delta\varphi(x, y, t)$ for $v'_{0\parallel} = 0.6$, $B_y/B_0 = S_0 = 0.2$, and $\mu_{\perp} = \nu_{\perp} = 0.01$	116
5.9	The time evolution of the contours of parallel velocity $\delta v_{\parallel}(x, y, t)$ for $v'_{0\parallel} = 0.6$, $B_y/B_0 = S_0 = 0.2$, and $\mu_{\perp} = \nu_{\perp} = 0.01$	117
5.10	The wavenumber spectra of the time average total energy for a early time interval $50 \leq tc_s/r_n \leq 250$ and a later time interval $2250 \leq tc_s/r_n \leq 2500$ for the case in Figs. (5.8) and (5.9).	119
5.11	The time evolution of the contours of electric potential $\delta\varphi(x, y, t)$ for $v'_{0\parallel} = 0.6$, $B_y/B_0 = 0.4 \sin(2\pi x/L_x)$, and $\mu_{\perp} = \nu_{\perp} = 0.01$. . .	122

5.12	The time evolution of the contours of parallel velocity $\delta v_{\parallel}(x, y, t)$ for $v'_{0\parallel} = 0.6$, $B_y/B_0 = 0.4 \sin(2\pi x/L_x)$, and $\mu_{\perp} = \nu_{\perp} = 0.01$. . .	123
5.13	The time evolution of the energies for $v'_{0\parallel} = 0.6$, $B_y/B_0 =$ $0.4 \sin(2\pi x/L_x)$, and $\mu_{\perp} = \nu_{\perp} = 0.01$	124
5.14	The time evolution of the energies for $v'_{0\parallel} = 0.6$, $B_y/B_0 = S_0 =$ 0.2 , and $\mu_{\perp} = \nu_{\perp} = 0.01$	125

Chapter 1

Introduction

1.1 Historical Review and Overview

For decades, the fluid in a rotating environment has attracted a great deal of attention from many geophysicists and astrophysicists. It was J. G. Charney [1948] who first studied the low frequency dynamics of the atmospheric and oceanographic planetary waves on a rotating planet with planetary rotational frequency being much higher than the wave frequency. He derived the so-called Charney equation in geophysics. The planetary waves described by the Charney equation are called Rossby waves, named after the Swedish geophysicist C. G. Rossby, who first showed that the waves play an important role in global atmospheric circulation process [Rossby, 1939]. The Charney equation, which is also called the barotropic vorticity equation, has an exact, localized, and finite amplitude solution first found by Larichev and Reznik [1976]. This solution also is called a modon and has the form of a stationary dipole vortex traveling in the direction perpendicular to the equilibrium inhomogeneity. The solitary vortex structures have been observed in the oceans and in planetary atmospheres, for instance, synoptic vortices in the earth's oceans and so called blocking structures in the atmospheres. The most phenomenal example of a localized long-lived planetary vortex is the Great Red Spot on Jupiter. This atmospheric vortex, which is significantly larger than the earth in diameter, has been observed for about 300 years. In terms of 10.5 hours day

of Jupiter this is a life time of 250285 rotations. The vortices also have been successfully simulated in many rotating water tank experiments in laboratory [Philips, 1965; Platzman, 1968; Holton, 1971; Antipov *et al.*, 1982 and 1983; Nezlin, 1986; Sommeria *et al.*, 1988; Meyers *et al.*, 1989].

In 1977, Hasegawa and Mima noticed the similarity between the Rossby wave in the atmosphere and the drift wave in magnetized plasmas and derived the so-called Hasegawa-Mima equation [Hasegawa and Mima, 1977 and 1978; Hasegawa *et al.*, 1979]. The H-M equation has exactly the same form as that of Charney equation. Physically the drift waves in a spatially non-uniform magnetized plasma are analogous to the Rossby waves. The analogy will be demonstrated in the next section of this chapter. It is perhaps to be expected from this analogy that the Rossby wave vortices observed in nature and experiments should exist in a magnetized plasma.

Since finding the modon solution for the Charney-Hasegawa-Mima equation, many physicists have found similar modon solutions for various collective modes in magnetically confined plasma [Makino *et al.*, 1981; Taniuti and Hasegawa, 1982; Meiss and Horton, 1983; Pavlenko and Petviashvili, 1983; Mikhailovski *et al.*, 1984; Shukla *et al.*, 1985; Horton *et al.*, 1986; Liu and Horton, 1986]. However the systems dealt with in all these works are homogeneous or quasi-homogeneous plasma systems. In the late sixty's, Buchel'nikova *et al.* [1967] and Hendel *et al.* [1968] experimentally showed that for low temperature plasmas ($T \leq 1 \text{ ev}$) produced under the condition of Q-machine the development of the drift wave instabilities results in regular drift wave structures of a form of saw-toothed shape like a train of solitons. However the experimentally observed drift wave structures appear to be monopole vortex

form. These observations can only be explained in an inhomogeneous plasma system. Petviashvili [1977] analyzed the nonlinear drift wave with the inclusion of a temperature gradient and showed that the monopole solitary solution can be found when the temperature gradient is included. It follows, from his works, that the necessary condition for the existence of such monopole structures is the presence of an electron temperature gradient. However the Buchel'nikova *et al.* [1967] and Hendel *et al.* [1968] experiments showed that such monopole vortex structures still exist in the absence of the temperature gradient. (In the Q-machine the uniformly heated end plate maintains constant electron temperature over the radius of the plate.) This paradox remained unsolved until about 10 years later. In 1987, Lakhin *et al.* [1987 and 1988] and Hori-hata *et al.* [1987] carefully studied Petviashvili's model [Petviashvili, 1977] and found that the model is incomplete and inconsistent with Ertel's theorem [Ertel, 1942; Pedlosky, 1979], the basic conservation law of potential vorticity. The authors showed that monopole vortices exist only when the drift velocity is non-constant, that is, has spatial variation. The spatial variation of the drift velocity adds a shear to the diamagnetic drift velocity and the shear flow causes the formation of monopole vortices.

However all the previous works failed to consider the effect of the coupling between the vortex and propagating drift waves. The coupling is a natural result of the inhomogeneity in the plasma. In this dissertation, the author will extend the previous theory, study the mechanism of formation of monopole vortices, and re-investigate the effect of inhomogeneities in the plasma on the drift wave vortices, especially the coupling between the vortex and the propagating drift waves.

For a long time, the effect of magnetic shear on vortex has been considered a difficult problem. In 1983, Meiss and Horton [1983] have studied the problem. However they considered the weak magnetic sheared field limit and treated the shear as a linear exterior perturbation to the vortex structure. In fact, even though there are many nonlinear vortex solutions for various collective modes today, there are still no solutions that include the magnetic shear of order unity. In this dissertation, the author will explore the problem theoretically and numerically and give a new coherent vortex structure governed by the coupled drift wave and ion acoustic wave equations in non-uniform plasmas with sheared magnetic fields.

The dynamics of nonlinear drift waves has been subject of intensive studies since these waves are regarded as responsible for the anomalous transport in plasmas. Hasegawa and Mima used the H-M model [Hasegawa and Mima, 1977 and 1978] to explain the high level of density fluctuations and the broad frequency spectrum observed in a tokamak [Surko and Slusher, 1978]. Since then, many properties of drift wave turbulence have been revealed: the spectrum evolution is characterized by an inverse cascade [Hasegawa and Wakatani, 1983], and the wavenumber spectrum of energy obeys the Kraichnan k^{-3} law [Kraichnan, 1967], as examples.

On the other hand, the H-M equation, as stated earlier, has exact dipole vortex solution referred to modons. These modons have been shown to be fairly stable against collisions and perturbations [Makino *et al.*, 1981; Seyler *et al.*, 1975]. Thus the H-M equation is anticipated to link strong turbulence to self-organized motions. Similar phenomena of the self-organization have been demonstrated in two-dimensional hydrodynamic turbulence [Seyler *et al.*, 1975;

Hasegawa, 1983] and in MHD turbulence [Montgomery *et al.*, 1978; Hassian *et al.*, 1985]. Another approach to the description of the drift wave turbulence was given in Horton [1976], in which the dissipation in the electron response provides both the sources of the turbulence through the dissipating drift wave instability and the nonlinear saturation through the so-called $\mathbf{E} \times \mathbf{B}$ nonlinearity in the continuity equation. The dissipative drift wave turbulence is analyzed in Horton [1986] where it is shown that the structures of dissipationless H-M type are recovered when the dissipation parameter ($i\delta_k$) vanishes (or becomes sufficiently weak).

In this dissertation, the author will pursue the subject and study the formation of a coherent vortex structure through turbulence in the course of the nonlinear development of the toroidal or parallel shear flow driven instabilities.

1.2 Analogy between Rossby Waves and Drift Waves

There is a profound analogy between Rossby waves in shallow rotating fluids and drift waves in plasmas, confined transversely by a strong longitudinal magnetic field. In the dissipationless limit the basic model equation for drift waves in plasmas is the Hasegawa-Mima equation, given by Eq. (2.1) in the next chapter. The same basic nonlinear wave equation describes the slow, nearly incompressible motions of shallow rotating fluids. In the case of drift waves the Lorentz force plays a role analogous to that of the Coriolis force on rotating system. The fundamental correspondence follows from low frequency disturbances where the vector cross-product forms of the accelerations, $\mathbf{V} \times \mathbf{B}$ and $2\mathbf{V} \times \boldsymbol{\Omega}$, respectively, dominate the dynamics. The drift waves appear as a result of the transverse (relative to the magnetic field) non-uniformity of the

Table 1.1: Analogy between drift wave and Rossby wave

Drift Wave	Rossby Wave
H-M equation: $(1 - \nabla^2) \frac{\partial \varphi}{\partial t} + v_d \frac{\partial \varphi}{\partial y} - [\varphi, \nabla^2 \varphi] = 0$	Charney equation: $(1 - \nabla^2) \frac{\partial h}{\partial t} + v_R \frac{\partial h}{\partial y} - [h, \nabla^2 h] = 0$
Electrostatic potential: $\varphi(x, y, t)$ $\varphi(x, y, t) = (\frac{r_n}{\rho_s}) e \Phi(\frac{x}{\rho_s}, \frac{y}{\rho_s}, \frac{c_s t}{r_n}) / T_e$	Variable part of fluid depth: $h(x, y, t)$ $h(x, y, t) = (\frac{L_R}{\rho_R}) \delta h(\frac{x}{\rho_R}, \frac{y}{\rho_R}, \frac{c_g t}{L_R}) / H$
Lorentz force: $m_i \omega_{ci} \mathbf{v}_\perp \times \hat{\mathbf{z}}$	Coriolis force: $\rho f \mathbf{v}_\perp \times \hat{\mathbf{z}}$
$\mathbf{E} \times \mathbf{B}$ drift flow: $\mathbf{V}_\perp = (\frac{c}{B}) \hat{\mathbf{z}} \times \nabla \Phi$	Geostrophic flow: $\mathbf{V}_\perp = (\frac{g}{f}) \hat{\mathbf{z}} \times \nabla \delta h$
Cyclotron frequency: $\omega_{ci} = \frac{eB}{cm_i}$	Coriolis parameter: f
Drift coefficient: $r_n^{-1} = -\frac{\partial}{\partial x} \ln n_0$	Rossby coefficient: $L_R^{-1} = \frac{\partial}{\partial x} \ln(\frac{f}{H})$
Larmor radius: $\rho_s = \frac{c_s}{\omega_{ci}}$	Rossby radius: $\rho_R = \frac{c_g}{f}$
Ion acoustic speed: $c_s = (\frac{T_e}{m_i})^{1/2}$ where T_e is electron temperature.	Gravity wave speed: $c_g = (gH)^{1/2}$ where H is depth of fluid layer.
Drift velocity: $v_d = c_s \rho_s \frac{\partial}{\partial x} \ln n_0$	Rossby velocity: $v_R = c_g \rho_R \frac{\partial}{\partial x} \ln(\frac{f}{H})$
Dispersion relation: $\omega = \frac{k_y v_d}{1 + k^2 \rho_s^2}$	Dispersion relation: $\omega = \frac{k_y v_R}{1 + k^2 \rho_R^2}$

electron temperature or plasma density, just like Rossby waves appear owing to the transverse (relative to the local angular rotation velocity Ω of the system) non-uniformity of the Coriolis parameter $f = 2\Omega \cdot \hat{z}$ or depth of the fluid H . The spatial scale of the dispersion of drift waves is the “Larmor radius, ρ_s , of the ions at the electron temperature,” analogous to the Rossby radius ρ_R , and equal to the ratio of the ion acoustic speed c_s to the ion cyclotron frequency ω_{ci} , while the ω_{ci} is analogous to the Coriolis parameter f . Here the ion acoustic speed c_s is analogous to the gravity wave speed c_g . The analogy of the drift velocity v_d is the characteristic Rossby velocity v_R . Based on these facts, it is understandable that the dispersion relation for drift waves is analogous to the relation for Rossby waves.

It follows from the indicated analogy between the two types of waves that, analogously to the hydrodynamic Rossby solitary vortices observed experimentally, the drift wave solitary vortices should also exist in a magnetized plasma. The detail correspondences of the analogy are listed in Table 1.1. It should be noted that in plasma physics the direction of inhomogeneity is taken in x , while in geophysics it is taken in y .

1.3 The Drift Wave Mechanism and Vortex

To illustrate the drift wave mechanism, we consider a dense and collisionless ion column confined in a constant and uniform magnetic field $\mathbf{B} = B_0 \hat{z}$ as shown in Fig. 1.1. The positive charged ion column causes a radial electric field $\mathbf{E} = -\nabla\Phi$. The background plasma has density gradient along negative x -direction. The radial electric field \mathbf{E} and the magnetic field \mathbf{B} cause the ion column to produce a $\mathbf{E} \times \mathbf{B}$ rotation $\mathbf{V}_{\mathbf{E} \times \mathbf{B}} = (c/B_0^2)\mathbf{E} \times \mathbf{B}$ around the axis of

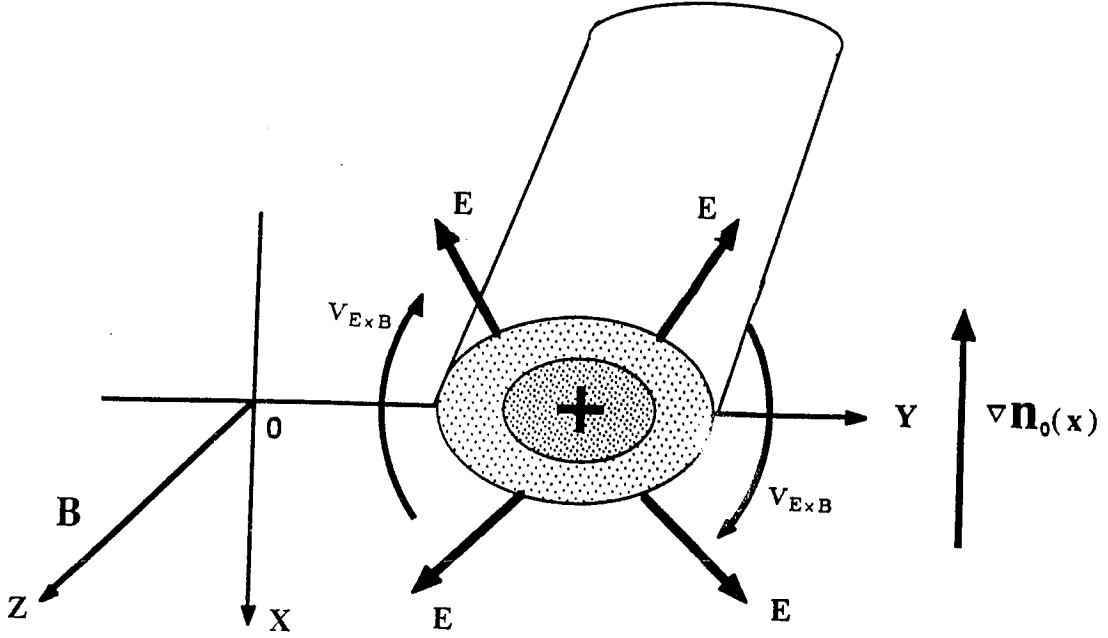


Figure 1.1: The demonstration of drift wave mechanism.

the column. The rotation rate can be calculated by $\Omega_E = (c/B_0)k_x k_y \Phi_k$ for a structure characterized by wave numbers (k_x, k_y) and amplitude Φ_k . We call this rotation rate characteristic nonlinear frequency since it depends on the amplitude of Φ_k , the electric potential of the structure of size π/k .

On the other hand, the non-uniform background plasma causes linear drift waves that propagate along the y-direction and have linear drift wave frequency $\omega_k = k_y v_d / (1 + k^2 \rho_s^2)$. The ratio of the nonlinear frequency or vortex rotation rate Ω_E to the linear frequency ω_k is defined as the dissipationless $\mathbf{E} \times \mathbf{B}$ Reynolds number R_E and is given by

$$R_E = \frac{\Omega_E(k)}{\omega_k} \simeq k_x r_n \left(\frac{e\Phi_k}{T_e} \right).$$

Therefore it is understandable that when $R_E < 1$, the dispersion of the wave packet dominates and only when $R_E \geq 1$ vortex structures can be formed.

Figure 1.2 is an example comparing the linear $R_E \ll 1$ behavior with the strong nonlinear $R_E \sim 10 \gg 1$ propagation of the same size initial disturbance which clearly shows the self-binding effect. Figure 1.2 shows that in contrast to small amplitude drift waves that spread out and lose strength as they travel as seen in Fig. 1.2(a), the solitary drift wave vortices are coherent, self-sustaining packets that retain their strength over long time intervals and distances as they travel as seen in Fig. 1.2(b).

The most commonly seen vortex structures are monopole and dipole vortices. The monopole vortex represents a net excess in the local charge density and is the natural, finite amplitude solution in the presence of a sheared flow, and the dipole vortex represents a local charge polarization in the local plasma density and is the natural, finite amplitude solution in the absence of a sheared flow. The dipole is usually seen to be produced in the turbulent wake of a 2-D fluid flowing past an obstacle and can be also formed through pairing or coupling of two monopole vortices with opposite rotational orientation [Couder and Basdevant 1986; Horton 1989]. The properties and interactions of both the monopole and dipole vortices have been studied previously by many authors [Seyler *et al.*, 1975; Makino *et al.*, 1981; McWilliams and Zabusky, 1982; Horton, 1989]. It is believed that the interactions of the long-lived and particle-trapping vortex structures play an important role in anomalous transport of plasmas.

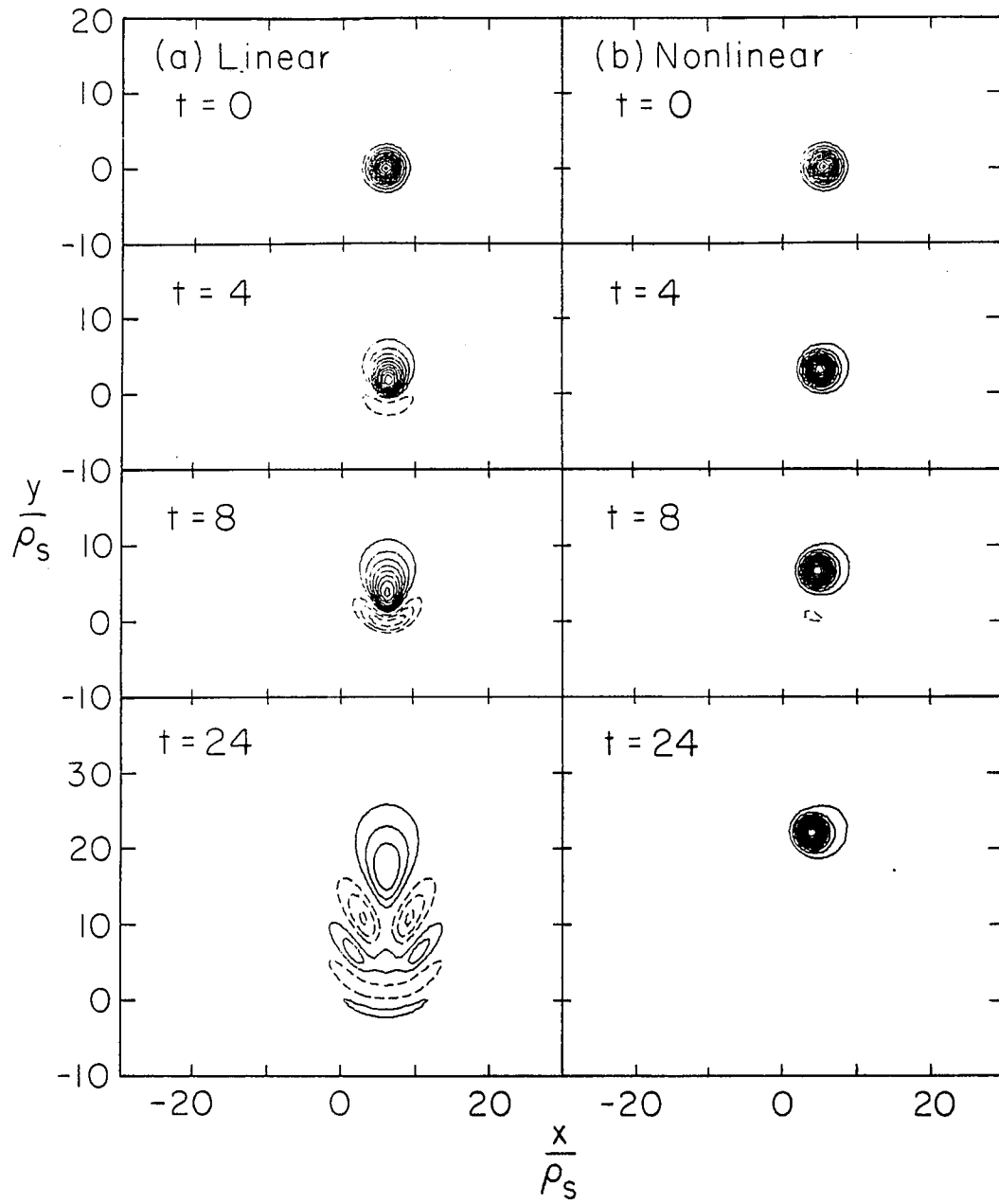


Figure 1.2: Dispersion and self-binding of a drift wave monopole vortex
 (a) Dispersion propagation in the linear regime with $R_E \ll 1$. (b) Self-binding in the nonlinear regime with $R_E \sim 10$.

Chapter 2

Effect of Temperature Gradient Induced KdV Nonlinearity on the Modon Vortex Solution

2.1 Introduction

It is well known that the dipole vortex is an exact solitary wave solution to the dissipationless Hasegawa-Mima (H-M) drift wave equation [Hasegawa and Mima, 1977 and 1978], which in the fluid mechanics literature is referred to as the Rossby wave equation

$$(1 - \nabla^2) \frac{\partial \varphi}{\partial t} + v_d \frac{\partial \varphi}{\partial y} - [\varphi, \nabla^2 \varphi] = 0 \quad (2.1)$$

where

$$[\varphi, \nabla^2 \varphi] = \frac{\partial \varphi}{\partial x} \frac{\partial \nabla^2 \varphi}{\partial y} - \frac{\partial \varphi}{\partial y} \frac{\partial \nabla^2 \varphi}{\partial x}$$

is the Jacobian between the electrostatic potential φ and the vorticity $\zeta = \nabla^2 \varphi$. The Jacobian is also called as the Poisson-bracket or vector nonlinearity. This type of nonlinearity is known to facilitate the formation of robust monopole and dipole vortices [Makino, 1981]. Recently, there have been numerous studies of this type of nonlinearity and the resulting vortex dynamics [Makino *et al.*, 1981; Taniuti and Hasegawa, 1982; Meiss and Horton, 1983; Pavlenko and Petviashvili, 1983; Mikhailovski *et al.*, 1984; Shukla *et al.*, 1985; Horton *et al.*, 1986; Liu and Horton, 1986]. However, a more comprehensive theory

includes the nonlinearity as given in Eq. (2.1), together with KdV or scalar type nonlinearity, a term proportional to $\varphi \partial\varphi/\partial y$ as given in Eq. (2.2) in the next section which was first introduced by Petviashvili [1977] in the case of drift waves. The Petviashvili model has recently been criticized by several authors [Lakhin *et al.*, 1987 and 1988; Horiata and Sato, 1987; Laedke and Spatschek, 1988; Nycander, 1989] because of a lack of consistency with Ertel's theorem [Ertel, 1942], the basic conservation law of potential vorticity of the flow. This issue will be addressed in Chapter 3. But more recently, Spatschek *et al.* [1990] used a new space/time scale ordering and amplitude scaling to develop a model that has the same form as the Petviashvili model. Therefore it is worthwhile to use the Petviashvili model to further study vortex dynamics since this model is simple and clear for investigation and demonstration of the effect of scalar or KdV nonlinearity on the dipole vortex and the stability of the dipole vortex structures. In this chapter, we will use the model to investigate how this scalar nonlinearity affects the evolution of the dipole vortex. Due to the presence of the scalar nonlinearity, the dipole vortex is no longer an exact solution. We will analytically and numerically show that the modon-type vortices of Larichev and Reznik [1976] are structurally unstable to the addition of a small amount of the scalar or KdV nonlinearity which arises from the electron temperature gradient. We will demonstrate numerically that even a small amount of the scalar nonlinearity can have important consequences for the vortices.

Hydrodynamic experiments by many scientists [Antipov *et al.*, 1982 and 1983; Nezlin, 1986] have shown that there is a rather rapid transition from a dipole vortex pair to isolated monopole vortices. This transition we argue

arises as a result of the competition between the vector and the scalar nonlinearities. From the analogy between the Coriolis force dynamics describing Rossby waves [Rossby, 1939] in rotating hydrodynamics and the Lorentz force dynamics describing drift waves in a magnetized, inhomogeneous plasma, we expect that the splitting process of the dipole vortex into monopoles should also occur in a plasma for solitary drift waves. It is, therefore, worthwhile to numerically simulate the dynamics of dipole vortices incorporating a small scalar nonlinearity, and thus to investigate how the scalar nonlinearity splits up the dipole.

This chapter is organized as follows: in Sec. 2.2, we give the equation of the simulation model and present its conservation laws. Exact monopole solutions are presented in Sec. 2.3. In Sec. 2.4, we describe how the dipole vortex splits up and give simulation results on the evolution when the dipole vortex pair is the initial state. Section 2.5 gives the summary and the conclusions for Chapter 2.

2.2 Model Equation and Conservation Laws

We consider a plasma in a uniform external magnetic field in the z -direction. The gradients in plasma density $d\ln n_0/dx$ and the electron temperature $\eta_e = d\ln T_e/d\ln n_e$ are along the x -axis, the diamagnetic drift velocity $v_d = -(cT_e/eB_0)d\ln n_0/dx$ is along the y -axis. To describe the dynamics of the potential drift waves in such a plasma, we consider the contribution of the electron and ion polarization drifts to the density equation and we use the

condition of quasi-neutrality of perturbations. One can thus derive the following simplified model equation [Petviashvili, 1977 and 1980; Williams, 1978 and 1985]

$$(1 - \nabla^2) \frac{\partial \varphi}{\partial t} + v_d \frac{\partial \varphi}{\partial y} + \alpha \varphi \frac{\partial \varphi}{\partial y} + [\nabla^2 \varphi, \varphi] = 0 \quad (2.2)$$

where $\alpha = v_d \eta_e = \rho_s / r_{T_e}$, $\varphi = e\Phi / T_e$, Φ is electric potential in volts, ρ_s is the ion Larmor radius with electron temperature T_e , r_{T_e} is the characteristic length of the plasma temperature inhomogeneity, space and time variables are normalized by ρ_s and the ion cyclotron frequency, respectively. All the terms in Eq. (2.2) except the KdV term $\alpha \varphi \partial \varphi / \partial y$ are order of unity and the $\alpha \varphi \partial \varphi / \partial y$ term is order of ρ_s / r_{T_e} . The analyses in the later sections of this chapter shows that existence of a small amount of KdV term makes the dipole vortex solutions of H-M equation structurally unstable and gives rise to a new type of vortices, the monopole vortices. Therefore, as a consequence, the KdV term is kept in Eq. (2.2). For $\alpha \rightarrow 0$ the time scale associated with the nonlinear dynamics from the KdV term becomes long as $t_{KdV} \sim v_d / \alpha \varphi_{\max}$. For sufficiently small α this time scale can be longer than the lifetime of the experiment or the viscous damping time scale.

Rossby waves in rapidly rotating shallow neutral fluids also satisfy Eq. (2.2) with the scalar nonlinearity which arises from variations in the depth of the fluid and the $[\nabla^2 \varphi, \varphi]$ nonlinearity which arises from the convective acceleration $\mathbf{v} \cdot \nabla \mathbf{v}$ of the fluid.

For weakly inhomogeneous plasma, ρ_s / r_{T_e} is small compared to unity and thus the scalar nonlinearity, i.e. the α term is typically neglected, where-

upon Eq. (2.2) reduces to Eq. (2.1). If we keep the scalar nonlinearity, then the dipole vortex is no longer an exact solution. For small ρ_s/r_{Te} , however, the dipole vortex is a good solution over short period of time. In the following we show that this small α term splits the dipole vortex into two monopoles of opposite sign.

Consider now the conservation laws of Eq. (2.2) after the scalar nonlinearity is added.

1. Equation (2.2) can be rewritten as

$$\frac{\partial \varphi}{\partial t} + \nabla \cdot \left[-\frac{\partial \nabla \varphi}{\partial t} + \left(v_d \varphi + \frac{\alpha \varphi^2}{2} \right) \hat{y} + (\nabla \varphi \times \hat{z}) \nabla^2 \varphi \right] = 0 \quad (2.3)$$

Equation (2.3) represents the conservation of mass in the two-dimensional system. The net excess mass is proportional to $\int \varphi dx dy$.

2. Multiplying Eq. (2.2) by φ , we derive the following equation

$$\frac{\partial \varepsilon}{\partial t} + \nabla \cdot \left[\left(\frac{1}{2} v_d \varphi^2 + \frac{1}{3} \alpha \varphi^3 \right) \hat{y} - \varphi \nabla \frac{\partial \varphi}{\partial t} - \nabla^2 \varphi \left(\hat{z} \times \nabla \frac{\varphi^2}{2} \right) \right] = 0 \quad (2.4)$$

where

$$\varepsilon(x, y, t) = \frac{1}{2} [\varphi^2 + (\nabla \varphi)^2]$$

is the local energy density. Equation (2.4) gives the energy conservation law.

3. Multiplying Eq. (2.2) by x , we get another constant of motion,

$$\begin{aligned} \frac{\partial(x\varphi)}{\partial t} + \nabla \cdot \left[\left(\frac{\partial \varphi}{\partial t} \right) \hat{x} + \left[x \left(v_d \varphi + \frac{\alpha \varphi^2}{2} \right) + \frac{|\nabla \varphi|^2}{2} \right] \hat{y} - \frac{\partial \varphi}{\partial y} \nabla \varphi \right. \\ \left. - \frac{\partial(x \nabla \varphi)}{\partial t} + x(\nabla \varphi \times \hat{z}) \nabla^2 \varphi \right] = 0 \end{aligned} \quad (2.5)$$

giving the conservation law for the x coordinate for the center of mass.

The above three constants of motion are used in the simulation to observe the accuracy of the numerical integration of Eq. (2.2).

We also notice that the conservation of the potential enstrophy which is defined as

$$U = \langle (\nabla\varphi)^2 + (\nabla^2\varphi)^2 \rangle$$

is broken for $\alpha \neq 0$. Here we use the angular bracket $\langle \dots \rangle$ to define the area integral over the relevant domain,

$$\langle F \rangle = \int \int dx dy F(x, y) .$$

In some cases it is convenient to normalize the area integral.

2.3 Exact Monopole Solutions

In order to interpret our results we first present exact monopole solutions to Eq. (2.2). Assuming a traveling steady-state solution $\varphi = \varphi(x, y - ut)$, Eq. (2.2) becomes

$$-u(1 - \nabla^2) \frac{\partial \varphi}{\partial y} + v_d \frac{\partial \varphi}{\partial y} + \alpha \varphi \frac{\partial \varphi}{\partial y} + [\nabla^2 \varphi, \varphi] = 0 . \quad (2.6)$$

For axisymmetric monopoles, $\varphi(r, \theta) \rightarrow \varphi(r)$ and $[\varphi(r), \nabla^2 \varphi(r)] = 0$, leaving

$$\frac{1}{r} \frac{d}{dr} \left(r \frac{d\varphi}{dr} \right) = 4k^2 \varphi - \frac{\alpha}{2u} \varphi^2 \quad (2.7)$$

where

$$k^2 = \frac{1}{4} \left(1 - \frac{v_d}{u} \right) . \quad (2.8)$$

(Introducing of the factor 4 is , of cause, somewhat arbitrary. We follow this convention since it was introduced in the literature.) Defining $\varphi = \varphi_m \psi(\xi)$, where $\xi = kr$, Eq. (2.7) becomes the following in terms of ψ :

$$\frac{d^2\psi}{d\xi^2} + \frac{1}{\xi} \frac{d\psi}{d\xi} = 4\psi - 6\gamma\psi^2. \quad (2.9)$$

Here we have set

$$\varphi_m = \frac{12\gamma uk^2}{\alpha} \quad (2.10)$$

where γ is a constant that remains to be determined.

We compare Eq. (2.9) to the analogous equation for one-dimensional solitary drift waves that are solutions of the regularized long-wave equation [Meiss and Horton, 1982; Morrison *et al.*, 1984],

$$\phi_t - \phi_{yyt} + v_d \phi_y + \alpha \phi \phi_y = 0. \quad (2.11)$$

This equation is the one-dimensional restriction of Eq. (2.2). Inserting $\varphi = \varphi_m \psi(k(y - ut))$ yields

$$\frac{d^2\psi}{d\xi^2} = 4\psi - 6\psi^2 \quad (2.12)$$

where $\xi \equiv k(y - ut)$, $k^2 = \frac{1}{4}(1 - v_d/u)$ and $\varphi_m = 12uk^2/\alpha$. For $k^2 > 0$ Eq. (2.12) possesses the well-known soliton solution

$$\psi = \text{sech}^2 \xi.$$

It is apparent that the monopole speed-width relation, Eq. (2.8), is identical with that for the one-dimensional case. But, the amplitude relation of Eq. (2.10) differs by the presence of γ , which also occurs in Eq. (2.9), the

equation for the shape of the monopole. This later equation, together with the boundary conditions

$$\frac{d\psi}{d\xi}(\xi = 0) = 0 \quad , \quad \lim_{\xi \rightarrow \infty} \frac{1}{\psi} \frac{d\psi}{d\xi} = -2 \quad (2.13)$$

and the condition $\psi(\xi = 0) = 1$ defines a nonlinear eigenvalue problem for γ . Physically, the eigenvalue is the amplitude of the monopole. Numerically we obtain $\gamma = 1.5946$; the shape of the eigenfunction defined by this procedure is shown in Fig. 2.1. In our computations we set γ to unity and then vary the value of ψ and $d\psi/d\xi$ at large values of ξ , consistent with the second equality of Eq. (2.13), until $d\psi(\xi = 0)/d\xi = 0$ is achieved. This yields $\psi(\xi = 0) = \gamma$. Finally, scaling $\psi(\xi = 0)$ by γ then gives the desired result.

The above calculation is only valid for $k^2 > 0$, which implies $u > v_d$ or $uv_d < 0$. In light of Eq. (2.10) positive velocity ($uv_d > 0$) monopoles have $\varphi_m > 0$. These are called anticyclones since they are regions of high density and pressure. The negative ($uv_d < 0$) velocity monopoles have negative φ_m and are called cyclones and have low pressure center. In the case $k^2 < 0$ neither the two-dimensional Eq. (2.9) nor the one-dimensional Eq. (2.12) possess exponentially localized solutions. When $k^2 < 0$ the wave structure propagates energy with speed u where $0 < u < v_d$, and in two-dimensions, there is a weakly localized oscillatory (outgoing radiation) solution where the amplitude decays as $\xi^{-1/2}$ to conserve the flux of wave energy in two-dimension.

In Fig. 2.2 we plot solutions to Eq. (2.9). All of these solutions have $d\psi(\xi = 0)/d\xi = 0$. For $\psi(\xi = 0) > \gamma$ the solution diverges to $-\infty$. Solutions with $0 < \psi(\xi = 0) \lesssim \gamma$ are homoclinic to $\psi = 2/3$. These nonlinear

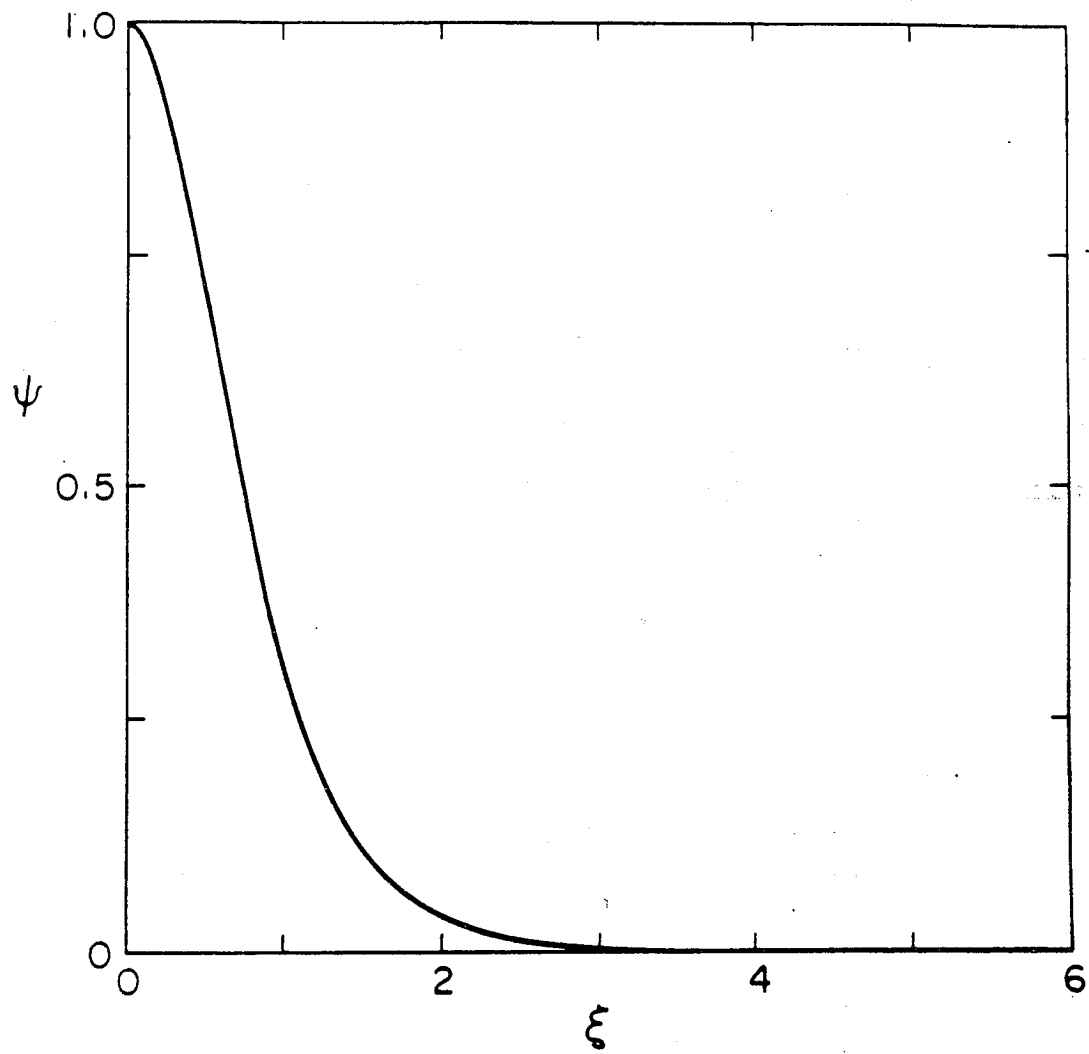


Figure 2.1: Plot of the solitary wave solution of Eq. (2.9)

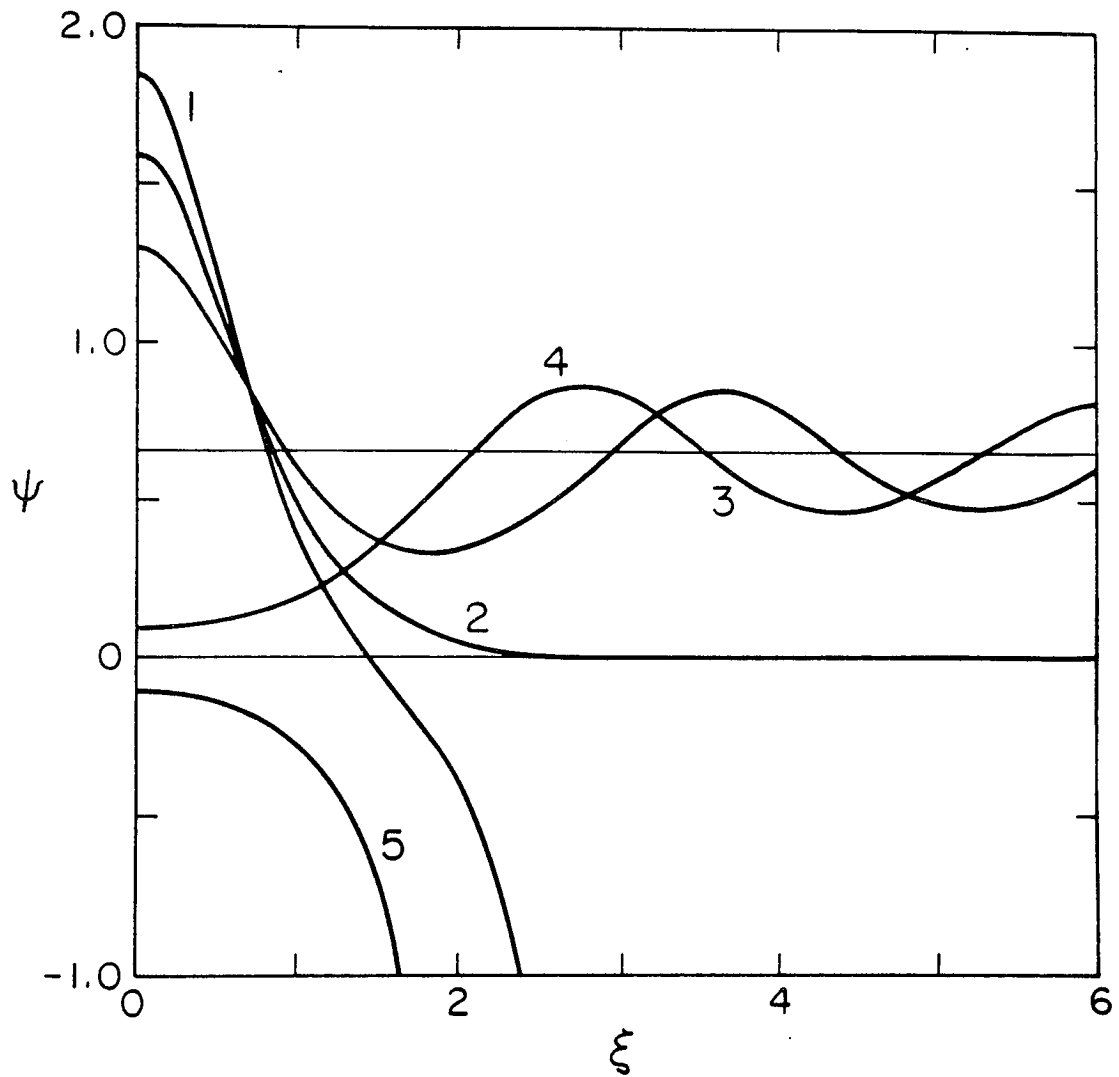


Figure 2.2: Solution of Eq. (2.9) with $\psi'(0) = 0$

Curve 1 has $\psi(0) = 1.85$. Curve 2 has $\psi(0) = \gamma$ (as in Fig. 2.1); it is homoclinic to zero: $\psi(r = \infty) = 0$. Curves 3 and 4 have $\psi(0) = 1.3$ and $\psi(0) = 0.1$, respectively. These, like all solutions with $\gamma > \psi(0) > 0$, are homoclinic to $2/3$. When lowered by $2/3$ these represent wave-like or radiation solutions. Curve 5 has $\psi(0) = -0.1$.

oscillatory solutions are the radiation solutions mentioned above and describe finite amplitude cylindrically symmetric waves propagating with speed u such that $0 < u < v_d$, that is, $k^2 < 0$. Mathematically, these finite amplitude wave solutions can be “pulled down” by the following symmetry relation:

$$\bar{\varphi}(-k^2; r, \theta) = \varphi(k^2; r, \theta) - \frac{8uk^2}{\alpha}.$$

If φ solves $\nabla^2\varphi - 4k^2\varphi + \alpha\varphi^2/2u = 0$, then $\bar{\varphi}$ solves $\nabla^2\bar{\varphi} + 4k^2\bar{\varphi} + \alpha\bar{\varphi}^2/2u = 0$. Thus, Fig. 2.2 compactly displays both the localized solitary wave and the finite amplitude radiation solutions.

Additional symmetries of Eqs. (2.1) and (2.2) are as follows: For every solution of Eq. (2.1) $\varphi(x, y, t)$ there is a solution — $\varphi(-x, y, t)$ (i.e., Eq. (2.1) has the symmetry $\varphi(x, y, t) \rightarrow -\varphi(-x, y, t)$.) This symmetry is lost when the scalar nonlinearity is added to the equation. This antisymmetry in x is the property possessed by the dipole vortex solution given in Eq. (2.14). When the scalar nonlinearity is added there is no symmetry for a given α , but for the two different equations with α and $-\alpha$ there is the symmetry relation

$$\varphi(-\alpha; x, y, t) = -\varphi(\alpha, -x, y, t) :$$

Thus a small, finite α lifts a degeneracy in the $\alpha = 0$ equation.

2.4 Dipole Vortex Splitting into Monopoles

The dipole vortex solution [Larichev and Reznik, 1976; Flierl *et al.*, 1980] possessed by Eq. (2.1) in the absence of scalar nonlinearity ($\alpha = 0$) is

given by

$$\varphi = \begin{cases} \left[-\frac{k^2 r_0}{p^2 r} \frac{J_1(pr)}{J_1(pr_0)} + \left(1 + \frac{k^2}{p^2} \right) \right] ur \cos \theta & (r < r_0) \\ u r_0 \frac{K_1(kr)}{K_1(kr_0)} \cos \theta & (r > r_0) \end{cases} \quad (2.14)$$

where $r^2 = x^2 + (y - ut)^2$, $u = v_d/(1 - k^2)$, $x = r \cos \theta$, and $y = r \sin \theta$. The parameters p and k are related by

$$\frac{1}{kr_0} \frac{K_2(kr_0)}{K_1(kr_0)} = -\frac{1}{pr_0} \frac{J_2(pr_0)}{J_1(pr_0)},$$

which follows from continuity of the flow velocity $\mathbf{v} = \hat{\mathbf{z}} \times \nabla \varphi$ across $r = r_0$.

Previous simulation studies of Eq. (2.2) by Mikhailovskaya [1986], with Eq. (2.14) as the initial state, indicate that when $\alpha \neq 0$, the dipole vortex rapidly separates into pieces moving in opposite directions away from their initial positions. The radius of the anticyclones ($\varphi > 0$) increases slightly, but the amplitude decreases and approaches a circular shape. Cyclones ($\varphi < 0$), are observed to gradually decay into small vortices that finally disappear.

We find a different result. From our calculation and simulations, we conclude that when $\alpha \neq 0$, the dipole vortex pair splits into *both* the anticyclone and the cyclone monopoles, which maintain their integrity.

In order to interpret our results and to understand the discrepancy with Mikhailovskaya's results [Mikhailovskaya, 1986] we use the amplitude and width-speed relations defined by Eq. (2.10) of Sec. 2.3. From Eqs. (2.8) and (2.10) we obtain the following speed for anticyclones:

$$u = v_d + \frac{\alpha |\varphi_m|}{3\gamma} \quad (2.15)$$

while for cyclones, $\varphi_m < 0$, and the speed is given by

$$u = v_d - \frac{\alpha|\varphi_m|}{3\gamma} \quad (2.16)$$

where exponential localization requires $\alpha|\varphi_m| > 3\gamma v_d$. The anticyclone and cyclone propagate with different speeds, the relative speed is

$$u_+ - u_- = \alpha|\varphi_m^+|/(3\gamma) + \alpha|\varphi_m^-|/(3\gamma) .$$

This result explains why the initial dipole vortex pair will split apart into two isolated monopoles with opposite signs. The time scale for the breakup of the dipole vortex can be estimated from

$$\Delta t \sim 3r_0\gamma/(2\alpha|\varphi_m|) . \quad (2.17)$$

This relation is observed by our simulations.

To solve Eq. (2.2), we use high order Runge-Kutta time stepping and the Fourier transformation $(x, y) \leftrightarrow (k_x, k_y)$ at each time step on a uniform grid over k_x and k_y in 85×85 k-space with 3612 complex $\varphi_{\mathbf{k}}(t)$ modes using the 128×128 FFT. The constants of motion in Sec. 2.2 are used to monitor the accuracy of the numerical integration of Eq. (2.2). They, in fact, remain constant within the fraction 10^{-3} during the simulation experiments. The initial perturbation $\varphi(x, y, 0)$ is taken to be the dipole vortex given in Eq.-(2.14) with $r_0 = 6(\rho_s)$, $u = 2v_d$ and $v_d = c_s\rho_s/r_n$. Typical simulations use twenty minutes CPU on the CRAY-2 for $\Delta t = 100 r_n/c_s$.

We studied two cases with $\alpha = 0.01$ and $\alpha = 0.1$, and observed the same results, except that the time scale of breakup for $\alpha = 0.01$ is about 10 times larger than that for $\alpha = 0.1$.

Figure 2.3 shows the streamlines $\varphi(x, y, t) = \text{const.}$ at times $tc_s/r_n = 0, 2, 10$, and 100 . Observe that at $tc_s/r_n = 10$, the initial dipole vortex splits into the two completely isolated monopoles and the two monopoles approach circular shape. We also observed that the amplitudes of the vortices increases slightly, but the radius of both the vortices does not change much until $t \simeq 30$. The observed speed of the anticyclone is $u \simeq 2.0v_d$ and that of the cyclone is $u \simeq -0.3v_d$, and amplitude of the anticyclone is $\varphi_m^+ \simeq 52$ and that of the cyclone, $\varphi_m^- \simeq -62$. These results agree with the analytical results Eq. (2.10) obtained in Sec. 2.3.

Moreover, when we turn off the vector nonlinearity and re-do the same experiment, we observed that the radius of the cyclone decreases significantly very rapidly and its amplitude increases a significant amount and then forms a very localized monopole vortex or solitary wave, while the radius of the anticyclone doesn't change much and its amplitude increases slightly. The evolution of the processes are illustrated by Fig. 2.4. In the case of an anticyclone, this result appears to be in accordance with the simulation studies of Eq. (2.2) made by Pavlenko and Tazanov [1986] in the long wavelength limit.

Now we consider whether the anticyclone and cyclones can naturally evolve from the one-dimensional solitary waves described by Eq. (2.12).

For $k_x \approx 0$, we know that Eq. (2.2) has the one-dimensional solitary wave solution given by Petviashvili [1977], Meiss and Horton [1982] and Morrison *et al.* [1984]

$$\varphi = \frac{3}{\alpha}(u - v_d)\text{sech}^2 \left[\frac{1}{2} \left(1 - \frac{v_d}{u} \right)^{1/2} (y - ut) \right], \quad (2.18)$$

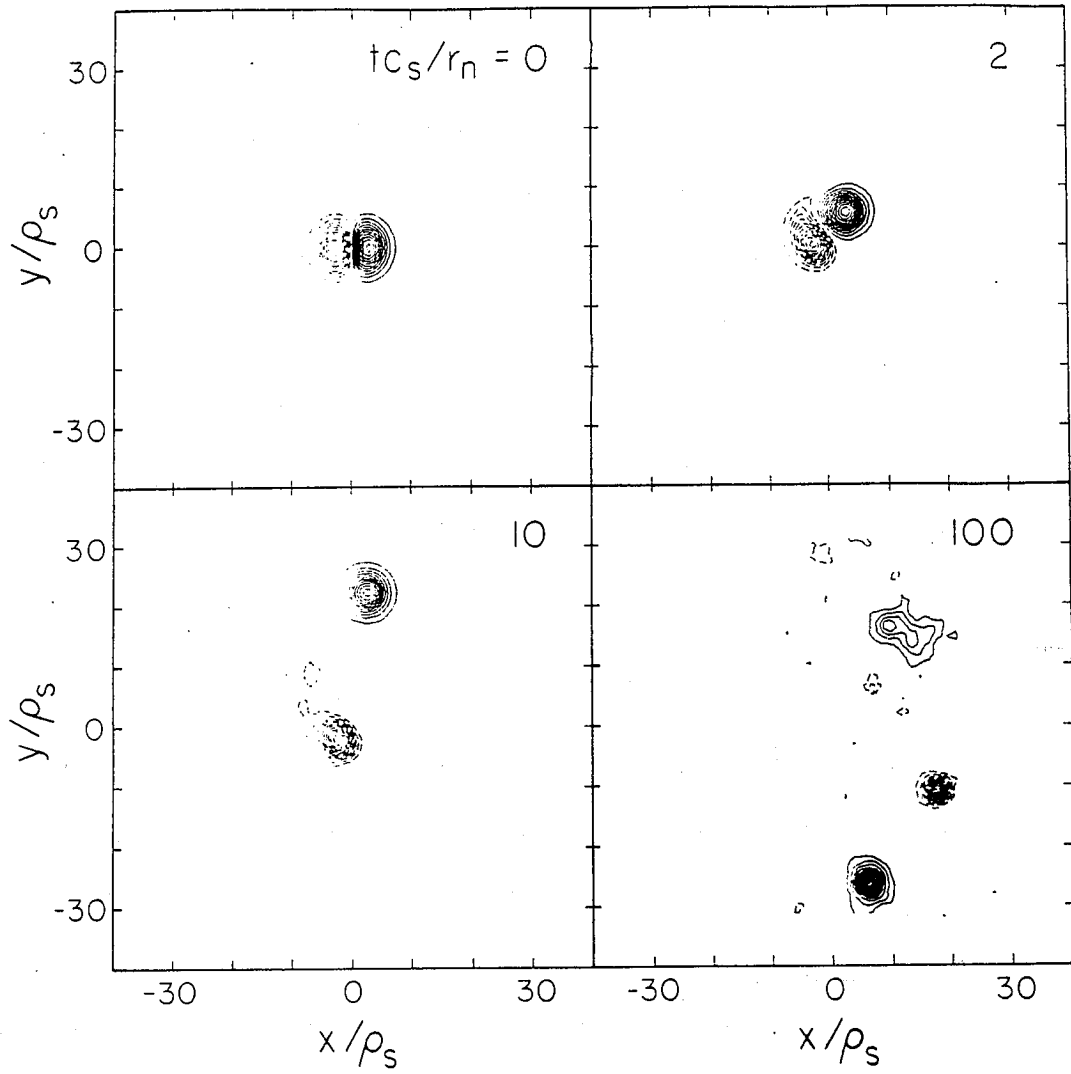


Figure 2.3: Splitting drift wave dipole vortex into monopoles

Dipole radius $r_0 = 6\rho_s$, amplitude of scalar nonlinearity $\alpha = 0.1 (\eta_e \rho_s / r_n)$, and vortex velocity $u = 2v_d$ ($v_d = 1$). At $t = 0$, (a) shows the contours for the exact dipole vortex solution, Eq.(2.14), of Hasegawa-Mima—Rossby wave Eq. (2.1). The solid lines represent positive value of potential φ , and the dashed lines, negative value. The contours for φ have contour interval $\Delta\varphi = 4.0$.

where u , as before, is the speed of the solitary wave.

However, the one-dimensional solitary wave is unstable to a finite k_x filamentation instability shown as follows. Taking Eq. (2.18) as the initial condition, we find that computer solution of Eq. (2.2), without the vector non-linearity, evolves to the two-dimensional, nearly circular symmetric monopole vortices. The results are shown in Fig. 2.5.

The solution (2.18) is possible only when $u > v_d$ or $v_d u < 0$. For $u > v_d$, we find that the positive solitary wave eventually evolves into two-dimensional anticyclones, as shown in Fig. 2.5. For $u < 0$, we also find that the negative solitary wave,

$$\varphi = -\frac{3}{\alpha}(|u| + v_d) \operatorname{sech}^2 \left(\frac{\sqrt{1 + \frac{v_d}{|u|}}}{2} y \right) \quad (2.19)$$

evolves into two-dimensional cyclones with $k_x \sim k_y$. From Eq. (2.16), we can see that $\varphi_m < 0$ occurs for $\alpha|\varphi_m|/3\gamma > v_d$ where $u < 0$. With Eq. (2.19) as initial data, we find that cyclones evolve out of the one-dimensional negative solitary wave.

As noted in Sec. 2.4, Mikhailovskaya [1986] did some simulation studies of Eq. (2.2). Her results indicate that when α is large enough, that is, the scalar nonlinearity is dominant, the dipole vortex rapidly separates with monopoles moving in opposite directions away from their initial positions. The radius of anticyclones ($\varphi > 0$) increase slightly. The amplitude decreases and it approaches a circular shape, but cyclones ($\varphi < 0$), they find, gradually decay into small vortices and finally disappear. In general, we find a different result, both theoretically and numerically.

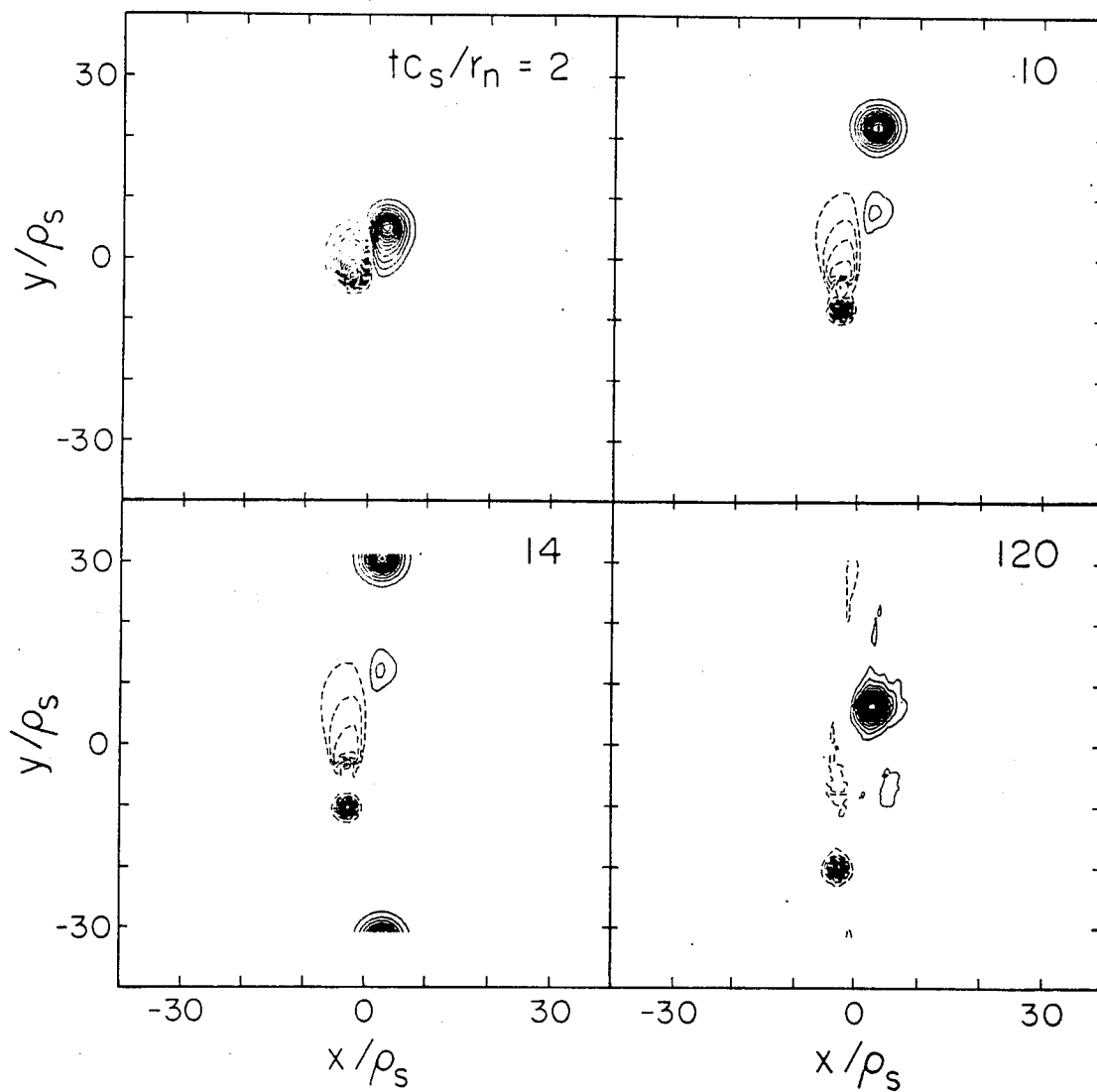


Figure 2.4: Splitting dipole vortex without vector nonlinearity

Everything is the same as in Fig. 2.3, except that the vector nonlinear term in Eq. (2.2) is dropped out.

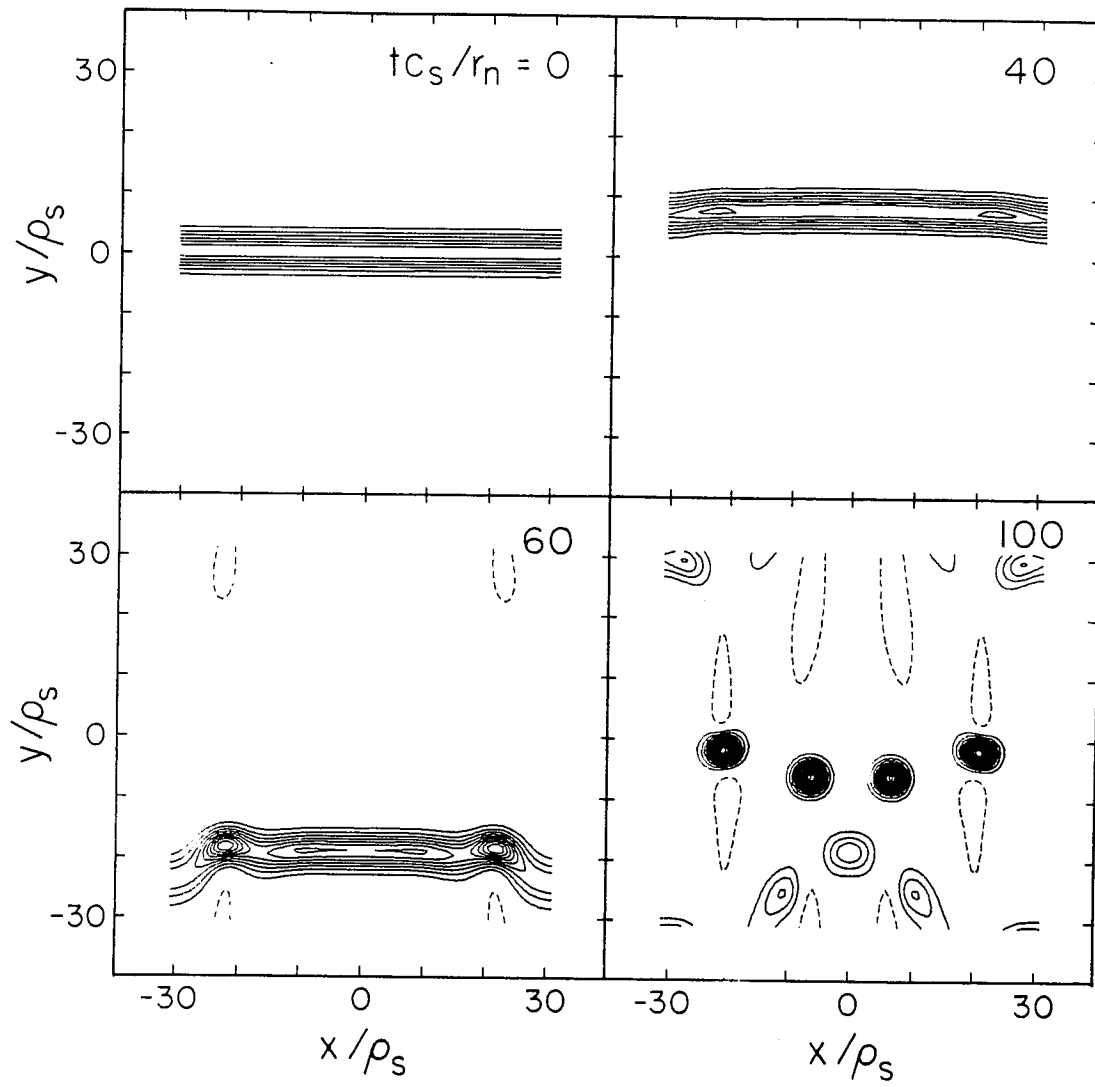


Figure 2.5: One-dimensional solitary wave traveling along the y -axis tears with finite k_x and forms two-dimensional solitary waves.

(a) shows the contours for the initial 1-D solitary wave solution with $k_x = 0$. (b)-(c) show the reconnection of the flow lines to form four strong, nearly circular vortices. Here $\alpha = 0.1$ and $u = 2v_d$ for the initial 1-D solitary wave, Eq. (2.18).

Now we ask if the cyclone will disappear eventually; in other words, if the cyclone can be the solution of Eq. (2.2).

From Sec. 2.3 the solitary wave solution of Eq. (2.7) does exist, which has the form,

$$\varphi = \left[\frac{3\gamma}{\alpha}(u - v_d) \right] \psi(kr) , \quad (2.20)$$

according to Eqs. (2.8) and (2.10), where $r = [x^2 + (y - ut)^2]^{1/2}$. So for $u > v_d$, we get a solitary solution for positive amplitude and the amplitude can be small by having $u \geq v_d$. For $uv_d < 0$ we get for negative amplitude and positive k^2 provided $\alpha|\varphi_m| > 3\gamma v_d$. Thus, the cyclone can only occur if there is sufficient energy in the initial structure.

This means that both the cyclones and anticyclones can exist and stay stable in the system after the initial dipole vortex pair breaks up if the amplitude φ_m of the dipole pair is large enough so that $\alpha|\varphi_m| > 3\gamma v_d$ where $\gamma = 1.5946$ has been determined in Sec. 2.3. This condition requires a substantial amplitude and energy for the solitary wave to form the cyclone. If one uses the approximate formula $\varphi_{dp} = 1.28v_d r_0$ for the amplitude of the dipole vortex, the condition for the onset of a cyclone can be re-expressed as the condition $r_0 > 3.74/\alpha$.

2.5 Summary and Conclusions

In this chapter, we have studied analytically and numerically the effect of KdV or scalar nonlinearity on the evolution of dipole vortex solutions of the nonlinear drift wave—Rossby wave equation. The study shows that the lifetime

of the dipole drift vortices depends on the magnitude of the scalar nonlinearity. For plasmas, the magnitude of the scalar nonlinearity is associated with a gradient of the plasma electron temperature [Petviashvili, 1977 and 1980], η_e , in the field of a drift wave and is described by the parameter $\alpha = \eta_e \rho_s / r_n$. In the Rossby waves the scalar nonlinearity arises from the variation of the depth of the fluid with wave amplitude, as in the classical KdV equation for shallow water waves. The lifetime scale of dipole of radius r_0 is estimated from $\tau \sim r_0 / \alpha \varphi_m$, where φ_m is a measure of vortex amplitude. We note that there is a critical amplitude for the formation of the cyclone. Above the critical amplitude we have shown that both the anticyclone ($\varphi > 0$) and cyclone ($\varphi < 0$) exist and do not disappear after the dipole vortex pair breaks up.

The question of the existence of the cyclone solution is important for the interpretation of the rotating water tank experiments. In the early experiments of Antipov *et al.* [1982 and 1983] only anticyclones were reported to be long-lived vortices. In the work of Antonova *et al.* [1983] with a larger tank it is reported that both cyclones and anticyclones are formed. We suggest that cyclones, although requiring sufficient amplitude to form, are a natural solution of the nonlinear drift wave-Rossby wave equation. The cyclones may be especially important for anomalous transport because of their low propagation velocity.

Chapter 3

Drift Wave Vortices in a Plasma with Temperature Gradient and Drift Velocity Shear

3.1 Introduction

In this chapter, we consider a generalization of the H-M drift wave equation that includes a general density profile $n_0(x)$ and temperature profile $T_e(x)$.

Petviashvili [1977] first studied the problem with a temperature gradient and an exponential density profile. The Petviashvili model became well known and stimulated numerous theoretical studies. However, the model he proposed has been criticized by several authors [Lakhin *et al.*, 1987 and 1988; Horiata and Sato, 1987; Laedke and Spatschek, 1988; Nycander, 1989] because of inconsistency with Ertel's theorem [Ertel, 1942], the basic conservation law of potential vorticity. Some of these authors [Lakhin *et al.*, 1987 and 1988; Horiata and Sato, 1987] showed that monopole vortices exist only when the drift velocity in Eq. (2.1) is nonconstant, $v_d = v_d(x)$. More recently, Spatschek *et al.* [1990] used a new high ordering with long wavelength scaling to develop a model that is essentially same as Petviashvili's model [Petviashvili, 1977]. These authors argue for the existence of a monopole vortex solution in the very long wavelength region ($\sim \rho_s/\epsilon$), even with constant drift velocity v_d . Here ϵ is the usual drift theory expansion parameter $\epsilon = \rho_s/r_n$, where $\rho_s = c(m_i T_e)^{1/2}/eB$ is drift wave dispersion scale length and r_n is the density

gradient scale length. We also define $\eta_e = r_n/r_{T_e}$ as the ratio of the density-to-temperature gradient scale length. The Spatschek *et al.* [1990] proposal to retain the Petviashvili model, while correct in terms of the special orderings involved, is of limited applicability since it requires $v_d(x)=\text{const.}$ over the large scales of ρ_s/ϵ . Thus it is of considerable practical interest to study the regime of general $v_d(x)$ and $T_e(x)$ addressed in this chapter.

It is well known that there exists a large class of vortex solutions for nonlinear drift waves. These solutions arise because of an arbitrary function $F(\varphi - ux)$ that appears in the equation for traveling wave solutions. Usually this function is chosen such that the solution vanishes as $r \rightarrow \infty$. The function F determines the relationship between the generalized potential vorticity, which to the first order is $\nabla^2\varphi - \varphi/T(x) - \ell n n_0(x)$, and the stream function, $\varphi - ux$, in a frame traveling with speed u . For the well known dipole vortex solution, the choice of this relationship is piece-wise linear with a jump in the slope $dF/d\varphi$. In spite of the presence of this jump the solution is consistent with the H-M equation [Meiss and Horton, 1983; Laedke and Spatschek, 1988]. Alternatively one can demand F to be analytic. In this chapter we show for a model that includes an arbitrary temperature gradient and a constant logarithmic density gradient, that the attempt to make the choice of F analytic makes it impossible to have a binding effective potential, thus showing that no local vortex solutions occurs for analytic F . Here the density profile is strictly exponential, but the result is independent of the temperature profile. However, with a more complex background plasma; i.e. with nonconstant drift wave velocity $v_d(x)$, the monopole vortex is found in the $\rho_s/\epsilon^{1/2}$ wavelength region with an analytic F . Physically the nonconstant $v_d(x)$ adds a shear to the diamagnetic drift

velocity. Since it is well known (Sagdeev *et al.* [1981] and Horton *et al.* [1987]) that shear flow causes the formation of monopole vortices, it is perhaps to be expected that the shear flow from nonuniform $v_d(x)$ will create monopole solitary waves.

Also we show that the monopole vortices mentioned above in inhomogeneous plasmas are not strictly localized soliton-like monopoles. The effect of inhomogeneity in the background plasma on vortex dynamics is shown to give rise to an oscillating tail; the inhomogeneity forces a coupling of the vortex core to the tail of a radiative wake of drift waves, which thus causes radiative damping of the vortex core.

This chapter is organized as follows: in Sec. 3.2, we derive the model equation for nonlinear drift waves in plasmas with density and temperature gradients. The steady state traveling wave equation of the model is given and solutions of this equation are discussed in Sec. 3.3. The subject of Sec. 3.4 is to study interaction of vortices with drift shear flow and mechanism of formation of monopole vortices. In Sec. 3.5 we investigate the effect of inhomogeneity on the drift wave vortex and give analytical results. Section 3.6 describes the results of the numerical investigations. Summary and conclusions are given in Sec. 3.7.

3.2 Model Equation of Drift Wave in Inhomogeneous Plasma

We consider a plasma in a uniform external magnetic field in the z -direction, where the electrons move freely along the magnetic field. The

dissipationless equation of motion and continuity equation for the ions are

$$\frac{d\mathbf{v}}{dt} = -\frac{e}{m_i} \nabla \Phi + \omega_{ci} \mathbf{v} \times \hat{\mathbf{z}} \quad (3.1)$$

$$\frac{\partial n}{\partial t} + \nabla \cdot (n\mathbf{v}) = 0, \quad (3.2)$$

where $d/dt = \partial/\partial t + \mathbf{v} \cdot \nabla$ and $\Omega = e\mathbf{B}/m_i c = \omega_{ci} \hat{\mathbf{z}}$ is the ion cyclotron frequency. The ion fluid Eq. (3.1) of motion can be rewritten in terms of the vorticity $\omega = \nabla \times \mathbf{v}$ by taking curl of Eq. (3.1):

$$\left(\frac{\partial}{\partial t} + \mathbf{v} \cdot \nabla \right) (\Omega + \omega) + (\Omega + \omega) \nabla \cdot \mathbf{v} = (\Omega + \omega) \cdot \nabla \mathbf{v} \quad (3.3)$$

Combining Eq. (3.3) with the continuity Eq. (3.2), one can derive Ertel's theorem [Ertel, 1942] by neglecting the parallel compression $\nabla_{\parallel} v_{\parallel}$,

$$\frac{d}{dt} \left(\frac{\omega_{ci} + \omega_z}{n} \right) = 0, \quad (3.4)$$

where

$$\omega_z = \hat{\mathbf{z}} \cdot (\nabla \times \mathbf{v}) = \frac{\partial v_y}{\partial x} - \frac{\partial v_x}{\partial y} = \frac{c}{B} \nabla^2 \Phi$$

with $\mathbf{v} = \mathbf{E} \times \mathbf{B}/B^2$. Equation (3.4) states that the potential vorticity

$$\Pi = \left[\frac{\Omega + \omega}{n} \right] \cdot \hat{\mathbf{z}}$$

is conserved by the flow. When $\nabla_{\parallel} v_{\parallel} \neq 0$, that is, there exists compressible parallel motion, the potential vorticity will be no longer conserved and solitary drift waves will experience the radiation damping due to the coupling of drift waves to ion acoustic waves. This subject will be studied in detail in the next chapter.

With the ordering,

$$\epsilon_t \equiv \frac{1}{\omega_{ci}} \frac{\partial}{\partial t} \sim \frac{\mathbf{v} \cdot \nabla}{\omega_{ci}} \ll 1,$$

to the lowest order in ϵ_i , we have

$$\mathbf{v} = \left(\frac{e}{m_i \omega_{ci}} \right) \hat{\mathbf{z}} \times \nabla \Phi,$$

$$\omega_z = \omega_{ci} \frac{\rho_s^2}{T_e} \nabla^2 (e\Phi),$$

and

$$\frac{d}{dt} = \frac{\partial}{\partial t} + \omega_{ci} \frac{\rho_s^2}{T_e} [e\Phi, \quad],$$

where $\rho_s = c_s/\omega_{ci}$ and $c_s = (T_e(x)/m_i)^{1/2}$. Now we define $T(x) = T_e(x)/T_0$ (where T_0 is a constant), $\varphi = (r_n/\rho_{s0})e\Phi/T_0$, and $\epsilon_n = \rho_{s0}/r_n$. Equation (3.4) becomes

$$\frac{\partial}{\partial t} \left(\frac{1 + \epsilon_n \nabla^2 \varphi}{n} \right) + \left[\varphi, \quad \frac{1 + \epsilon_n \nabla^2 \varphi}{n} \right] = 0. \quad (3.5)$$

where $[f, g] = \mathbf{z} \cdot \nabla f \times \nabla g$. The space and time variables are normalized by ρ_{s0} and r_n/c_{s0} , respectively, where $r_n^{-1} = -d\ln n_0/dx$, and ρ_{s0} and c_{s0} are the ion Larmor radius and ion acoustic speed at the reference electron temperature T_0 , respectively. Equation (3.5) states that the potential vorticity is conserved on each fluid element moving with the velocity $\mathbf{v} = \hat{\mathbf{z}} \times \nabla \varphi(x, y, t)$.

The local vorticity $\omega_z = \hat{\mathbf{z}} \cdot \nabla \times \mathbf{v}$ is a measure of the rotational part of the flow velocity $\mathbf{v}(\mathbf{x}, t)$, as opposed to the compressional $\nabla \cdot \mathbf{v}$ part of the flow. Being the rotation of \mathbf{v} , the vorticity is similar to a local spin of the fluid although it is not the same as the local angular momentum $\mathbf{r} \times \mathbf{v}$. In a patch of plasma with solid body rotation at the angular frequency Ω the local velocity is $\mathbf{v} = \mathbf{r} \times \boldsymbol{\Omega} = r\Omega\hat{\boldsymbol{\theta}}$ and $\omega_z = 2\Omega$. In such a patch of plasma of radius R the potential disturbance is parabolic with $\Phi = (R^2\Omega B/2c)(r^2/R^2 - 1)$ so that $v_\theta = (c/B)(\partial\Phi/\partial r) = r\Omega$ and $\omega_z = 2\Omega$. Here $\Omega < 0$ is a cyclonic and $\Omega > 0$ is an anticyclonic disturbance.

To close Eq. (3.5), we assume that the particles satisfy the condition of quasi-neutrality with the electrons obeying the Boltzmann density distribution. Thus, the ion density is given by

$$n = n_0(x) \exp\left[\frac{e\Phi}{T_e(x)}\right] = n_0(x) \exp\left[\frac{\epsilon_n \varphi}{T(x)}\right], \quad (3.6)$$

where $n_0(x)$ and $T(x)$ are assumed to be analytic functions. Due to the fact that ϵ_n is a small parameter, for the numerical calculations in Sec. 3.6 the exponential in Eq. (3.6) is expanded to first order in ϵ_n . For certain strong monopole solutions with large negative φ , however, the expansion can lead to negative density states. Thus, whenever the expansion is performed we require that $\epsilon_n \varphi < T$ for all x .

3.3 Traveling Wave Equation and Solutions

Now we look for stationary traveling wave solutions of Eq. (3.5) of the form $\varphi = \varphi(x, y - ut)$. Such solutions travel with the velocity u in the y -direction. Equations (3.5) and (3.6) together give the following:

$$-u \frac{\partial G}{\partial y} + [\varphi, G] = 0, \quad (3.7)$$

where

$$G = \frac{1 + \epsilon_n \nabla^2 \varphi}{n_0(x) \exp(\epsilon_n \varphi / T(x))}.$$

Equation (3.7) gives the condition for stationarity as

$$[\varphi - ux, G] = 0, \quad (3.8)$$

which requires that

$$\frac{1 + \epsilon_n \nabla^2 \varphi}{n_0(x) \exp(\epsilon_n \varphi / T(x))} = F(\varphi - ux) \quad (3.9)$$

where F is an arbitrary function of its argument.

If we choose F to be an analytic function determined by the density profile $n_0(x)$, that is,

$$F(\varphi - ux) = \frac{1}{n_0[(ux - \varphi)/u]} , \quad (3.10)$$

then Eq. (3.9) becomes

$$\epsilon_n \nabla^2 \varphi = \frac{n_0(x)}{n_0(x - \frac{\varphi}{u})} \exp\left(\frac{\epsilon_n \varphi}{T(x)}\right) - 1 , \quad (3.11)$$

With this choice of F the right hand side of Eq. (3.11) approaches zero as $|x| \rightarrow \infty$ and $\varphi \rightarrow 0$, which corresponds to the untrapped flow region. It is possible that there exist other analytic choices for F that satisfy $\nabla^2 \varphi \rightarrow 0$ as $|x| \rightarrow \infty$ and $\varphi \rightarrow 0$, which may lead to localized solutions for reasonable density profiles $n_0(x)$. But for the strictly exponential profile $n_0(x) = \exp(-\epsilon_n x)$ and the F of Eq. (3.10), bound solutions do not exist. To see this, we insert the density profile $n_0(x)$ into Eq. (3.11) and write the equation into the following nonlinear Poisson equation for φ :

$$\begin{aligned} \epsilon_n \nabla^2 \varphi &= \exp \left[\epsilon_n \left(\frac{1}{T(x)} - \frac{1}{u} \right) \varphi \right] - 1 \\ &= -\frac{\partial}{\partial \varphi} \left[\varphi - \frac{\exp [\epsilon_n (1/T(x) - 1/u) \varphi]}{\epsilon_n (1/T(x) - 1/u)} \right] . \end{aligned} \quad (3.12)$$

The effective potential for Eq. (3.12) is then

$$V_{\text{eff}}(\varphi, x) = \varphi - \frac{\exp [\epsilon_n (1/T(x) - 1/u) \varphi]}{\epsilon_n (1/T(x) - 1/u)} . \quad (3.13)$$

It is easy to prove that this effective ("time" dependent) potential $V_{\text{eff}}(\varphi, x)$ [Eq. (3.13)] for any temperature profile $T(x)$, is simply not able to

form a soliton well, and thus bind a local disturbance to form a solitary vortex (monopole or dipole). Therefore, the choice of F specified in Eq. (3.10) does not produce any solitary wave solutions with any kind of temperature profile $T(x)$.

However, the fact that this choice for F does not produce a localized solution does not exclude the possibility that the dynamics of the plasmas in relaxing from a turbulent state finds another choice of $F(\varphi - ux)$ with a new structure that allows binding. One example for a binding F structure is to follow the modon construction [Makino *et al.*, 1981; Meiss and Horton, 1983] for the dipole vortex by choosing $F(\varphi - ux)$ to be piecewise linear. For the dipole vortex, F is the same as Eq. (3.10) in the untrapped region $r > r_0$ and a different interior function $F_{\text{int}}(\varphi - ux)$ with opposite signed slope $dF/d\varphi$ in the trapped region $r < r_0$. To see the relationship with the dipole vortex solution we consider the logarithm of Eq. (3.9)

$$\ell n(1 + \epsilon_n \nabla^2 \varphi) = \ell n F(\varphi - ux) + \ell n n_0 + \frac{\epsilon_n \varphi}{T(x)}. \quad (3.14)$$

With $n_0(x) = \exp(-\epsilon_n x)$, in the exterior or untrapped region

$$F_{\text{ext}}(\varphi - ux) = \exp[\epsilon_n(x - \varphi/u)]$$

as defined by Eq. (3.10), and the ordering

$$u \sim v_{d0} \equiv v_d(x=0) = 1, \quad \frac{e\Phi}{T_e} \sim \frac{\rho_{s0}}{r_{n0}} \equiv \epsilon_n \sim \epsilon \ll 1, \quad (3.15)$$

Eq. (3.14) to lowest order in ϵ yields

$$\nabla^2 \varphi = \left(\frac{1}{T(x)} - \frac{v_{d0}}{u} \right) \varphi \quad \text{for} \quad r \geq r_0. \quad (3.16)$$

For the interior ($r < r_0$) solution we choose

$$\ell n F_{\text{int}}(\varphi - ux) = -\epsilon_n(1 + p^2)(\varphi - ux) , \quad (3.17)$$

so that, to the lowest order in ϵ , Eq. (3.14) reduces to

$$\nabla^2 \varphi + \left(1 + p^2 - \frac{1}{T(x)}\right) \varphi = [u(1 + p^2) - 1] x \quad \text{for} \quad r < r_0 . \quad (3.18)$$

Equation (3.18) for the interior vortex structure is driven by a source term which measures the mismatch between the vortex speed u and the linear wave speed $1/(1+p^2)$. The constant $p^2 > 0$ is determined by continuity of φ , $\partial\varphi/\partial r$, and $\nabla^2\varphi$ at $r = r_0$. In the case where $T = \text{constant}$ this choice for $F(\varphi - ux)$ produces dipole solutions [Meiss and Horton, 1983] of radius r_0 with an amplitude that increases as $v_{d0}r_0$. Thus, while we have shown that the simplest analytic choice of $F(\varphi - ux)$ forbids the existence of monopole vortices for the strictly exponential density profile, the plasma dynamics in relaxing from a turbulent state in which trapping takes place may naturally produce a $F(\varphi - ux)$ with nonanalyticity at the point of transition between the trapped and untrapped regions. An example from turbulent particle simulation that demonstrates an abrupt change in the slope of $F(\varphi - ux)$ as plotted versus vorticity is shown in Horton *et al.* [1987]. However, the dipole vortices have been shown [Su *et al.*, 1988; Spatschek *et al.*, 1990] to be structurally unstable, in particular, a small term of KdV type nonlinearity can split them into monopole-like vortices, an effect to which we now turn.

In most magnetic confinement systems both $T_e(x)$ and $v_d(x)$ vary on the scale of r_n . We define the dimensionless parameters $\kappa_T \equiv \rho_{s0}d(1/T)/dx \sim \epsilon$ and $v'_{d0} \equiv \rho_{s0}dv_d/dx \sim \epsilon_n v_{d0}$. In the case of a nonconstant drift velocity $v_d(x)$, with or without a temperature gradient, the analytic choice of $F(\varphi - ux)$ in

Eq. (3.10) can lead to the possibility of trapping and the formation of solitary vortices. Taking the logarithm of Eq. (3.11)

$$\ln(1 + \epsilon_n \nabla^2 \varphi) = \ln n_0(x) - \ln n_0(x - \frac{\varphi}{u}) + \frac{\epsilon_n \varphi}{T(x)}. \quad (3.19)$$

and expanding the density profile as

$$\ln n_0(x) = -\epsilon_n(v_{d0}x + \frac{v'_{d0}}{2}x^2 + \dots) \quad (3.20)$$

yields

$$\ln(1 + \epsilon_n \nabla^2 \varphi) = \epsilon_n k^2(u, x) \varphi + \epsilon_n \frac{v'_{d0}}{2u^2} \varphi^2 + \dots \quad (3.21)$$

where

$$k^2(u, x) \equiv \frac{1}{T(x)} - \frac{v_d(x)}{u} \quad (3.22)$$

and

$$v_d(x) = 1 + v'_{d0}x. \quad (3.23)$$

Observe that $v_{d0} = 1$ follows from the choice of space-time units.

With the ordering

$$\rho_{s0}^2 \nabla^2 \sim \frac{e\Phi}{T_e} \sim \kappa_T \sim v'_{d0} \sim \frac{\rho_{s0}}{r_{n0}} \equiv \epsilon_n \sim \epsilon \ll 1, \quad \text{and} \quad u \sim v_{d0} = 1 \quad (3.24)$$

and keeping only the terms of order ϵ^2 in Eq. (3.21), we get

$$\nabla^2 \tilde{\varphi} = k_0^2 \varphi + \frac{v'_{d0}}{2u^2} \varphi^2, \quad (3.25)$$

where we have expanded

$$k^2(u, x) = k_0^2 + \alpha x + \dots$$

and considered

$$k_0^2 = (1 - v_{d0}/u) \sim \epsilon \quad \text{and} \quad \alpha = (\kappa_T - v'_{d0}/u) \sim \epsilon^2.$$

Notice that Eq. (3.25) has the same form as the Petviashvili equation for the steady state [Petviashvili, 1977]. But the crucial difference is that in the Petviashvili equation the nonlinear term arises due to the temperature gradient, while in the present case the nonlinear term is caused by the gradient of drift velocity. However, the gradient of the drift velocity also gives rise to a linear damping term $-(v'_{d0}/u)x\varphi$ on the right side of Eq. (3.25), which is of the same order as the other terms. The important thing is that although the temperature gradient does not contribute to the nonlinear term, its existence can balance the linear damping term caused by the gradient of drift velocity v'_{d0} . In this way the linear damping term is made smaller and exact monopole vortex solutions are possible when $\kappa_T = v'_{d0}/u$ or $\alpha = 0$.

The quadratic nonlinear Poisson Eq. (3.25) has monopole vortex solutions [Horiata and Sato, 1987; Su *et al.*, 1988] when $k_0^2 \equiv (1/T - v_d/u)_0 > 0$. The solutions can be approximately [Horiata and Sato, 1987; Petviashvili, 1980] written as follows, for small r ,

$$\varphi(x, y, t) = -2.4k_0^2 \left(\frac{2u^2}{v'_{d0}} \right) \left[\cosh \left(\frac{3}{4}k_0 \sqrt{x^2 + (y - ut)^2} \right) \right]^{-\frac{4}{3}}. \quad (3.26)$$

Figure 3.1 is 3-D plot and contour plot of the solution for $v'_{d0} = 0.05$ and $u = 1.5$.

From Eqs. (3.25) and (3.26) we see that the sign of the vortex amplitude no longer depends on the sign of velocity u as is the case for Petviashvili monopoles [Petviashvili, 1980]. Instead it depends on the sign of v'_{d0} . From

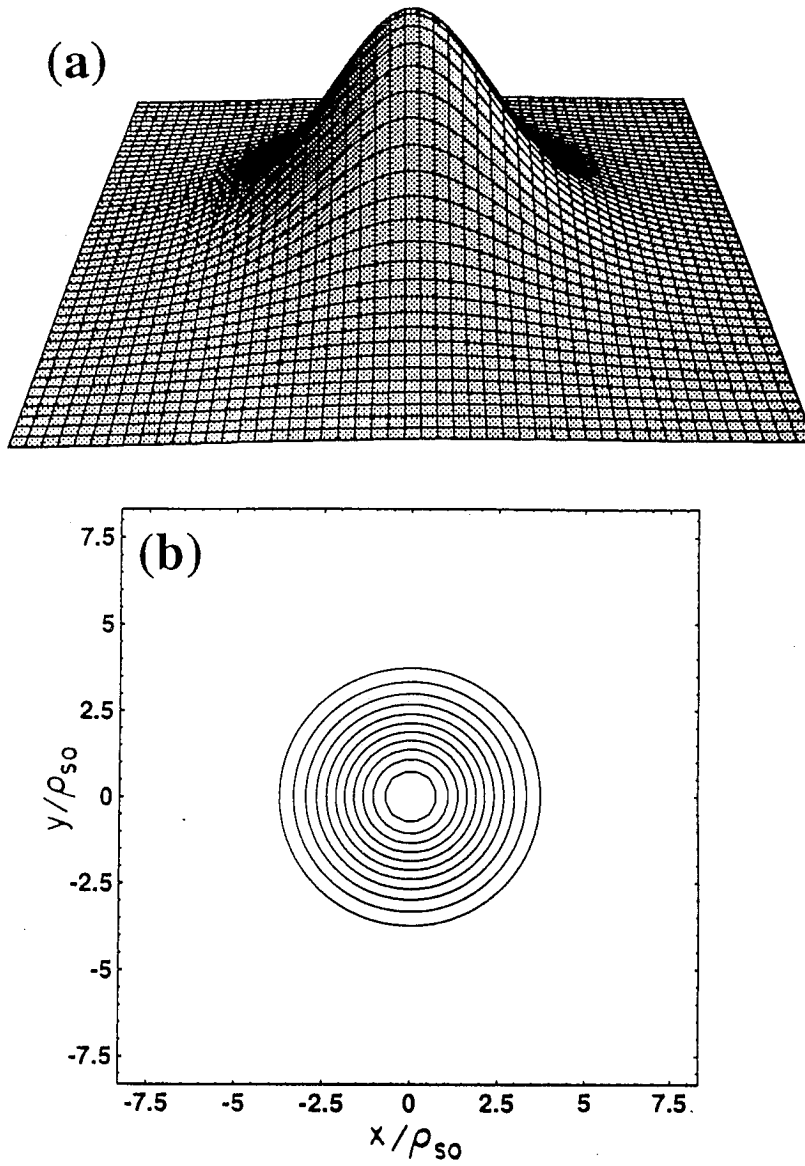


Figure 3.1: Stationary monopole solution given in Eq. (3.26) for $v'_{d0} = 0.05$ and $u = 1.5$.

(a) 3-D plot of the monopole. (b) Contour plot of the monopole.

Eq. (3.25), we recognize the symmetry relation

$$\varphi(-v'_{d0}; x, y) = -\varphi(v'_{d0}; x, y),$$

which we test in the simulations. The simulation results will be discussed in Sec. 3.6.

We have also tested the new monopole vortex solution given here for soliton-like behavior upon collision. Initially we put a strong vortex behind a weaker vortex with the both vortices moving in the same direction. The numerical results show that the stronger vortex overtakes and passes through the weaker vortex. After the collision, both the vortices nearly restore their shapes, that is, the overtaking collision observed is largely elastic. The result is showed in Fig. 3.2. We also did numerical experiments on point vortex-like interaction of the monopole vortices. We used two nearly equal strength monopole vortices with the same signs in a range of $15\rho_s$. The results in Fig. 3.3 show that the two strong monopole vortices interact like point-vortices rotating around one another.

The following amplitude-velocity relation is obtained from Eq. (3.26):

$$u = \frac{v_{d0} \pm \sqrt{v_{d0}^2 + 0.83|v'_{d0}\varphi_m|}}{2} \quad (3.27)$$

where φ_m is the amplitude of the monopole vortex given by Eq. (3.26). However, the monopole vortex solutions given here must propagate in the direction of the drift wave ($uv_{d0} > 0$) since the negative velocity ($uv_{d0} < 0$) monopoles have $k_0^2 = 1 + v_{d0}/|u| \geq 1$, which violates the ordering in Eq. (3.24) required for localization. In this short wavelength region, $r_0 \sim \rho_{s0}$, there are no localized monopole solutions as discussed in the beginning of this section. Therefore we

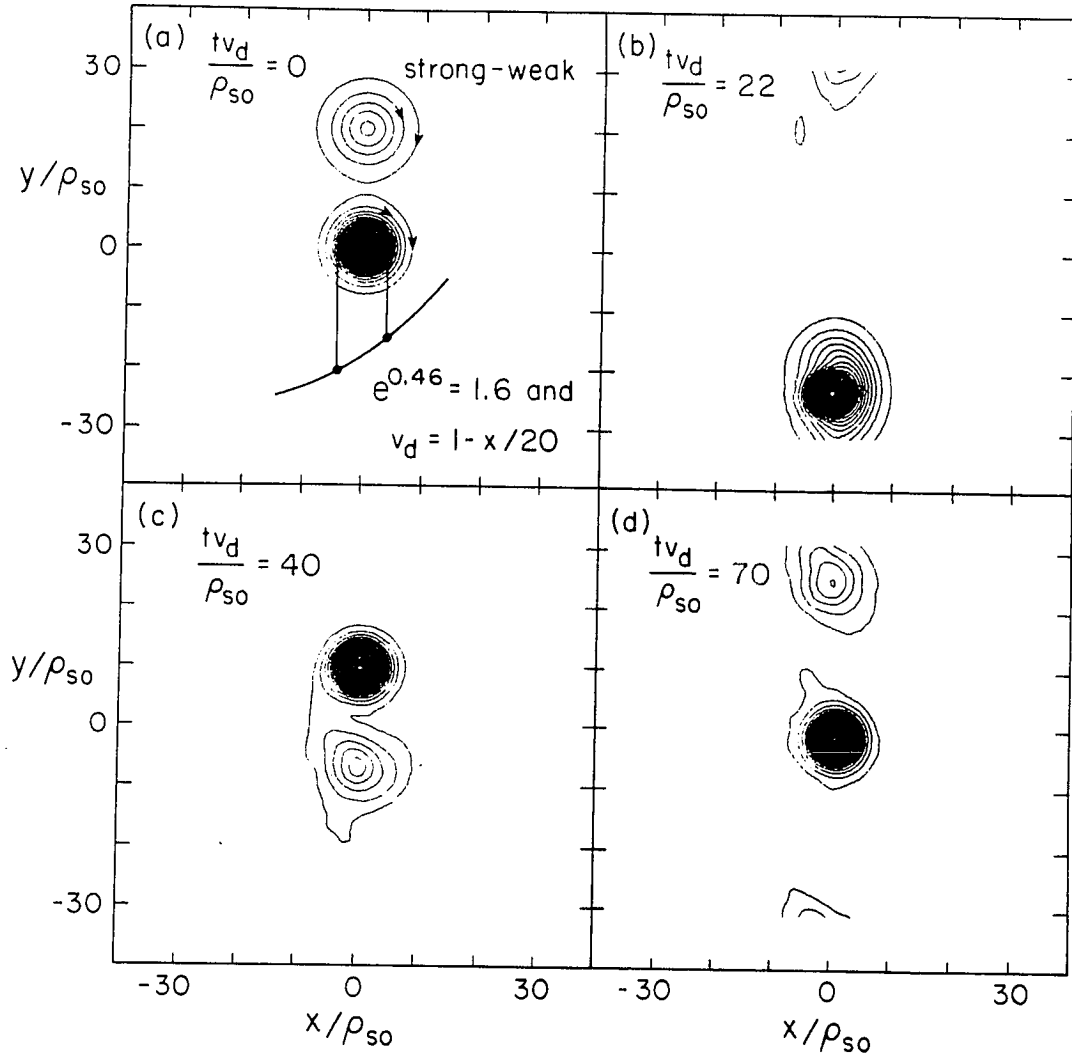


Figure 3.2: Nearly elastic overtaking collision of a strong monopole vortex with a weaker monopole vortex.

The profile of $1/T(x) = \exp(0.046x)$ gives a variation of 1.6 over the core of the vortex. The gradient in the drift velocity is $v_d(x) = 1 - x/20$. The speeds of the two vortices are $u_1 = 1.1$ and $u_2 = 1.7$ giving the expected collision time $\Delta l/\Delta u = 20/0.6 = 33$ compared with observed overlapping at $t = 22$ in frame(b). After separation showed in (c) and (d) frames, the weaker vortex still has 5 closed contours.

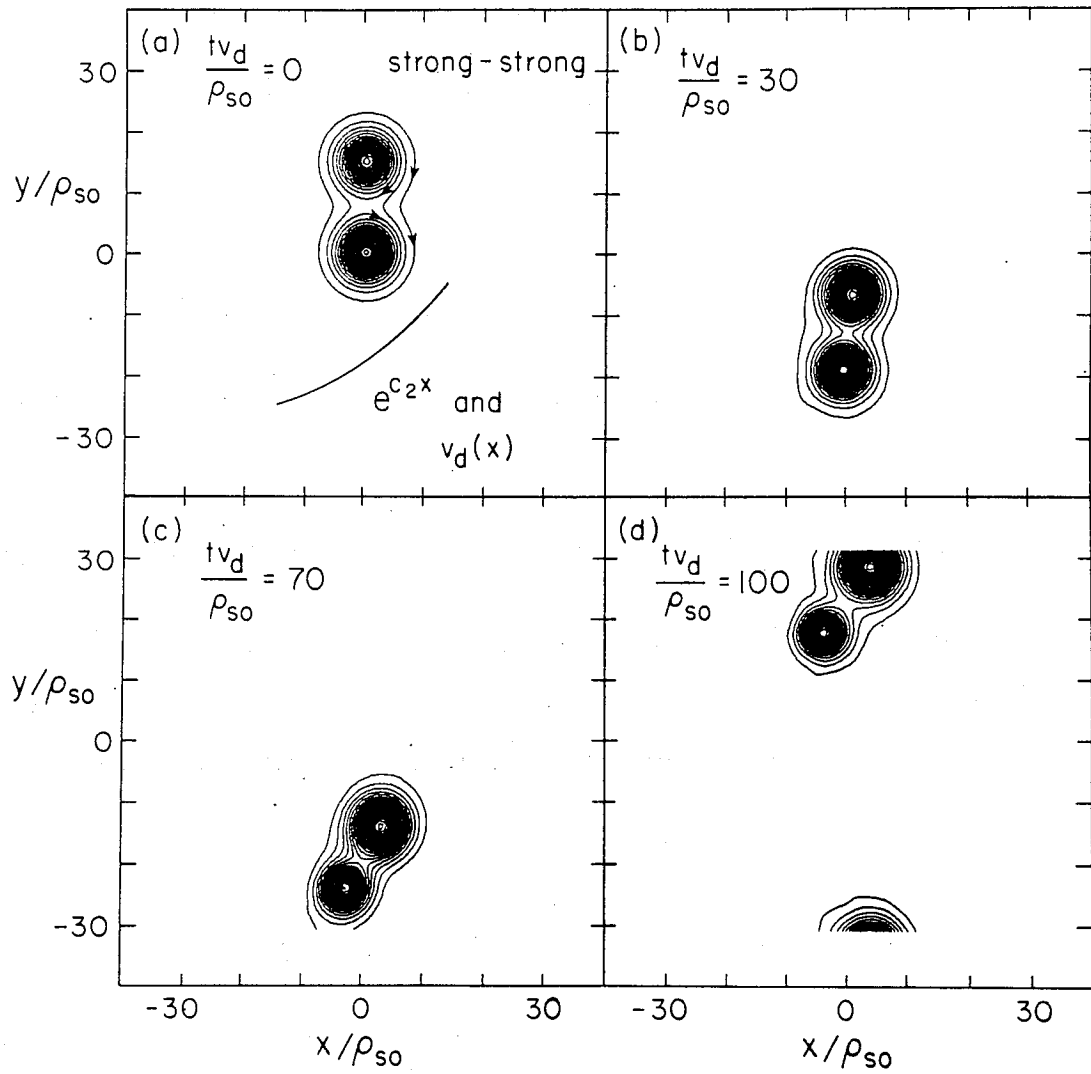


Figure 3.3: Point vortex type of interaction of two strong monopole vortices.

$u_1 = 1.3$, and $u_2 = 1.35$. Although merging might be expected here, instead the vortices rotate around one another after pulling together from the initial separation of $15\rho_s$.

can only take the positive sign in Eq. (3.27) and the monopole vortex speed is

$$u(\varphi_m) = \frac{v_{d0} + \sqrt{v_{d0}^2 + 0.83|v'_{d0}\varphi_m|}}{2}, \quad (3.28)$$

which clearly reduces to the usual drift wave when

$$|v'_{d0}\varphi_m| \ll v_{d0}^2 \quad \text{or} \quad \frac{e\Phi_m}{T_e} \ll \frac{(dn_0/dx)^2}{d^2n_0/dx^2}. \quad (3.29)$$

We can use the amplitude φ_m to estimate the maximum or minimum density of the vortex

$$n/n_0 = \exp\left(\frac{\epsilon_n \varphi}{T(x)}\right) \approx \exp(\epsilon_n \varphi_m) = \exp\left(-\frac{4.8\epsilon_n}{v'_{d0}} u(u - v_{d0})\right). \quad (3.30)$$

Deriving Eq. (3.25), and therefore Eq. (3.26) from Eq. (3.21) implies that we have expanded the Boltzmann density distribution of Eq. (3.6) to first order in ϵ_n and dropped all the higher order terms. For consistency of the expansion,

$$\epsilon_n |\varphi_m| = \frac{4.8\epsilon_n}{|v'_{d0}|} u(u - v_{d0}) \leq 1$$

We therefore get the interval condition for the velocity u

$$v_{d0} \leq u \leq \frac{v_{d0} + \sqrt{v_{d0}^2 + 0.83|v'_{d0}|/\epsilon_n}}{2} \quad (3.31)$$

required for the validity of the expansion. Equation (3.31) shows that u must be the same order as v_{d0} . This implies that we consider $v'_{d0} \sim \epsilon_n$.

Spatschek *et al.* [1990] ordering:

Using a multiple-scale method and a different ordering, namely taking

$$\rho_s^2 \nabla^2 \sim \frac{e\Phi}{T_e} \sim \frac{u}{c_s} \sim \kappa_T \sim k_0^2 \sim \epsilon^2, \quad \text{and} \quad \frac{1}{\omega_{ci}} \frac{\partial}{\partial t} \sim \epsilon^5, \quad (3.32)$$

Spatschek *et al.* [1990] developed a model in which the steady state equation has a form similar to Eq. (3.25), but with a coefficient of the last nonlinear term in Eq. (3.25) proportional to $\kappa_T \equiv -(1/T)(\partial \ln T / \partial x)$.

Although both the equations (our Eq. (3.25) and Eq. (5) in Spatschek *et al.* [1990]) have been shown to have monopole solutions [Petviashvili, 1977 and 1980; Su *et al.*, 1988; Spatschek *et al.*, 1990], in reality the vortex wave function will extend into the region where

$$k^2(u, x) = k_0^2 + \alpha x + \dots < 0. \quad (3.33)$$

When this happens outgoing drift wave propagation occurs. The matching analysis in Sec. 3.5 shows that the amplitude of the outgoing wave is of order $\varphi_{\text{vortex}}(x = x_{\text{crit}})$ where x_{crit} is the point at which

$$k^2(u, x_{\text{crit}}) = 1/T - v_d/u = 0.$$

For large scale vortices with core size $r_0 \sim k_0^{-1} > \rho_{s0}/\epsilon^{2/3}$, in inhomogeneous plasma, the coupling to outgoing drift waves is a strong effect that eliminates the existence of the monopole vortex.

3.4 Interaction of Vortices with Drift Sheared Flow and the Formation of Monopole Vortices

In the last section, we have derived the solitary vortex solutions in inhomogeneous plasmas and found that such solutions behave like monopole vortices and that the sign of vorticity of the monopole vortex depends on the sign of drift velocity gradient v'_{d0} . Physically the finite drift velocity gradient v'_{d0} adds a shear to the diamagnetic drift velocity and the interaction of the

sheared flow with vortices gradually destroys one pole of dipole vortex structures which are characterized by two poles with opposite signs of vorticity. Therefore monopole vortex structure becomes dominant form of vortex in such an environment [Sagdeev *et al.*, 1981; Horton *et al.*, 1987; Horton, 1989]. Figure 3.4 is the simulation results for the interaction of the dipole vortex with a sheared flow. As seen in Fig. 3.4 the dipole first separates into two monopoles, a cyclone $\varphi < 0$ and an anticyclone $\varphi > 0$, as reported in Chapter 2. Finally, only one monopole survives, which is determined by the sign of v'_{d0} . If $v'_{d0} > 0$, only the cyclone survives, while if $v'_{d0} < 0$, only the anticyclone survives.

The mechanism of the interaction of dipole vortex with sheared flow and the formation of monopole vortex can be understood from Figs. 3.5 and 3.6. Figure 3.5 shows the configuration of the sheared flow superimposed upon the dipole vortex shown in Fig. 3.4(a). The sheared flow places a stagnation point (x point) in the flow at a distance $\Delta x = u/v'_{d0}$ on the side of the dipole vortex with opposing flows, where u is velocity of the dipole vortex. When the stagnation point is within the distance $u/v'_{d0} < 2r_0$ from the vortex center, where r_0 is the dipole vortex radius, the peeling and/or reinforcing processes of the vortex demonstrated in Fig. 3.6 will be taking place. From Fig. 3.6(a) one can see that the flows at the left and right sides of the positive pole of the dipole vortex oppose to that of the sheared flow. The sheared flow of background causes the outer layer of fluid in the positive pole to peel off as shown in Fig. 3.6(b). The "peeled-off" section of the positive pole can reinforce the sheared flow of background [Drake *et al.*, 1992]. The positive pole or lobe of the dipole vortex continues to peel until it is entirely destroyed. On the other hand, the negative pole of the dipole vortex, which has the velocity opposite

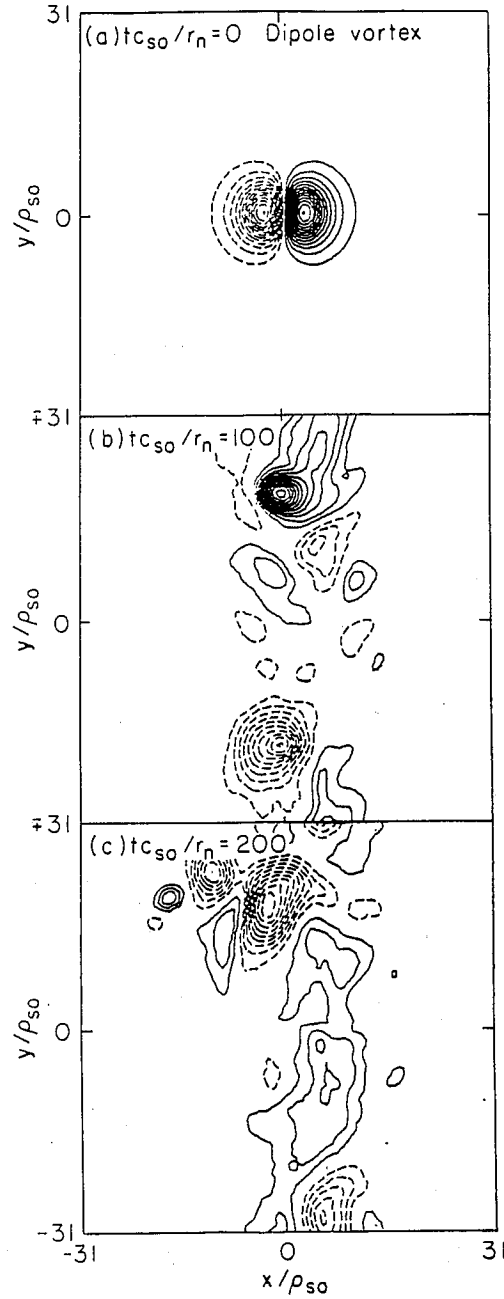


Figure 3.4: Interaction of dipole vortex with drift shear flow.

(a) Contour plot of the electrostatic potential $\varphi(x, y, t)$ of Eq. (3.47). The dipole vortex (solution of the H-M equation) is taken as initial condition with $T(x) = \exp(-c_2 x)$, $c_2 = 0.046$, $u = 1.1$, $r_0 = 6.0$, and $v'_{d0} = 0.05$. The solid lines represent positive values of potential φ , and the dashed lines are negative values. (b) The dipole vortex is first split into two monopoles, cyclone ($\varphi < 0$) and anticyclone ($\varphi > 0$). (c) Only the cyclone is seen to survive.

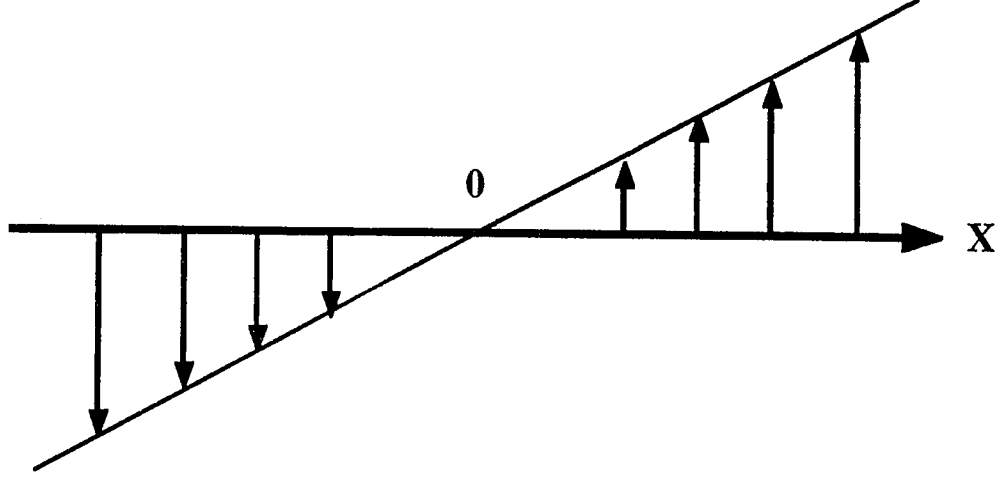


Figure 3.5: Configuration of sheared flow.

to that of the positive pole, has the flows at the left and right sides reinforced by the sheared flow as seen in Fig. 3.6(c). Therefore, the remaining **negative** pole eventually evolves into a shear flow driven monopole vortex as shown in Fig. 3.6(d) with the form given in Eq. (3.26).

3.5 Radiation Damping of Solitary Drift Wave Vortex in Inhomogeneous Plasmas

In the small amplitude region exterior to the vortex core the wave field is given, from Eq. (3.21), by

$$\frac{\partial^2 \varphi_{k_y}(x)}{\partial x^2} + \left[-\left(\frac{1}{T(x)} - \frac{v_d(x)}{u} \right) - k_y^2 \right] \varphi_{k_y}(x) = 0, \quad (3.34)$$

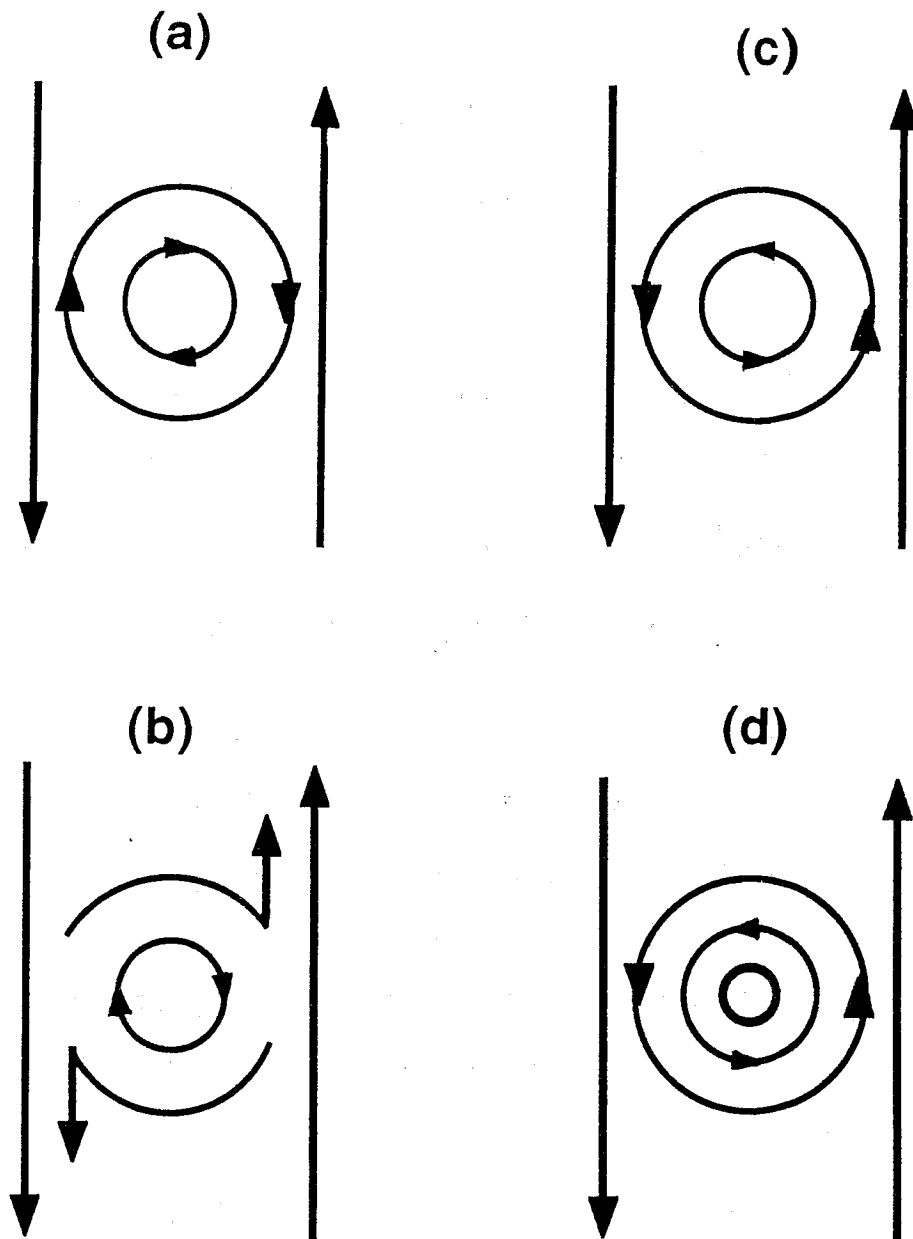


Figure 3.6: Interaction of vortex with sheared flow

(a) The positive pole in sheared flow. (b) The sheared flow of background causes the outer layer of fluid in the positive pole to peel off. (c) The negative pole in sheared flow. (d) The flow of the negative pole is reinforced by the sheared flow and eventually evolves into a shear flow driven monopole vortex.

with $\varphi_{k_y}(x)$ the Fourier transform in y of $\varphi(x, y, t)$ such that

$$\varphi(x, y, t) = \int dk_y \varphi_{k_y}(x) e^{ik_y(y-ut)}.$$

Equation (3.34) has turning points at $x = x_T$ where the x_T are determined by $v_d(x_T)/u - k_y^2 - 1/T(x_T) = 0$. For $k_y^2 \rightarrow 0$ the $x_T(k_y) \rightarrow x_{\text{crit}}$ defined by $k^2(u, x_{\text{crit}}) = 0$ in Eq. (3.33).

For $|x| > x_0$ in the exterior region, where x_0 is the length scale of the vortex core given by $k_0 x_0 \simeq 1$, the WKB solutions of Eq. (3.34) are

$$\varphi_{k_y}(x) = \begin{cases} A_{k_y} Q_{k_y}^{-1/4}(x, u) \exp\left(i \int_{x_T}^x Q_{k_y}^{1/2}(x', u) dx'\right), & Q_{k_y}(x, u) > 0 \\ A_{k_y} (-Q_{k_y}(x, u))^{-1/4} \exp\left(-\int_{x_T}^x (-Q_{k_y}(x', u))^{1/2} dx' - \frac{i\pi}{4}\right), & Q_{k_y}(x, u) < 0 \end{cases} \quad (3.35)$$

where

$$Q_{k_y}(x, u) = v_d(x)/u - 1/T(x) - k_y^2$$

and the amplitude A_{k_y} will be determined by matching to the vortex solution. Equation (3.35) with $Q_{k_y} > 0$ describes the outgoing radiation wave in the high density gradient and high temperature region. In the region where $v_d(x)/u - 1/T(x) < k_y^2$, we again expand $v_d(x)/u - 1/T(x) \simeq -k_0^2 - \alpha x > 0$. Then $x_T \simeq -(k_0^2 + k_y^2)/\alpha$ for $k_0^2 > 0$ and

$$\int_{x_T}^x (-Q_{k_y}(x, u))^{1/2} dx' \simeq [x - (2/3|\alpha|)(k_0^2 + k_y^2)](k_0^2 + k_y^2)^{1/2}$$

for $|x_0| \ll |x| \ll |x_T|$.

The approximate exterior vortex solution can be obtained by neglecting the nonlinear term in Eq. (3.25),

$$\varphi(x, y, t) \simeq \varphi_m K_0(k_0 r) \quad (3.36)$$

where

$$r = [x^2 + (y - ut)^2]^{1/2}, \quad \text{and} \quad \varphi_m = -4.8k_0^2 u^2 / v'_{d0}$$

is the amplitude of the vortex. The Fourier transform of Eq. (3.36) in y is [Magnus and Oberhettinger, 1949]

$$\varphi_{k_y}(x) = \frac{\varphi_m}{2} \frac{\exp(-|x|\sqrt{k_0^2 + k_y^2})}{\sqrt{k_0^2 + k_y^2}}. \quad (3.37)$$

Matching Eq. (3.37) and Eq. (3.35) with $Q_{k_y} < 0$, we can obtain the radiation amplitude formula

$$A_{k_y} \simeq \frac{\varphi_m}{2(k_0^2 + k_y^2)^{1/4}} \exp \left[i \frac{\pi}{4} - \frac{2}{3|\alpha|} (k_0^2 + k_y^2)^{3/2} \right], \quad (3.38)$$

which is to be used in Eq. (3.35). Therefore the monopole vortex solution of Eq. (3.25) is coupled to a radiation wave with significant amplitude unless the condition $|\alpha| \ll 2k_0^3/3 \sim \epsilon^{3/2}$ is satisfied.

We point out that for the case discussed in Spatschek *et al.* [1990], where the stationary equation is similar to that of Eq. (3.25) but with the longer wavelength scaling $k_0 \sim \epsilon$ and $\alpha \sim \epsilon^3$, the monopole vortices should have oscillating tails with the substantial amplitude $\sim ((2/\epsilon)^{1/2} \varphi_m / 4) \exp(-2/3)$ as seen from Eq. (3.38). The numerical solutions given in their work do not show the oscillating tail since their equation (Eq. (8) in Spatschek *et al.* [1990]) does not explicitly contain the inhomogeneity. Their numerical results, therefore, are only for the very special case of $\kappa_T = v'_{d0}/u$, i.e., $\alpha = 0$. Therefore the solutions which the authors give are essentially those given in the previous chapter for the Petviashvili equation.

The decay rate of energy of the solitary drift wave can be computed

by using the energy conservation law,

$$\frac{\partial \mathcal{E}}{\partial t} + \nabla \cdot \mathbf{S} = 0, \quad (3.39)$$

where

$$\mathcal{E}(x, y, t) = \frac{1}{2} \left[\frac{\varphi^2}{T(x)} + (\nabla \varphi)^2 \right], \quad (3.40)$$

and

$$\mathbf{S} = \left(\frac{v_d(x)}{2} \varphi^2 - \frac{\kappa_T}{3} \varphi^3 \right) \hat{y} - \varphi \nabla \frac{\partial \varphi}{\partial t} - \nabla^2 \varphi \left(\hat{z} \times \nabla \frac{\varphi^2}{2} \right) \quad (3.41)$$

are the local energy density and the energy flux, respectively. Integrating Eq. (3.41) over the space volume, with the help of Eqs. (3.25), (3.26) and (3.36), we obtain the energy for the monopole vortex

$$E_v = \int \mathcal{E} d^3x \approx \frac{8.2\pi L_c u^4 k_0^2}{(v'_{d0})^2} \left(\frac{4}{3} + k_0^2 \right), \quad (3.42)$$

where L_c is the length scale in z of the coherent vortex structure.

The outgoing wave propagation given by the matching of Eq. (3.37) to Eq. (3.35), leads to the decay of the vortex energy E_v . Integrating the energy balance Eq. (3.39) over the space volume $\int d^3x$, neglecting the last term of Eq. (3.41) proportional to φ^3 , since φ is exponentially small for $x \gg x_0$, and using Parseval's theorem and Eq. (3.35) to evaluate the outgoing wave energy flux, gives the decay rate of vortex energy

$$\begin{aligned} \frac{dE_v}{dt} &= \int d^3x \frac{\partial \mathcal{E}}{\partial t} \simeq \int dy dz \left[\varphi \frac{\partial^2 \varphi}{\partial x \partial t} \right]_{x=-L}^{x=L} \\ &= -\frac{uL_c}{4\pi} \int_{-\infty}^{+\infty} dk_y i k_y \left[\varphi_{k_y}^*(x) \partial_x \varphi_{k_y}(x) - \varphi_{k_y}(x) \partial_x \varphi_{k_y}^*(x) \right]_{x=-L}^{x=L} \\ &= -\frac{uL_c}{\pi} \int_0^\infty dk_y k_y |A_{k_y}|^2, \end{aligned} \quad (3.43)$$

which is independent of L_x for $L_x \gg x_0$.

Using Eq. (3.38) for A_{k_y} we perform the k_y integral to obtain the vortex decay rate

$$\begin{aligned} \frac{dE_v}{dt} &= -\frac{uL_c\varphi_m^2}{4\pi} \int_0^\infty dk_y \frac{k_y}{\sqrt{k_0^2 + k_y^2}} \exp\left(-\frac{4}{3|\alpha|}(k_0^2 + k_y^2)^{3/2}\right) \\ &= -\frac{B}{3b^{1/3}} \int_b^\infty dt t^{-2/3} \exp(-t) \\ &= -\frac{B}{3b^{1/3}} \Gamma\left(\frac{1}{3}, b\right) \end{aligned} \quad (3.44)$$

where $B = uL_c\varphi_m^2/4\pi$, $b = 4k_0^3/3|\alpha|$, $t = b(1 + k_y^2/k_0^2)^{3/2}$ and

$$\Gamma(\zeta, \xi) = \int_\xi^\infty d\tau \exp(-\tau) \tau^{\zeta-1}$$

is the incomplete gamma function [Abramowitz and Stegun, 1965]. For large ξ , one can write

$$\Gamma(\zeta, \xi) \approx \xi^{\zeta-1} \exp(-\xi)$$

Therefore for small $\alpha \ll 4k_0^3/3$, i.e., large b , the decay rate of vortex energy is

$$\frac{dE_v}{dt} \approx -\frac{uL_c\varphi_m^2|\alpha|}{16\pi k_0^3} \exp\left(-\frac{4k_0^3}{3|\alpha|}\right), \quad (3.45)$$

valid for $k_0^2 > 0$. Thus the damping is exponentially small provided $k_0^3 > 3\alpha/4$, or in terms of the vortex length scale,

$$\rho_{s0} \ll r_0 \sim k_0^{-1} \ll (4/3\alpha)^{1/3} \rho_{s0} \sim \rho_{s0}/\epsilon^{2/3}.$$

The damping time scale τ_L for the decay of the vortex can be estimated by

$$\tau_L = \frac{E_v}{|dE_v/dt|} \approx \frac{2.8\pi^2}{u|\alpha|} \left(\frac{4}{3} + k_0^2\right) \exp\left(\frac{4k_0^3}{3|\alpha|}\right). \quad (3.46)$$

The theory for the effect of the inhomogeneity in Eqs. (3.34)–(3.46) is based on the observation [Horton, 1989] that for strong vortices (ones with $\Omega_E/\omega_k \gg 1$ where Ω_E is the rotation frequency in the core of vortex and $\omega_k \simeq k_y u$), the inhomogeneity causes a leakage of wave energy from the vortex core, but does not strongly alter the interior solution. At some stronger level of inhomogeneity the core of the vortex is changed, and non-perturbative solutions exhibiting the effect of inhomogeneity are required.

3.6 Numerical Simulations

In this section we present the numerical simulation results to give insight into the dynamics of the vortices.

In order to facilitate the numerical solutions of Eq. (3.5), we first expand the equation according to the ordering in Eq. (3.24) and consider $\epsilon_t \sim \epsilon$. Keeping only the terms of order ϵ and ϵ^2 , we derive from Eq. (3.5) the reduced dynamical equation

$$\left(\frac{1}{T(x)} - \nabla^2 \right) \frac{\partial \varphi}{\partial t} + (v_{d0} + v'_{d0}x - \kappa_T \varphi) \frac{\partial \varphi}{\partial y} - [\varphi, \nabla^2 \varphi] = 0, \quad (3.47)$$

which is valid only when the condition of Eq. (3.31) is satisfied.

Rewriting Eq. (3.47), we get the conservation of mass in the two-dimensional system,

$$\frac{\partial}{\partial t} \left(\frac{\varphi}{T(x)} \right) + \nabla \cdot \left[-\frac{\partial \nabla \varphi}{\partial t} + \left(v_d(x) \varphi - \frac{\kappa_T \varphi^2}{2} \right) \hat{\mathbf{y}} + (\nabla \varphi \times \hat{\mathbf{z}}) \nabla^2 \varphi \right] = 0. \quad (3.48)$$

Multiplying Eq. (3.47) by φ , we can derive the energy conservation law given by Eqs. (3.39), (3.40) and (3.41) in the previous section. The constants are subsequently used to monitor the solutions.

To solve Eq. (3.47), we use a uniform grid over x and k_y in 85×85 xk_y -space with 3655 complex $\varphi_{x,k_y}(t)$ modes. Since the first term of Eq. (3.47) depends on x , transforming Eq. (3.47) into $k_x k_y$ space would lead to a difficult convolution integral in k_x for the linear problem. Leaving the equation in x space and using the second order central difference formula for ∂_x^2 , gives a tri-diagonal system to solve for each $\partial_t \varphi(x, k_y, t)$. We use the Ahlberg-Nilson-Walsh algorithm for cyclic tri-diagonal systems [Temperton, 1975] to reduce the operator $(1/T(x) - \nabla^2)$ to a cyclic tri-diagonal matrix and then compute $\partial \varphi / \partial t$ for each mode, in which process the nonlinear convolution terms in Eq. (3.47) are evaluated by first transforming φ in $k_x k_y$ space to get derivatives of φ , then transforming φ and its derivatives into xy space to calculate the convolutions and, after that, transforming the results back into xk_y space. Finally, we use the fifth and sixth order Runge-Kutta time stepping and the Fourier Transformation $y \leftrightarrow k_y$ at each time step. The code to do the time integration is DVERK of commercial IMSL math package. The constants of motion defined in Eqs. (3.39) and (3.48) are used to monitor the accuracy of the code. The approximate monopole solution Eq. (3.26) is taken as the initial condition $\varphi(x, y, t = 0)$. The temperature profile is $T(x) = \exp(-c_2 x)$, which avoids the negative temperature problem that arises when expanding $T(x)$ as $1 - c_2 x$. For this profile $\kappa_T = c_2 \exp(c_2 x)$. Typical simulations average 15 minutes CPU time on the CRAY-2 for $\Delta t = 100 r_n / c_s$, which is about 10 rotations of the vortex core.

In the first case we used $v'_{d0} = -0.1v_{d0}$, $u = 1.1v_{d0}$ and $c_2 = -0.011$, which give $k_0^2 = (1 - v_{d0}/u) \simeq 0.1$ and $\alpha \simeq (c_2 - v'_{d0}/u) \simeq 0.08$. Therefore α is the same order as k_0^3 ($k_0^3/\alpha \simeq 0.34$). We observe the forming of a oscillating tail

with significant amplitude and a strong damping process of the monopole vortex. Figure 3.7 shows the streamline of $\varphi(x, y, t) = \text{const.}$ at times $tc_s/r_n = 0, 40$ and 60 , and the projections of their cross sections in the x and y directions. The particle density is, from Eq. (3.30), $n/n_0 \approx \exp(\epsilon_n \varphi_m) \approx 1.7$ at the maximum point of the vortex.

In the second case $v'_{d0} = 0.05v_{d0}$, $u=1.1v_{d0}$ and $c_2=0.046$, and thus $\alpha \simeq 0.0006$ and $k_0^3 \simeq 0.027$ so that $k_0^3/\alpha \sim 45$. We can see in Fig. 3.8 that the amplitude of the oscillating tail is so insignificant that the monopole vortex keeps its shape for a long time without much damping. The particle density in this case is $n/n_0 \simeq 0.58$ at the deepest negative amplitude of the vortex. The question of electron trapping in such vortices is addressed by Jovanovic and Horton [1992].

Although in the first and second cases above, we discussed only the anticyclone vortex ($\varphi > 0$) in the first case, and only the cyclone vortex ($\varphi < 0$) in the second case, the same results are obtained for the cyclone vortex in the first case and the anticyclone vortex in the second case, because Eq. (3.47) possesses the following symmetry relation

$$\varphi(\kappa_T, v'_{d0}; x, y, t) = -\varphi(-\kappa_T, -v'_{d0}; -x, y, t) .$$

In Fig. 3.9, we used the same parameters and initial condition as those in Fig. 3.8, but dropped the scalar nonlinear term with coefficient κ_T in Eq. (3.47). The monopole vortex in this case is seen to connect to a radiation wake.

These numerical results support our arguments that when the drift velocity depends on the space variable, monopole-like vortices can exist in the

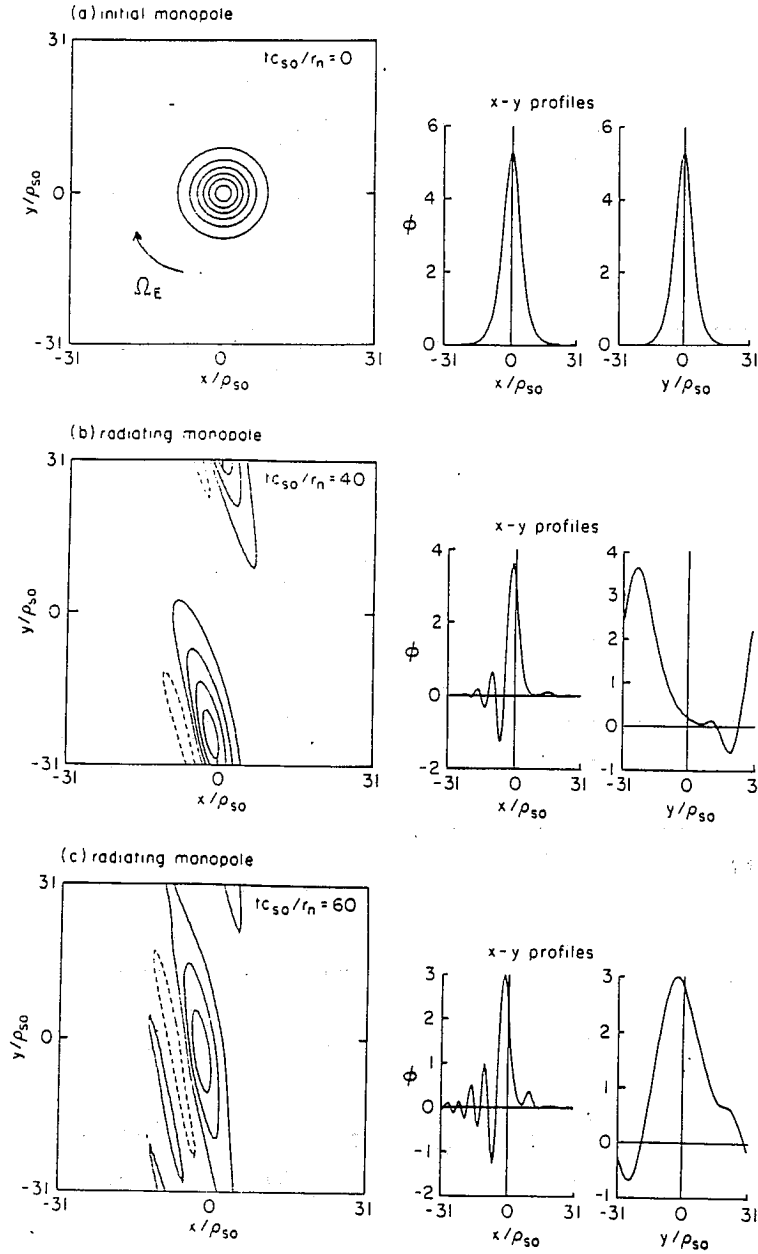


Figure 3.7: Contour plot of the electrostatic potential $\varphi(x, y, t)$ with strong radiation damping.

(a) The initial condition is a monopole defined by Eq. (3.26). (b) At $t = 40 r_n / c_s$, the monopole vortex core is coupling to an oscillating tail, *i.e.* a radiative wake of drift waves. (c) At $t = 60 r_n / c_s$, the monopole vortex has been strongly distorted and the amplitude has been significantly decreased from $5.28(T_0/e)(\rho_{s0}/r_n)$ at beginning to $3(T_0/e)(\rho_{s0}/r_n)$, due to the strong damping.

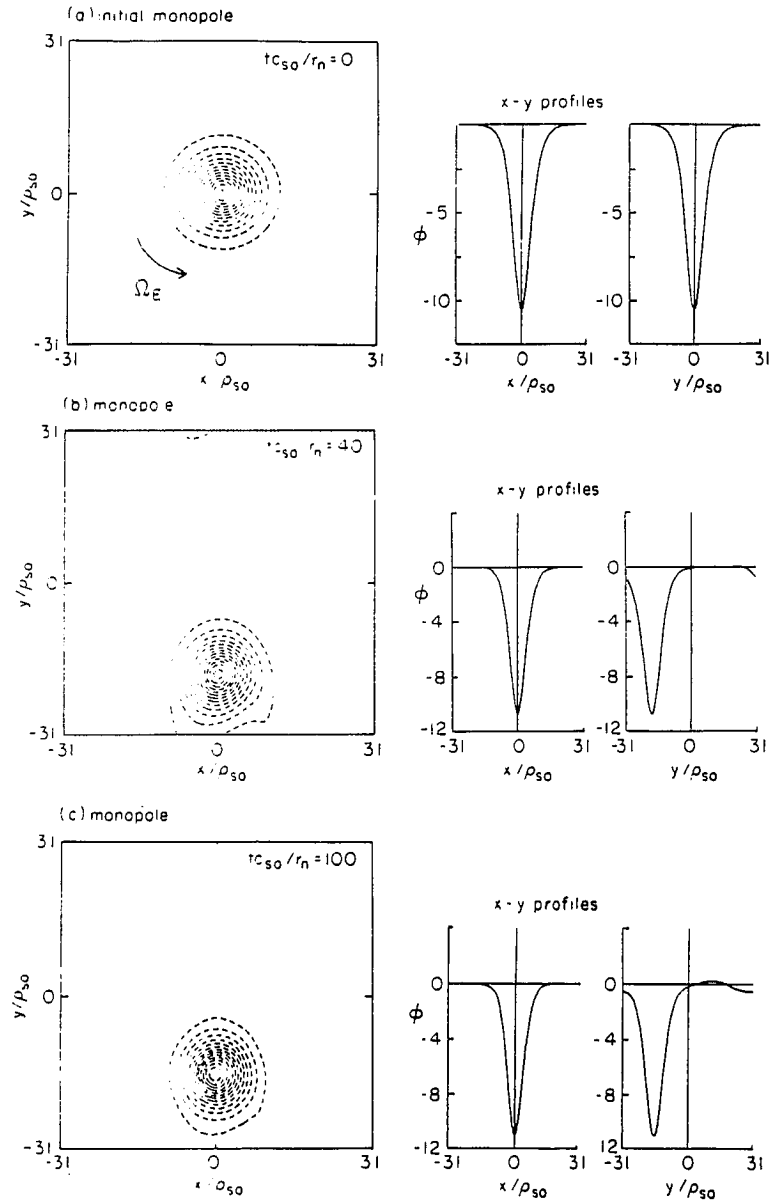


Figure 3.8: Contour plot of the electrostatic potential $\varphi(x, y, t)$ with weak damping.

(a) the contours of $\varphi(x, y, t)$ at $t = 0$ show the initial state given by Eq. (3.26). (b) At $t = 40r_n/c_s$, the amplitude of the oscillating tail is too small to be noticed. (c) and (d) At $t = 80r_n/c_s$ and $100r_n/c_s$, the monopole vortex keeps its shape with very slight distortion in the exterior region and the amplitude has no significant change.

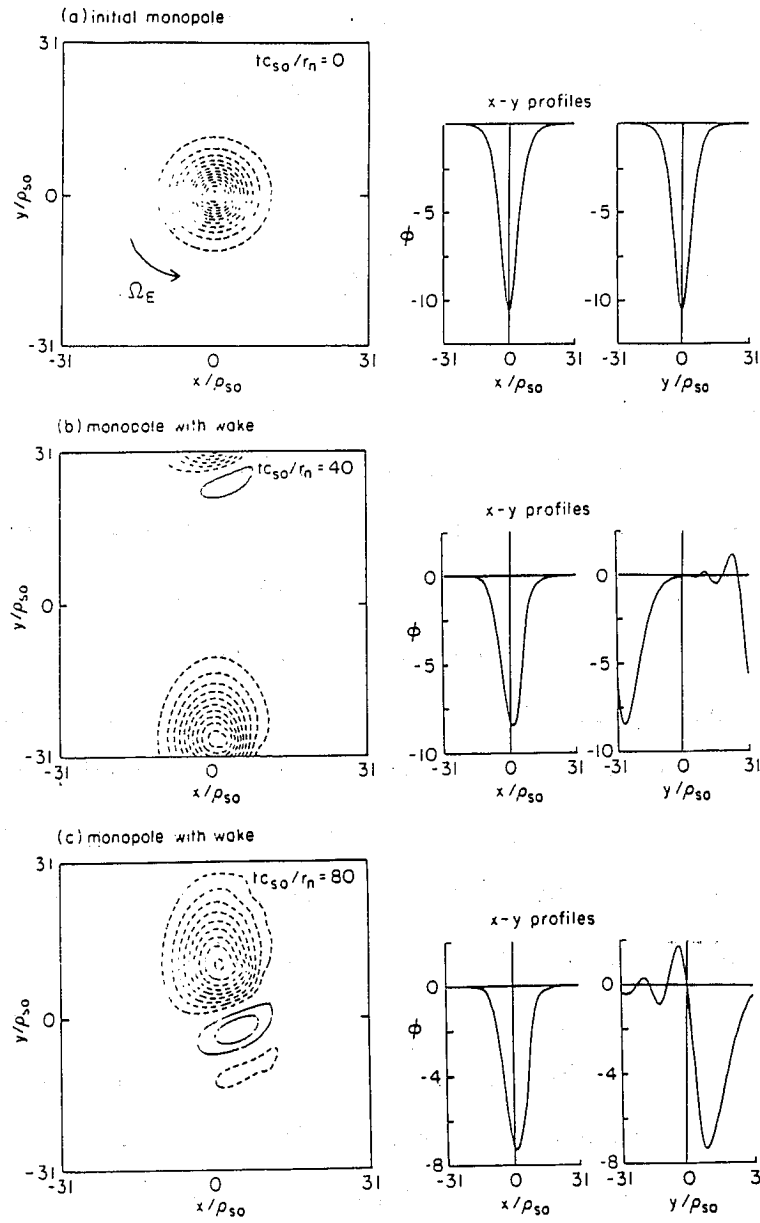


Figure 3.9: Monopole vortex with a radiation wake.

The parameters and the initial condition are same as those in Fig. 3.8, but the scalar nonlinear term with coefficient κ_T in Eq. (3.47) is dropped. The monopole vortex in this case is shown to connect to a radiation wake.

wavelength $\sim (\rho_s r_n)^{1/2}$ region. The simulations also verify that the stability of the vortices is affected by the combined effect of temperature and drift velocity gradients and that the vortices are stable or free of damping only when $\alpha \ll (4/3)k_0^3$.

3.7 Summary and Conclusions

We have studied the effect of density and temperature gradients on drift wave vortices, both analytically and numerically. The results show that when the drift wave velocity v_d does not depend on the space variable, localized monopole vortices can not be formed in the long wavelength $\sim (\rho_s r_n)^{1/2}$ region for the choice of $F = 1/n_0(x - \varphi/u)$ given in Eq. (3.10) by continuation from the form of $F(x) \rightarrow n_0(x)$ as $x \rightarrow \infty$ and $\varphi \rightarrow 0$, no matter what the temperature profile is. When the drift wave velocity is not constant, monopole vortex solutions can be found in the wavelength $\sim \rho_s/\epsilon^{1/2}$ region. However, the important result is that the monopole vortices are not the strictly localized monopoles found by many other authors [Lakhin *et al.*, 1987 and 1988; Horiata and Sato, 1987; Spatschek *et al.*, 1990]. Although the gradient of the drift velocity is responsible for the formation of the monopole vortices, its existence also causes the formation of the oscillating tails or radiative wakes of drift waves, which connect to the cores of the vortices. The results show that as long as $\alpha \equiv (\kappa_T - v'_{d0}/u) \neq 0$, the wave energy of the vortices leaks out from the vortex cores through the oscillating tails. The effect of the temperature gradient here is to reduce the energy leakage. The analytic and numerical results also show that only when the combined effect of the temperature and the drift velocity gradients satisfies $\alpha \equiv (\kappa_T - v'_{d0}/u) \ll (4/3)(1 - v_{d0}/u)^{3/2}$,

will the leakage be small and negligible.

Chapter 4

Nonlinear Drift Wave Coherent Structures in a Sheared Magnetic Field

4.1 Introduction

Since the solitary dipole vortex solutions, also called modons, were found [Larichev and Reznik, 1976] for the Hasegawa-Mima [1977 and 1978] (H-M) drift wave equation in a uniform plasma, numerous works have concerned solitary vortex solutions in nonuniform plasmas. Petviashvili [1977] first suggested that if the H-M equation is modified by including the effect of the electron temperature gradient, one can derive solitary monopole vortex solutions. The derivation of the original Petviashvili model [Petviashvili, 1977], however, has been shown to be incomplete recently by several authors [Lakhin *et al.*, 1987 and 1988; Horihata and Sato, 1987; Nycander, 1989; Su *et al.*, 1991]. In particular, the full analysis shows that non-locality of the linear wave operator must be retained simultaneously with the KdV-type nonlinearity introduced by Petviashvili [1977], in order to preserve the conservation of potential vorticity. The authors have shown that for a plasma with constant drift velocity v_d , there exist no monopole vortex solutions, no matter what the temperature profile, $T(x)$; but monopole solutions can exist if the drift velocity is not constant $v_d(x)$. In Chapter 3, we have considered a fully nonlinear model with a Boltzmann density distribution and have concluded that the monopole-like vortices can exist if the temperature and drift velocity are not constant. Such monopole-

like vortices are not exponentially localized soliton-like monopoles since the inhomogeneity also causes energy leakage from the vortex core through radiative tails. This leakage will be negligible if the strength of the inhomogeneity $\alpha = |T'/T^2 - v'_{d0}/u|$ and size of the vortex $1/k_0$ (where $k_0 \equiv \sqrt{1 - v_{d0}/u}$) satisfy $\alpha \ll k_0^3$.

In the previous chapters as well as all previous works by many authors (for examples: Petviashvili, 1977; Makino *et al.*, 1981; Lakhin *et al.*, 1987 and 1988; Horihata and Sato, 1987; Spatschek *et al.*, 1990), the spatial dependence of k_{\parallel} is ignored, and consequently the effects of magnetic shear are systematically eliminated. The present chapter extends previous chapters by taking into account the nonlinear coupling of vorticity to the magnetic shear induced parallel ion motion. Here a model that includes not only the temperature and density gradients, but also the effect of magnetic shear is developed and analyzed. Analytically we consider a quasi-one-dimensional model for the finite amplitude coherent structures that exhibits a nonlinear localization mechanism. With this model we are able to show that when the effect of magnetic shear is included in the drift wave equation, even without the gradient of drift velocity, the effective potential becomes a nonlinear trapping potential and, therefore, there exist solitary solutions. The solutions are shown to be dipole-like solitary waves. However, they are different from the well-known modons which are exact solutions of the H-M equation. Due to the coupling of drift waves to ion acoustic waves, the solitary structures, like those induced by nonconstant drift velocity in a shearless field studied in Chapter 3, are not exponentially localized soliton-like solutions; instead they have oscillating tails which connect to the cores of the vortices. We also use two-dimensional magneto-hydrodynamic

type of numerical code to simulate the coupled vorticity and parallel velocity fields. The numerical results are consistent with the analytic results obtained from the quasi-one-dimensional model.

This chapter is organized as follows. In Sec. 4.2 the model equations are derived and the conservation laws are presented. In Sec. 4.3 the model equations are analyzed. Section 4.4 is devoted to the studies of properties of the coherent structures in sheared magnetic field. The numerical results are presented and discussed in Sec. 4.5. The summary and conclusions are given in Sec. 4.6.

4.2 Theoretical Model and Conservations

We consider a plasma of cold ions and massless electrons in a sheared external magnetic field $\mathbf{B} = B_0(\hat{\mathbf{z}} + \mathcal{S}(x/L_s)\hat{\mathbf{y}}) = B_0\hat{\mathbf{b}}$. The dissipationless equation of motion and the continuity equation for the ions are

$$\frac{d\mathbf{v}}{dt} = -\frac{e}{m_i} \nabla\Phi + \mathbf{v} \times \boldsymbol{\Omega} , \quad (4.1)$$

$$\frac{\partial n}{\partial t} + \nabla \cdot (n\mathbf{v}) = 0 , \quad (4.2)$$

where $d/dt = \partial/\partial t + \mathbf{v} \cdot \nabla$, and $\boldsymbol{\Omega} = e\mathbf{B}/m_i c = \omega_{ci}\hat{\mathbf{b}}$ is the ion cyclotron frequency. Upon taking the curl of Eq. (4.1) and combining with Eq. (4.2), one can derive the inhomogeneous Ertel's theorem,

$$\frac{d}{dt} \left(\frac{\boldsymbol{\Omega} + \boldsymbol{\omega}}{n} \right) = \left(\frac{\boldsymbol{\Omega} + \boldsymbol{\omega}}{n} \right) \cdot \nabla \mathbf{v} , \quad (4.3)$$

where $\boldsymbol{\omega} = \nabla \times \mathbf{v}$.

Introducing the ordering,

$$\epsilon_t \equiv \frac{1}{\omega_{ci}} \frac{\partial}{\partial t} \sim \frac{\mathbf{v} \cdot \nabla}{\omega_{ci}} \sim \frac{\nabla_{\parallel} v_{\parallel}}{\omega_{ci}} \ll 1 ,$$

we obtain from Eq. (1) to lowest order in ϵ_i

$$\mathbf{v} = \mathbf{v}_\perp = \left(\frac{e}{m_i \omega_{ci}} \right) \hat{\mathbf{z}} \times \nabla \Phi$$

$$\omega = \omega_{ci} \frac{\rho_s^2}{T_e} \nabla_\perp^2 (e\Phi) \hat{\mathbf{z}}$$

and the convective derivative becomes

$$\frac{d}{dt} = \frac{\partial}{\partial t} + \mathbf{v}_\perp \cdot \nabla = \frac{\partial}{\partial t} + \omega_{ci} \frac{\rho_s^2}{T_e} [e\Phi, \] ,$$

where $\rho_s = c_s/\omega_{ci}$ and $c_s = (T_e(x)/m_i)^{1/2}$. Now we define $T(x) = T_e(x)/T_0$ (where T_0 is a constant), $r_n^{-1} = -d \ln n_0 / dx$, $\epsilon_n = \rho_{s0}/r_n$, $\rho_{s0} = c_{s0}/\omega_{ci} = (T_0/m_i)^{1/2}/\omega_{ci}$ and the magnetic shear strength $S(x) = (r_n/\rho_{s0})\mathcal{S}(\rho_{s0}x/L_s)$. The parallel component of the vorticity equation from Eq. (4.3) can now be written as

$$\frac{\partial}{\partial t} \ell n \left(\frac{1 + \epsilon_n \nabla_\perp^2 \varphi}{n} \right) + \left[\varphi, \ell n \left(\frac{1 + \epsilon_n \nabla_\perp^2 \varphi}{n} \right) \right] = \left(\frac{\partial}{\partial z} + S(x) \frac{\partial}{\partial y} \right) \epsilon_n v_\parallel , \quad (4.4)$$

and the parallel component of the momentum equation from Eq. (4.1) is

$$\frac{\partial v_\parallel}{\partial t} + [\varphi, v_\parallel] = - \left(\frac{\partial}{\partial z} + S(x) \frac{\partial}{\partial y} \right) \varphi . \quad (4.5)$$

For the massless electrons, we assume the Boltzmann distribution

$$n = n_0(x) \exp \left(\frac{e\Phi}{T_e} \right) = n_0(x) \exp \left(\frac{\epsilon_n \varphi}{T} \right) . \quad (4.6)$$

In writing Eqs. (4.4)–(4.6), we have used the following scaling transformations to dimensionless variables:

$$x, y = x/\rho_{s0}, y/\rho_{s0} ;$$

$$z = z/r_n ;$$

$$t = c_{s0}t/r_n ;$$

$$v_{\parallel} = (r_n/\rho_{s0})(v_{\parallel}/c_{s0}) ;$$

$$\varphi = (r_n/\rho_{s0})(e\Phi/T_0) .$$

Upon substitution Eq. (4.6) into Eq. (4.4) and considering the ordering

$$\frac{r_n}{c_{s0}} \frac{\partial}{\partial t} \sim \rho_{s0}^2 \nabla_{\perp}^2 \sim r_n \nabla_{\parallel} \sim \frac{e\Phi}{T} \sim \frac{v}{c_{s0}} \sim \frac{\rho_{s0}}{r_n} \equiv \epsilon_n \sim \epsilon , \quad (4.7)$$

we can rewrite Eq. (4.4) to order ϵ and ϵ^2 as

$$\left(\frac{1}{T} - \nabla^2 \right) \frac{\partial \varphi}{\partial t} + v_d \frac{\partial \varphi}{\partial y} - \kappa_T \varphi \frac{\partial \varphi}{\partial y} - [\varphi, \nabla_{\perp}^2 \varphi] = - \left(\frac{\partial}{\partial z} + S(x) \frac{\partial}{\partial y} \right) v_{\parallel} , \quad (4.8)$$

where $v_d(x) = -d\ell n n_0/dx \sim \mathcal{O}(1)$ and $\kappa_T(x) = -(1/T)d\ell n T/dx \sim \mathcal{O}(\epsilon)$.

Now the conservation law for mass is evident by rewriting Eq. (4.8) as

$$\begin{aligned} \frac{\partial}{\partial t} \left(\frac{\varphi}{T(x)} \right) + \nabla \cdot \left[- \frac{\partial \nabla \varphi}{\partial t} + \left(v_d(x) \varphi - \frac{\kappa_T(x) \varphi^2}{2} \right) \hat{\mathbf{y}} \right. \\ \left. + (\nabla \varphi \times \hat{\mathbf{z}}) \nabla^2 \varphi + v_{\parallel} \hat{\mathbf{b}} \right] = 0 , \end{aligned} \quad (4.9)$$

and momentum conservation by rewriting Eq. (4.5) as

$$\frac{\partial}{\partial t} v_{\parallel} + \nabla \cdot [(\nabla \varphi \times \hat{\mathbf{z}}) v_{\parallel} + \varphi \hat{\mathbf{b}}] = 0 . \quad (4.10)$$

The conservation law for energy can be obtained by multiplying Eq. (4.5) by v_{\parallel} and Eq. (4.8) by φ and then combining the two equations to get

$$\begin{aligned} \frac{\partial \mathcal{E}}{\partial t} + \nabla \cdot \left[\left(\frac{v_d(x)}{2} \varphi^2 - \frac{\kappa_T(x)}{3} \varphi^3 \right) \hat{\mathbf{y}} - \varphi \nabla \frac{\partial \varphi}{\partial t} - \nabla^2 \varphi \left(\hat{\mathbf{z}} \times \nabla \frac{\varphi^2}{2} \right) \right. \\ \left. + (\varphi v_{\parallel}) \hat{\mathbf{b}} \right] = 0 , \end{aligned} \quad (4.11)$$

where the energy density \mathcal{E} is defined as

$$\mathcal{E}(x, y, t) = \frac{1}{2} \left[\frac{\varphi^2}{T(x)} + (\nabla \varphi)^2 + v_{\parallel}^2 \right].$$

Therefore, Eqs. (4.9), (4.10) and (4.11) show that the dynamical system conserves mass, momentum and energy to the second order in ϵ .

Equation (4.4) describes the advection of the generalized potential vorticity and its change caused by parallel compression $\nabla_{\parallel} v_{\parallel}$. The compression from the parallel motion eliminates the conservation of potential enstrophy, defined as

$$U = \int (\nabla_{\perp} \varphi)^2 + (\nabla_{\perp}^2 \varphi)^2 dx dy.$$

However, the generalized cross helicity appears as constant of motion. To systematically construct the invariants, the so-called Casimir noncanonical Hamiltonian structure is developed in Appendix A. Here we observe that if we introduce the antiderivative of the shear

$$\sigma(x) = \int^x S(x') dx'$$

such that $[\sigma(x), v_{\parallel}] = S(x) \partial v_{\parallel} / \partial y$ and the potential vorticity $q = \nabla^2 \varphi - \varphi / T(x) - \ell n n_0(x)$, then it is straightforward to show that the conserved helicity is

$$h = \int q (v_{\parallel} - \sigma(x)) dx dy dz. \quad (4.12)$$

A generalization of this invariant in the case where z -dependence is neglected is given in Appendix A.

4.3 Analytical Stationary Solitary Wave Solutions

Now we look for traveling wave solutions of Eqs. (4.4) and (4.5) by assuming $\varphi = \varphi(x, y - ut)$ and $v_{\parallel} = v_{\parallel}(x, y - ut)$. Equations (4.4) and (4.5)

become

$$-u \frac{\partial}{\partial y} \ell n \left(\frac{1 + \epsilon_n \nabla^2 \varphi}{n} \right) + \left[\varphi, \ell n \left(\frac{1 + \epsilon_n \nabla^2 \varphi}{n} \right) \right] = \epsilon_n S(x) \frac{\partial v_{\parallel}}{\partial y}, \quad (4.13)$$

$$-u \frac{\partial v_{\parallel}}{\partial y} + [\varphi, v_{\parallel}] = -S(x) \frac{\partial \varphi}{\partial y}. \quad (4.14)$$

Equation (4.14) gives

$$\left[\varphi - ux, v_{\parallel} + \sum_{n=1}^{\infty} (-1)^n \frac{d^{(n-1)} S(x) / dx^{(n-1)}}{n! u^n} \varphi^n \right] = 0, \quad (4.15)$$

which has the general solution

$$v_{\parallel} - \frac{S_1 x}{u} \varphi + \frac{S_1}{2u^2} \varphi^2 = G(\varphi - ux), \quad (4.16)$$

where G is an arbitrary function of its argument. In writing Eq. (4.16), we have expanded

$$S(x) = S_0 + S_1 x + S_2 x^2 + \dots$$

with $S_0 = 0$ and noticed that the higher order derivatives of $S(x)$ are significantly smaller than the first order derivative for the magnetic shear problem.

For localized solutions $\varphi \rightarrow 0$ as $r \rightarrow \infty$ and we assume the boundary condition $v_{\parallel} \rightarrow v_{\infty} = \text{constant}$ as $r \rightarrow \infty$. Assuming $G(\infty) = v_{\infty}$, v_{\parallel} can be written as

$$v_{\parallel} = \frac{S_1 x}{u} \varphi - \frac{S_1}{2u^2} \varphi^2 + v_{\infty}, \quad (4.17)$$

where we see that the magnetic shear introduces an important nonlinearity into the dependence of v_{\parallel} on φ .

Substituting Eq. (4.17) into Eq. (4.13), we obtain another condition

$$\left[\varphi - ux, \ell n \left(\frac{1 + \epsilon_n \nabla^2 \varphi}{n} \right) + \frac{\epsilon_n S_1^2 x^2}{u^2} \varphi - \frac{3\epsilon_n S_1^2 x}{2u^3} \varphi^2 + \frac{\epsilon_n S_1^2}{2u^4} \varphi^3 \right] = 0. \quad (4.18)$$

which has the general solution

$$\begin{aligned} \ell n \left(1 + \epsilon_n \nabla^2 \varphi \right) - \ell n n_0 - \frac{\epsilon_n \varphi}{T(x)} + \frac{\epsilon_n S_1^2 x^2}{u^2} \varphi - \frac{3 \epsilon_n S_1^2 x}{2u^3} \varphi^2 \\ + \frac{\epsilon_n S_1^2}{2u^4} \varphi^3 = F(\varphi - ux) , \end{aligned} \quad (4.19)$$

where we have assumed quasi-neutrality with the electrons obeying the Boltzmann distribution of Eq. (4.6). Again we see that the presence of magnetic shear introduces important strong nonlinearities into the system.

To insure localization for φ we select

$$F(\varphi - ux) = -\ell n n_0 \left(\frac{ux - \varphi}{u} \right) . \quad (4.20)$$

For a simple exponential density profile, $n_0(x) = \exp(-\epsilon_n x)$, and constant temperature ($T = 1$), Eq. (4.19) with Eq. (4.20) becomes

$$\epsilon_n \nabla^2 \varphi = \exp \left[\epsilon_n \left(1 - \frac{v_d}{u} \right) \varphi - \epsilon_n S_1^2 \left(\frac{x^2}{u^2} \varphi - \frac{3x}{2u^3} \varphi^2 + \frac{\varphi^3}{2u^4} \right) \right] - 1 , \quad (4.21)$$

where $v_d = 1$ follows from the choice of units.

Considering the quasi-one-dimensional case in which $\partial/\partial y \ll \partial/\partial x$ and introducing the new variables

$$k^2 = 1 - \frac{1}{u} , \quad x = \frac{t}{k} , \quad \varphi = \frac{u}{k} \Psi , \quad s^2 = \frac{S_1^2}{2u^2 k^4} , \quad \epsilon_0 = uk\epsilon_n ,$$

we obtain

$$\epsilon_0 \frac{\partial^2 \Psi}{\partial t^2} = \exp \left[\epsilon_0 \left(\Psi - s^2 (2t^2 \Psi - 3t \Psi^2 + \Psi^3) \right) \right] - 1 . \quad (4.22)$$

Here, note that for small k^2 , corresponding to large coherent structures, the effective shear parameter s^2 is considerably enhanced over the original shear parameter S_1^2 .

The boundary condition:

$$\Psi(t \rightarrow \pm\infty) \rightarrow 0$$

and the initial conditions:

$$\Psi(t = 0) = 0 \quad \text{and} \quad d\Psi(t = 0)/dt = \text{const.}$$

or

$$\Psi(t = 0) = \text{const.} \quad \text{and} \quad d\Psi(t = 0)/dt = 0$$

together with Eq. (4.22) define a nonlinear eigenvalue problem for the unknown constant values at $t = 0$.

In the new variables we can calculate the nonlinear rotation rate [Horton, 1989] $\Omega_E = (c_s/r_n)k_y d\varphi/dx$ compared to the vortex frequency $\omega_{\text{lab}} = (c_s/r_n)k_y u$ in the laboratory frame as

$$\Omega_E/\omega_{\text{lab}} = d\Psi/dt .$$

Equation (4.22) can be written in the form of the Hamiltonian equations for an imaginary particle with coordinate $q = \Psi$, time t , and momentum $p = \partial\Psi/\partial t$ in the effective potential

$$V_{\text{eff}}(\Psi, t) = -\frac{1}{\epsilon_0} \int^{\Psi} d\Psi \exp \left[\epsilon_0 \left(\Psi - s^2(2t^2\Psi - 3t\Psi^2 + \Psi^3) \right) \right] + \frac{\Psi}{\epsilon_0} , \quad (4.23)$$

For $u \sim v_d = 1$, $\epsilon_0 \sim \epsilon_n^2 \ll 1$ and the effective potential reduces to

$$V_{\text{eff}}(\Psi, t) \approx - \left[\frac{\Psi^2}{2} - s^2 \left(t^2\Psi^2 - t\Psi^3 + \frac{\Psi^4}{4} \right) \right] . \quad (4.24)$$

Although for simplicity in Eq. (4.24) we have kept only the lowest order of V_{eff} in ϵ_0 , it can easily be shown that this approximation does not change the shape of V_{eff} .

The dynamical equations for a “particle” representing the system are

$$\dot{p} = -\frac{\partial}{\partial \Psi} V_{\text{eff}}(\Psi, t) = \Psi - s^2(2t^2\Psi - 3t\Psi^2 + \Psi^3) , \quad (4.25)$$

$$\dot{\Psi} = p . \quad (4.26)$$

In order for Eq. (4.22) to have localized solutions, the effective potential must be a trapping potential. In the limit of $s \rightarrow 0$ the effective potential has the form

$$V_{\text{eff}}(s = 0) = \Psi - (1/\epsilon_0)e^{\epsilon_0\Psi}$$

or to lowest order

$$V_{\text{eff}}(s = 0) \approx -(1/2)\Psi^2 ,$$

which is easily seen to not be a trapping potential. However, with existence of small shear s , the situation is changed entirely. To realize this, one can examine the properties of V_{eff} . The extremal points of the potential are given by

$$-\frac{\partial V_{\text{eff}}}{\partial \Psi} = \Psi - s^2(2t^2\Psi - 3t\Psi^2 + \Psi^3) = 0$$

which yields

$$\Psi_{m1} = 0 ,$$

$$\Psi_{m2} = (3/2)t - (1/2)\sqrt{t^2 + 4/s^2} ,$$

$$\Psi_{m3} = (3/2)t + (1/2)\sqrt{t^2 + 4/s^2} .$$

The signs of second derivative $\partial^2 V_{\text{eff}}/\partial \Psi^2$ at the extremal points determine the shape of the potential. Figure 4.1 is a sketch of the evolution of the effective potential with “time” t . Figure 4.2 displays corresponding phase space portraits

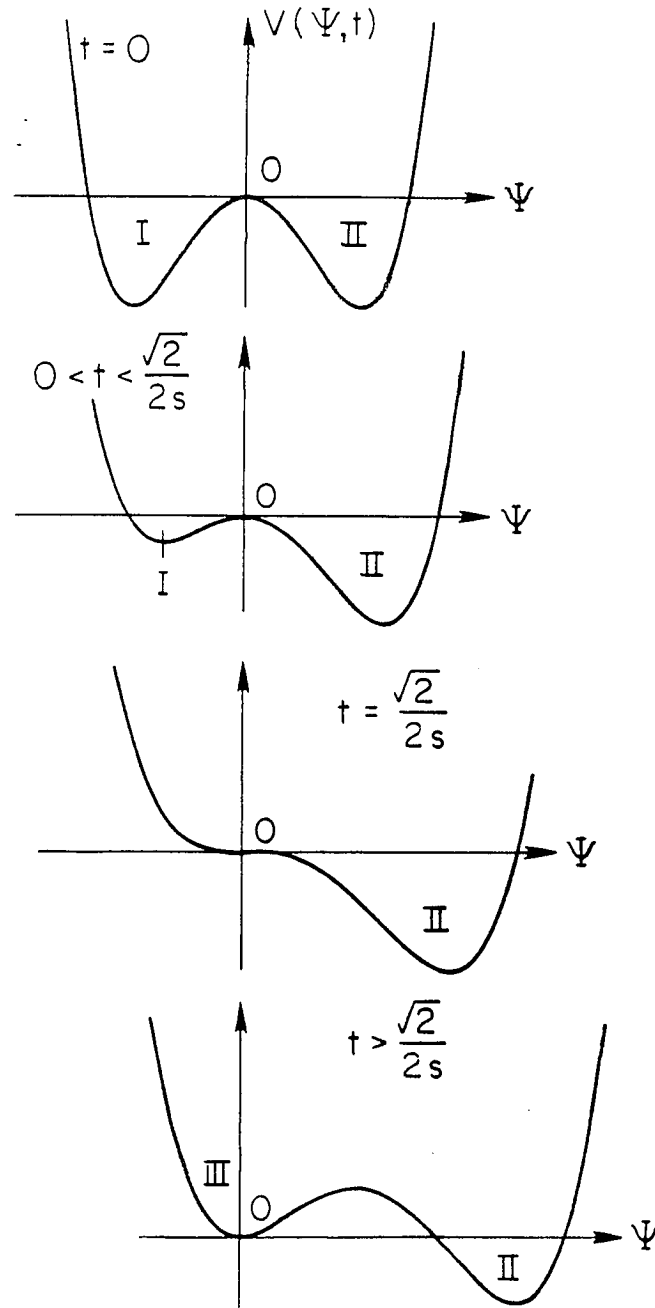


Figure 4.1: Evolution of effective potential $V_{\text{eff}}(\Psi, t)$ with the “time” t . The “time” t corresponds to the distance kx from the shear reversal point.

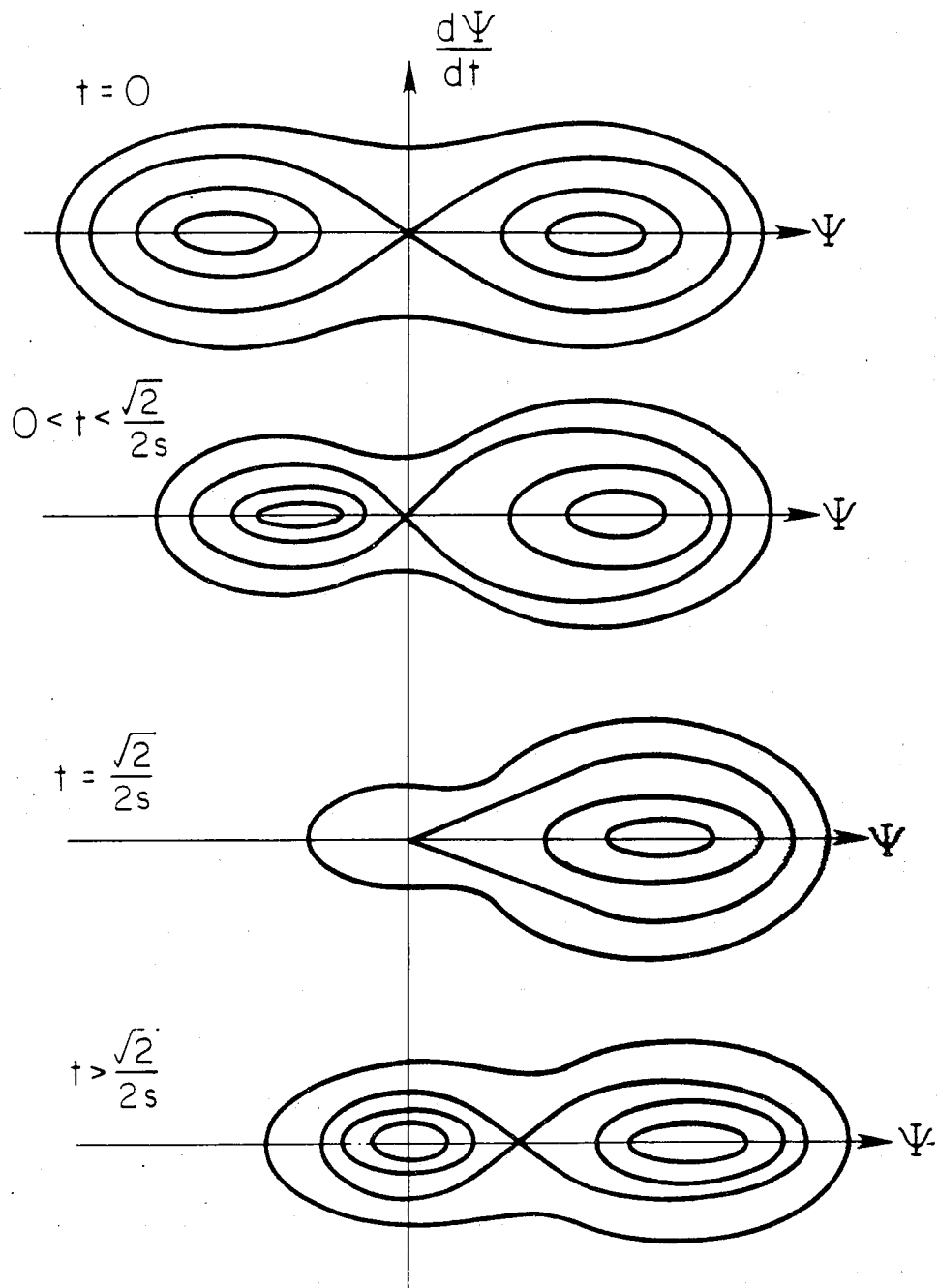


Figure 4.2: Evolution of the separatrix in phase space corresponding to the effective potential $V_{\text{eff}}(\Psi, t)$

showing the bifurcation of the origin from unstable to stable at $t = \sqrt{2}/2s$. It is evident that the effective potential has two wells when $t = 0$, indicated by I and II in Fig. 4.1. Well I moves to $\Psi = 0$ and disappears as $t \rightarrow \sqrt{2}/2s$ and then a new trapping Well III appears and stays at $\Psi = 0$ for $t > \sqrt{2}/2s$, while Well II moves towards $\Psi \rightarrow \infty$ as $t \rightarrow \infty$. For $t < 0$, Well II moves to $\Psi = 0$ and disappears as $t \rightarrow -\sqrt{2}/2s$ and a new trapping Well III appears and stays at $\Psi = 0$ for $t < -\sqrt{2}/2s$, while Well I moves towards $\Psi \rightarrow -\infty$ as $t \rightarrow -\infty$. Therefore only a “particle” eventually trapped in Well III corresponds to a solution satisfying the boundary conditions. The initial conditions determine if the “particle” will be eventually trapped in the Well III.

The presence of the trapping well indicates that the existence of magnetic shear changes the effective potential from nontrapping to trapping, and therefore creates the possibility of solitary wave solutions with finite amplitudes. However, the presence of magnetic shear also makes the solitary drift wave couple to the ion acoustic wave by changing the effective potential $V_{\text{eff}}(\Psi, t)$ at the critical “time” $t_0 = \pm\sqrt{2}/2s$. The new trapping Well III that appears when $|t| > |t_0|$ actually is the potential well associated with the ion acoustic wave. The coupling between the solitary waves and the propagating ion acoustic waves leads to the formation of the oscillating tail emanating from the core of vortex. This tail gives rise to the dissipation of energy from the solitary wave core. Therefore, for a solitary vortex solution, the oscillating tail must be far away from the core of vortex, that is, $t_0 > 1$ or $x_0 > 1/k$, where $1/k$ is the size of the solitary vortex. This gives

$$s < \sqrt{2}/2 \quad \text{or} \quad S_1 < |u - v_d|, \quad (4.27)$$

which is consistent with the condition for a modon with small damping given earlier by Meiss and Horton [1983].

Equations (4.24) and (4.25) are symmetric under the following transformations:

$$\begin{aligned} V_{\text{eff}}(\Psi, t) &\longrightarrow V_{\text{eff}}(-\Psi, -t) , \\ \Psi(t) &\longrightarrow -\Psi(-t) . \end{aligned} \tag{4.28}$$

These relations rule out the possibility of monopole solutions, since these are symmetric about $t = 0$. However, localized solutions in the form of dipoles are not ruled out. The shape of such a dipole is determined by the initial conditions $\Psi(t = 0) = 0$ and $d\Psi(t = 0)/dt = \text{constant}$ corresponding to the strength of the core electric field or $\mathbf{E} \times \mathbf{B}$ flow velocity. Numerical integration of Eq. (4.25) yields the spectrum of eigenvalues for the initial momentum $d\Psi(t = 0)/dt$ or equivalently $(1/u)d\phi(x = 0)/dx$. Solutions are constructed by choosing the initial condition of zero coordinate and nonzero momentum, and then integrating beyond $t_0 = \pm\sqrt{2}/2s$ to determine if there is trapping as $t \rightarrow \pm\infty$ in the ion acoustic potential well. Physically the trapping implies the radiative tail at large t .

Figure 4.3 shows an example of a nonlinear trapping solution for $s = 0.06$. Clearly the trapping solutions of this form only occur for certain initial data, which depend on the shear parameter s . The magnitude of $d\Psi(t = 0)/dt$ and the initial amplitude Ψ_m of the vortex can be estimated with the help of Eq. (4.25). For small $t \leq t_m \sim \epsilon_0 < 1$, where t_m is the “time” at which Ψ assumes its maximum value or amplitude $\Psi_m \equiv \Psi(t = t_m)$ and $d\Psi(t = t_m)/dt = 0$, the second and third terms on the right side of Eq. (4.25) are much

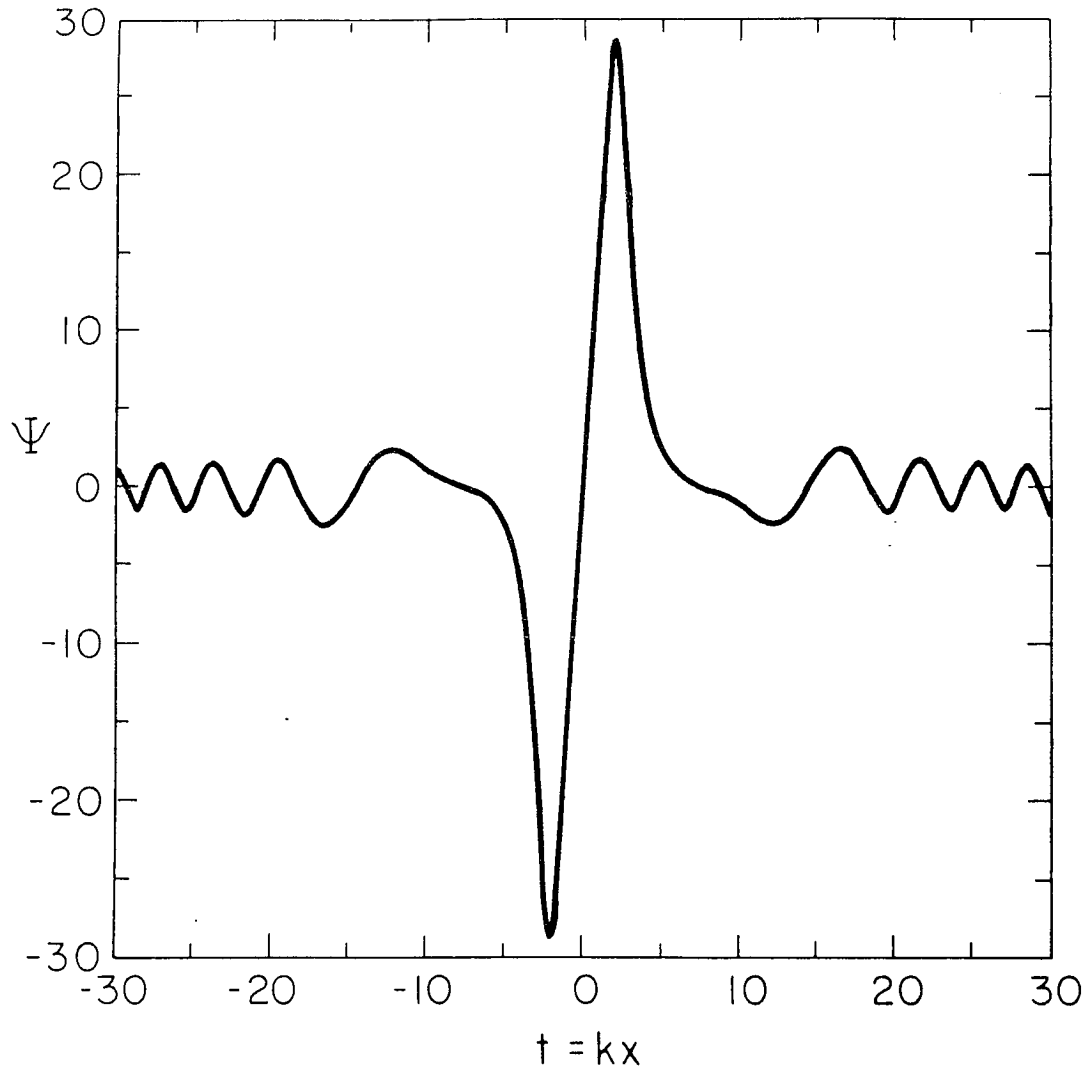


Figure 4.3: A typical nonlinear eigenfunction with magnetic shear.

In this case $s = 0.06$ and $d\Psi(t = 0)/dt = 13.58$, the eigenfunction appears to be the dip-type solitary wave solution.

less than the first and fourth. Therefore for a nonlinear solitary solution, there must be a balance between the linear and nonlinear terms on Eq. (4.25), that is, $\Psi \sim s^2 \Psi^3$. This gives the scaling law for amplitude of the vortex,

$$\Psi_m \sim \frac{1}{s} \quad \text{or} \quad \varphi_m \sim \frac{\sqrt{2}u^2 k}{S_1}. \quad (4.29)$$

On the other hand, multiplying both sides of Eq. (4.25) by $d\Psi/dt$ and integrating in time from $t = 0$ to $t = t_m$, we can approximately get

$$\Psi'(0) \approx (s^2/2)\Psi_m^4 - \Psi_m^2,$$

where $\Psi'(0) \equiv d\Psi(t=0)/dt$. Therefore the scaling law for the $\Psi'(0)$ is

$$\Psi'(0) \equiv \frac{d\Psi(t=0)}{dt} \sim \frac{1}{s} \quad \text{or} \quad \varphi'(0) \equiv \frac{d\varphi(x=0)}{dx} \sim \frac{\sqrt{2}u^2 k^2}{S_1}. \quad (4.30)$$

A detailed study of the numerical spectrum yields the $\Psi'(0)$ vs. s curve shown in Fig. 4.4. The curve shows the allowable initial momenta $\Psi'(0)$ for the eigenfunction $\Psi(t)$ that are bounded as $t \rightarrow \pm\infty$, versus the shear parameter s . The shaded regions in Fig. 4.4 represent the allowable initial values for $\Psi'(0)$. The lowest values of $\Psi'(0)$ gives the minimum flow velocity for the vortex core required for the formation of the coherent trapped structure. Both the Figs. 4.3 and 4.4 consistently support the scaling laws presented by Eqs. (4.29) and (4.30). In addition, Fig. 4.4 shows that the existence of a vortex for small electric fields $\Psi'(0)$ (or flow velocity) requires that $s \geq 0.06$, whereas for large electric fields a vortex is formed for $s \geq 0.02$.

From the analysis, we conclude that when the magnetic shear parameter $s \ll 0.02$, the effect of magnetic shear on drift waves is small and the coupling between the vorticity and parallel velocity fields is weak. The decoupled vorticity equation becomes the H-M equation and therefore we recover

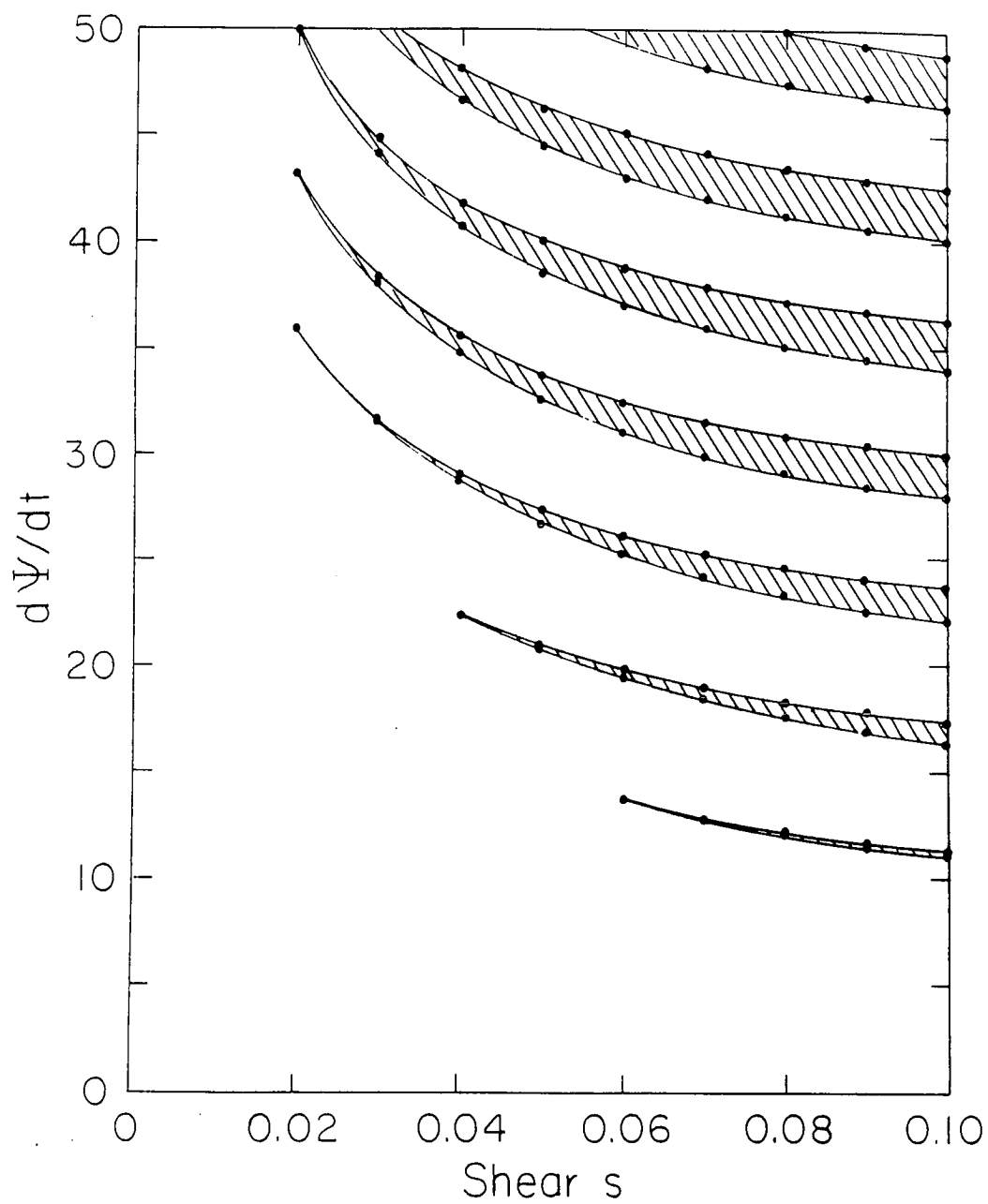


Figure 4.4: Spectrum of critical $d\Psi(t=0)/dt$ versus the effective shear s from 0 to 0.1.

The spectrum shows the allowable initial “momenta” $d\Psi(t=0)/dt$ in the range of 0 — 50 for the eigenfunction $\Psi(t)$ to be bounded as $t \rightarrow \pm\infty$. The shaded regions represent the allowable initial values for $d\Psi(t=0)/dt$.

the modon solutions. With the increase of s , the coupling between the two fields becomes important. When $0.02 \leq s \leq \sqrt{2}/2$, the new type of dipole vortex emerges. The new vortices are localized solitary waves. However, when $s > \sqrt{2}/2$, the strong coupling between the drift waves and ion acoustic waves causes strong radiation damping of energy from the vortex cores and thus eliminates the existence of the solitary waves.

Although the above analysis is based on the one-dimensional model, the main features given in the analysis have been shown to generally agree with those of 2-D numerical solutions obtained recently [Horton *et al.*, 1992 (a)]. Figure 4.5 is a comparison between the 1-D and 2-D numerical solutions for $s = 1$. It shows that the both solutions generally agree with each other, except that the amplitude of the 2-D solution is slightly larger than that of 1-D solution. Figure 4.6 is 3-D plot and contour plot of the 2-D numerical solution which clearly shows the new dipole vortex structure. The 2-D simulations of Eqs. (4.4) and (4.5) discussed in the following section show that the principle features of the one-dimensional model are consistent with the simulation. As the shear parameter increases the x -variation of the coherent structure becomes stronger than the y -variation and the one dimensional model becomes more accurate. The one-dimensional model is adequate qualitative picture, but does not yield quantitative values for the amplitudes.

4.4 Properties of the Coherent Structures in Sheared Magnetic Field

It is important to note that the dipole solutions presented in the last section are different from the Larichev and Reznik's modons [Larichev

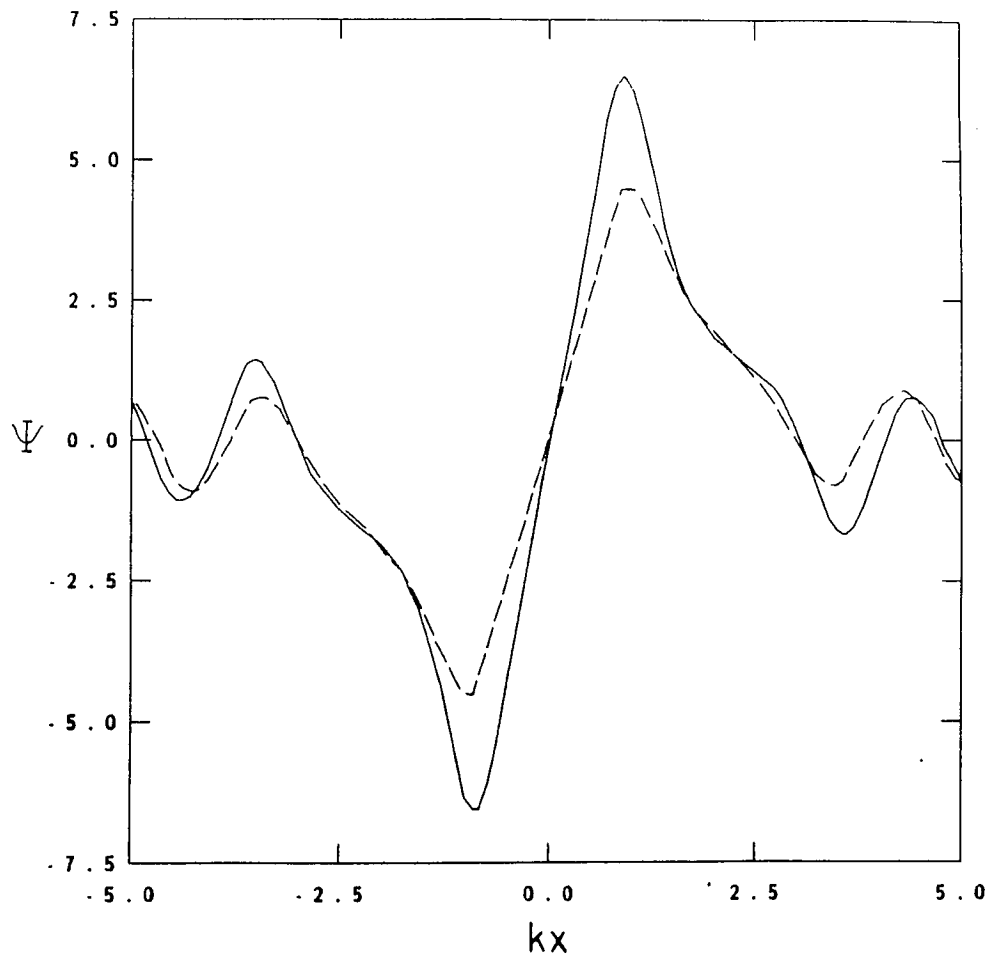


Figure 4.5: Comparison between the 1-D and 2-D numerical solutions with $s = 1$.

----- 1-D solution.
 ——— 2-D solution with $y = 0$.

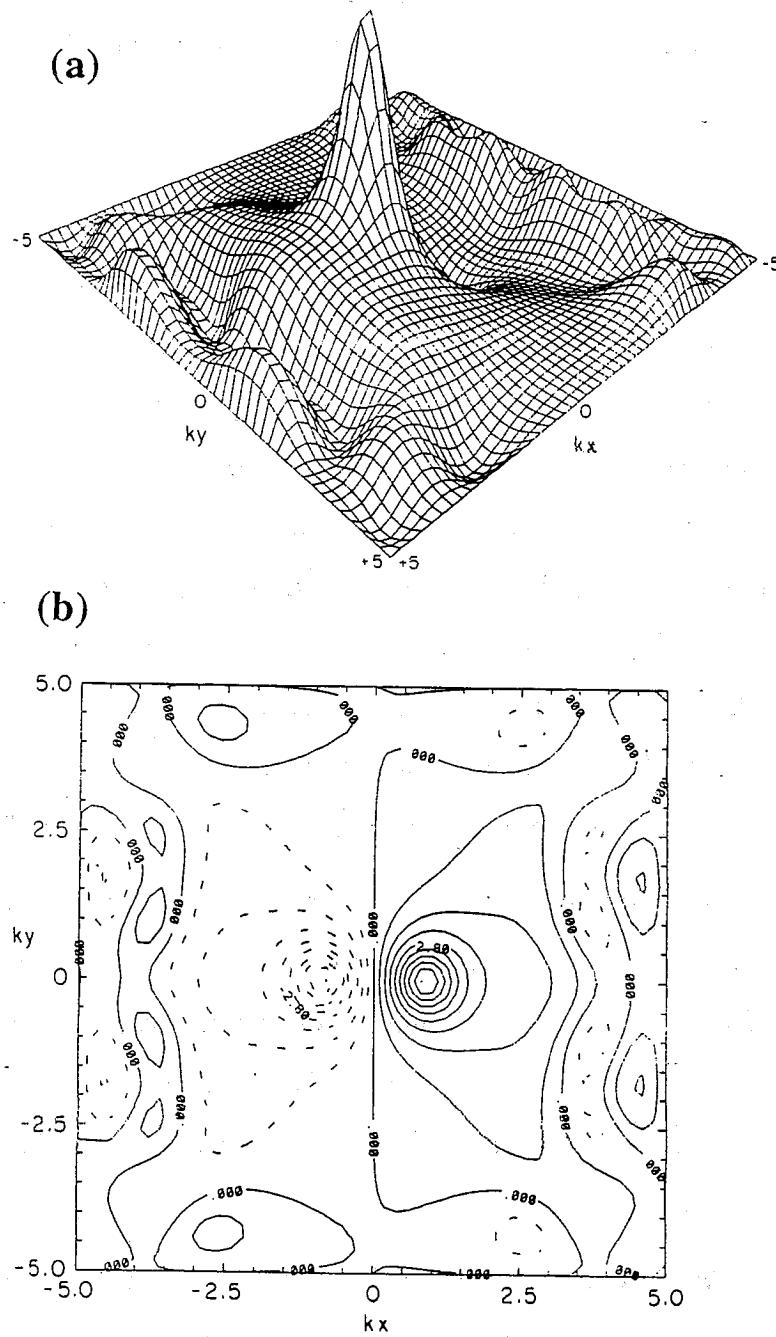


Figure 4.6: Drift wave - Ion acoustic wave vortex in a sheared magnetic field for $s = 1$.

(a) 3-D plot. (b) Contour plot.

and Reznik, 1976]. The modon construction uses two different linear functions $F(\varphi - ux)$ in the two different regions, namely, the interior and exterior regions of a modon; thus, the equations determining the modon structure are two linear equations. These two equations are solved separately in the two regions and the solutions from the two regions are matched up to second derivatives at the boundary. However, the construction of the new dipole solutions presented in the preceding section uses only one single arbitrary function $F(\varphi - ux)$. Therefore the derivatives of the eigenfunction $\varphi = (u/k)\Psi$ are continuous to any order in the whole x - y plane. Furthermore, the equation determining the structure of the dipole is a nonlinear multi-eigenvalue equation. When the parameters S_1 and u are given, one can find multiple eigenfunctions $\varphi_n(x)$ with different amplitudes and derivatives $d\varphi_n(x=0)/dx$. The derivatives $d\varphi_n(x=0)/dx$ of eigenfunctions form a banded continuous spectrum as a function of the parameter $s = S_1/\sqrt{2}(u - v_{d0})$ as shown in Fig. 4.4.

The new solitary waves, as pointed out in the last section, couple to the ion acoustic wave due to existence of magnetic shear. The coupling leads to the formation of the oscillating tail emanating from the core of vortex. This tail causes the dissipation of energy from the solitary wave core. However, when $s < \sqrt{2}/2$ or $S_1 < |u - v_d|$, the tail is small and the dissipation of energy is negligible.

We also find that when the new dipole vortex interacts with the drift sheared flow, one pole of the dipole will be destroyed and the other pole will survive and eventually evolve into a monopole. Which pole of the dipole will survive or vanish is determined by the sign of v'_{d0} or orientation of the drift sheared flow. Figure 4.9 presented in the next section is an example of the

interaction. The mechanism of the interaction is basically same as that of a modon in a sheared drift flow as studied in detail in Sec. 3.4.

In the previous section, we have pointed out that the formation of the new dipole structure in a sheared magnetic field requires an amplitude

$$\varphi_m \sim \frac{\sqrt{2}u^2 k}{S_1},$$

and the flow velocity

$$\varphi'(0) \equiv \frac{d\varphi(x=0)}{dx} \sim \frac{\sqrt{2}u^2 k^2}{S_1}.$$

Therefore the critical $\mathbf{E} \times \mathbf{B}$ Reynolds number R_E can be given by

$$R_E = \frac{\Omega_E(k)}{\omega_k} \sim \frac{d\varphi/dx}{v_d} \sim \frac{d\Psi}{dt} \sim \frac{1}{s}. \quad (4.31)$$

For a well-localized dipole structure with negligible radiation damping, it requires that $s < \sqrt{2}/2$. Therefore we conclude that the formation of the well-localized vortex structure requires that

$$R_E \sim \frac{d\varphi/dx}{v_d} \geq 1.4. \quad (4.32)$$

We know that the mixing length level is defined by

$$R_E \sim \frac{d\varphi/dx}{v_d} \sim 1.$$

Therefore the new dipole structures can be formed in a sheared magnetic field when the amplitudes of the flow velocity $d\varphi/dx$ or internal electric field are just above those of the mixing length level. Figures 4.7 and 4.8 in the next section show the cases for $R_E \gg 1.4$ and $R_E \ll 1$, respectively. In the both cases, we started with the same initial dipole vortex. when the time progresses, the

dipole vortex in Fig. 4.8 with $R_E \ll 1$ soon spreads out into the whole space due to the domination of linear dispersive propagation, while the dipole vortex in Fig. 4.7 with $R_E \gg 1.4$ keeps its shape for a long time without much change because of the domination of nonlinear self-binding.

From the analysis, we can sum up the properties of the vortex structures in sheared magnetic field as following: when the magnetic shear parameter $s \ll 0.02$, the effect of magnetic shear on drift waves is small and the coupling between the vorticity and parallel velocity fields is weak. In this case the decoupled vorticity equation becomes the H-M equation and therefore we recover the modon solutions. With the increase of s , the coupling between the two fields becomes important. When $0.02 \leq s \leq \sqrt{2}/2$ or the $\mathbf{E} \times \mathbf{B}$ Reynolds number $R_E \geq 1.4$, the new type of dipole vortex emerges. The new dipole vortices are localized solitary waves. But when the dipole vortex interacts with sheared flow, it will involve into monopole vortex. For strong magnetic shear $s > \sqrt{2}/2$, the strong coupling between the drift waves and ion acoustic waves causes strong radiation damping of energy from the vortex cores and thus eliminates the existence of the solitary waves.

4.5 Numerical Simulation Results

In order to facilitate the numerical solutions of Eqs. (4.4) and (4.5), we first expand Eq. (4.4) according to the ordering in Eq. (4.7) and consider $v'_{d0} \sim \kappa_T \sim \epsilon_n \sim \epsilon$. Keeping only the terms of order ϵ and ϵ^2 , we derive from Eqs. (4.4) and (4.5) the reduced dynamical equations

$$\left(\frac{1}{T(x)} - \nabla^2 \right) \frac{\partial \varphi}{\partial t} + (v_{d0} + v'_{d0}x - \kappa_T \varphi) \frac{\partial \varphi}{\partial y} - [\varphi, \nabla^2 \varphi] = -S(x) \frac{\partial v_{\parallel}}{\partial y}, \quad (4.33)$$

$$\frac{\partial v_{\parallel}}{\partial t} + [\varphi, v_{\parallel}] = -S(x) \frac{\partial \varphi}{\partial y} + \mu \nabla^2 v_{\parallel}. \quad (4.34)$$

Here $v'_{d0} = \rho_{s0} dv_d/dx \sim (\rho_{s0}/r_n) v_{d0}$ at the core of the vortex. In writing Eq. (4.34) we have included a viscous damping term to absorb energy transferred to $|k| \rightarrow \infty$.

To solve Eqs. (4.33) and (4.34), we use a uniform grid over x and k_y in 85×85 xk_y -space with 3655 complex $\varphi_{x,k_y}(t)$ and $v_{\parallel x,k_y}(t)$ modes. Since the first term of Eq. (4.33) depends on x , we leave the equation in x space and use the second order central difference formula for ∂_x^2 , which yields a tri-diagonal system that is solved for each $\partial_t \varphi(x, k_y, t)$. We use the Ahlberg-Nilson-Walsh algorithm for cyclic tri-diagonal systems [Temperton, 1975] to reduce the operator $(1/T(x) - \nabla^2)$ to a cyclic tri-diagonal matrix. Upon inverting the matrix we obtain $\partial_t \varphi(x, k_y, t)$ for each mode. The nonlinear convolution terms in both the equations are evaluated by first transforming φ and v_{\parallel} in $k_x k_y$ space to get derivatives of φ and v_{\parallel} , then transforming $\varphi_{\mathbf{k}}$ and $v_{\parallel \mathbf{k}}$ and their derivatives into xy -space to calculate the convolutions. The results are then transformed back into xk_y -space. Finally we use the fifth and sixth order Runge-Kutta time stepping to get $\varphi(x, k_y, t)$ for each mode at each time step. The constants of motion defined in Eqs. (4.9)–(4.12) are used to monitor the accuracy of the code. The modon of Larichev and Reznik is taken as the initial perturbation for $\varphi(x, y, t = 0)$, and Eq. (4.17) with $v_{\infty} = 0$, for v_{\parallel} . The exponential temperature profile $T(x) = \exp(-c_2 x)$ is used so as to avoid the negative temperature problem that can arise when expanding $T(x)$ as $1 - c_2 x$. For the exponential profile $\kappa_T = -(1/T^2) dT/dx = c_2 \exp(c_2 x)$. Because of periodic boundary condition, we choose the magnetic shear profile as $S(x) = S_m \sin(2\pi x/L_x)$, where $L_x = 20\pi\rho_{s0}$ is the length of periodic simulation box in

the x -direction. Typical simulations use an average of 40 minutes CPU time on the CRAY-2 for $\Delta t = 100 r_n/c_s$ which is about 10 rotations of the vortex core.

In the first case we used $v'_{d0} = c_2 = 0$, $\mu = 0.1$ and $S_m = 0.1$ so that $S_1 \simeq 0.01$ and the effective shear $s \simeq 0.07$, which give the parameter $|u/v_d - 1| = 0.1 \gg S_1$, therefore the radiative damping of the vortex is small and negligible. We start with Larichev and Reznik's modon with $u = 1.1v_{d0}$ and $r_0 = 6.0\rho_{s0}$, so that the center derivative of the modon $\varphi'(0) \equiv (\partial\varphi/\partial x)_{x=0} \simeq 6.7$ or $\Psi'(0) \simeq 6.1$ where $t = kx$. In this case, the $\mathbf{E} \times \mathbf{B}$ Reynolds number $R_E = \Omega_E/\omega_k \sim 7$. We observe that the dipole vortex structure for the φ field stays a long time without much change, and that the v_{\parallel} field, though experiencing some change, still keeps a rather coherent and stable structure in the interior region of the dipole vortex. After a long time, the amplitude of the dipole $\varphi_m \sim 13$, the velocity $u \sim 1.3$, and the center derivative $\varphi'(0)$ slightly increases. Figure 4.7 shows the streamline of $\varphi(x, y, t) = \text{const.}$ and $v_{\parallel}(x, y, t) = \text{const.}$ at times $tc_s/r_n = tv_{d0}/\rho_{s0} = 0, 20, 40$ and 60 .

In the second case, we use same parameters as those in the first case. The initial dipole vortex is also same as that in the first case, but with much small amplitude, so that $R_E \ll 1$. Figure 4.8 shows that the dipole vortex spreads out very soon into the whole space with the progress of time.

In the third case, we show the interaction between the new dipole vortex presented in Sec. 4.3 and sheared drift flow. We choose $c_2 = 0$, $v'_{d0} = 0.05$, $S_m = 0.1$ ($S_1 \simeq 0.01$ and $s \simeq 0.07$), $u \simeq 1.1v_{d0}$ and $\mu = 0.1$. The same initial profiles as those in the first case are used for φ and v_{\parallel} . As time progresses, the positive pole of the dipole is destroyed and the negative pole

survives and gradually involves into a monopole vortex. The results are shown in Fig. 4.9.

Finally, we test the radiation damping of the dipole vortex due to the strong coupling of the vortex with ion acoustic wave when $s \sim 1$ or $|u/v_d - 1| \sim S_1$. We set $|u/v_d - 1| \sim S_1 = 0.1$, $c_2 = 0$ and $v'_{d0} = 0$. In this case $R_E \sim 3$. The results in Fig. 4.10 show that the dipoles eventually connect to oscillating tails with significantly large amplitudes and the dipole vortices experience strong damping of energy through the tails.

In all the simulations, we notice that the waves with small amplitudes in the $v_{||}$ field appear to be stationary and that the energy of the $v_{||}$ field tends to go into waves with small scale lengths. The reason for these phenomena is that Eq. (4.34) does not have a linear wave term like $v_{d0} \partial \varphi / \partial y$ as in Eq. (4.33); thus linear waves with small amplitude do not propagate. Since Eq. (4.34) lacks linear dispersion, the nonlinear steeping process cannot be effectively balanced and the waves with small scale lengths tend to grow. Because of this fact, we add a viscous term in Eq. (4.34) to dissipate the energy transferred to the waves with the smallest scale lengths resolved in the system.

The results of the simulations show the general consistency with the results of the analysis in the previous section. In particular, the simulations show that the dipole-type vortex solutions of the drift wave-ion acoustic wave system can exist in a sheared magnetic field when the electron temperature is constant over the vortex. The dipole type vortices are well formed and can last a long time without much damping if $s < 1$ or $|u/v_d - 1| > S_1$ provided the $\kappa_T \rightarrow 0$. For finite κ_T we can estimate [Su *et al.*, 1988] the life time of the dipole vortex from $t_L \sim 1/\kappa_T \varphi_m k \sim 1/\kappa_T \varphi'(0) k^2$.

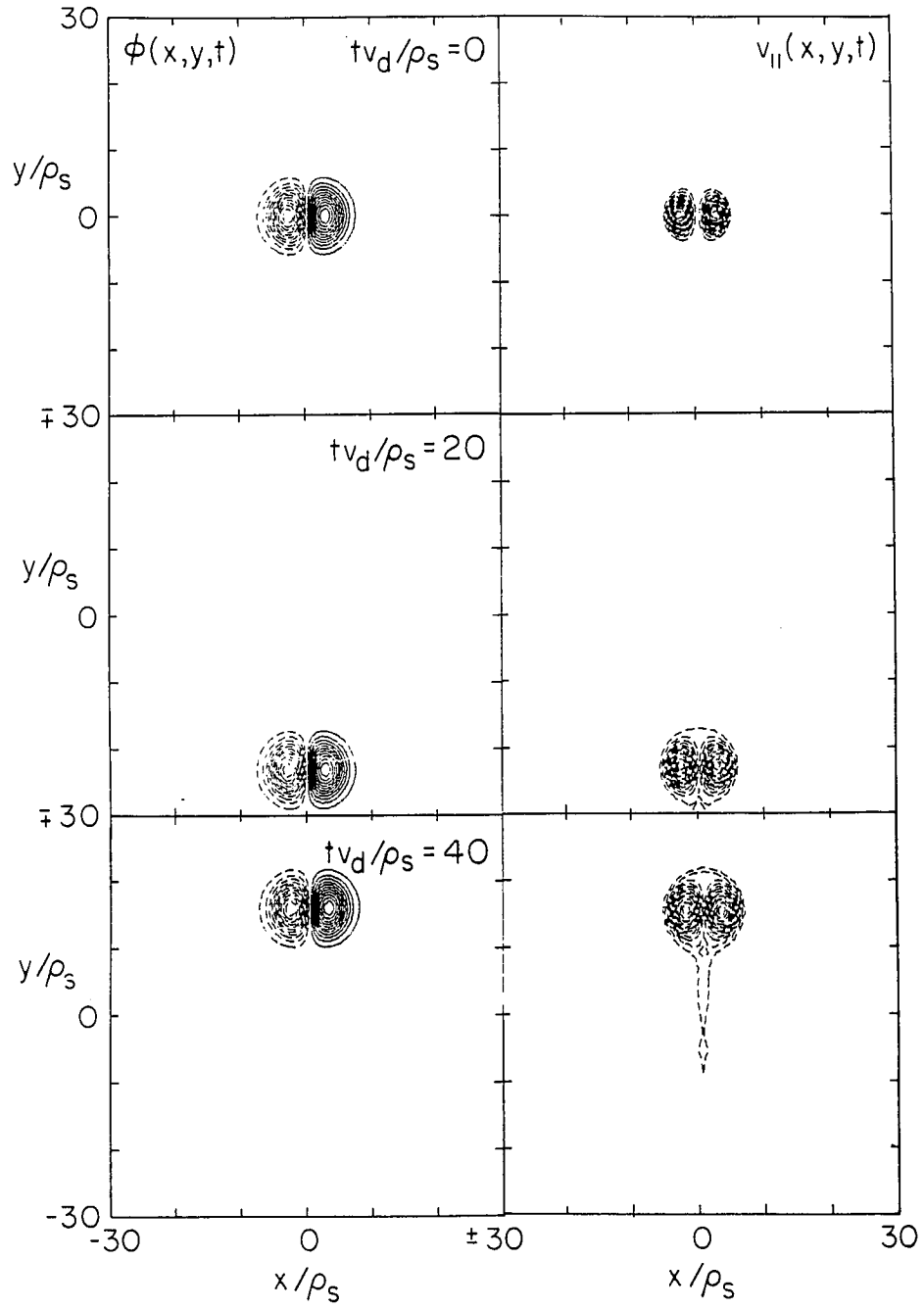


Figure 4.7: Contour plots of the electrostatic potential $\phi(x, y, t)$ and parallel velocity $v_{||}(x, y, t)$ with magnetic shear parameter $S_m = 0.1 (s \simeq 0.07)$, drift velocity gradient $v'_{d0} = 0$ and $R_E \sim 7$.

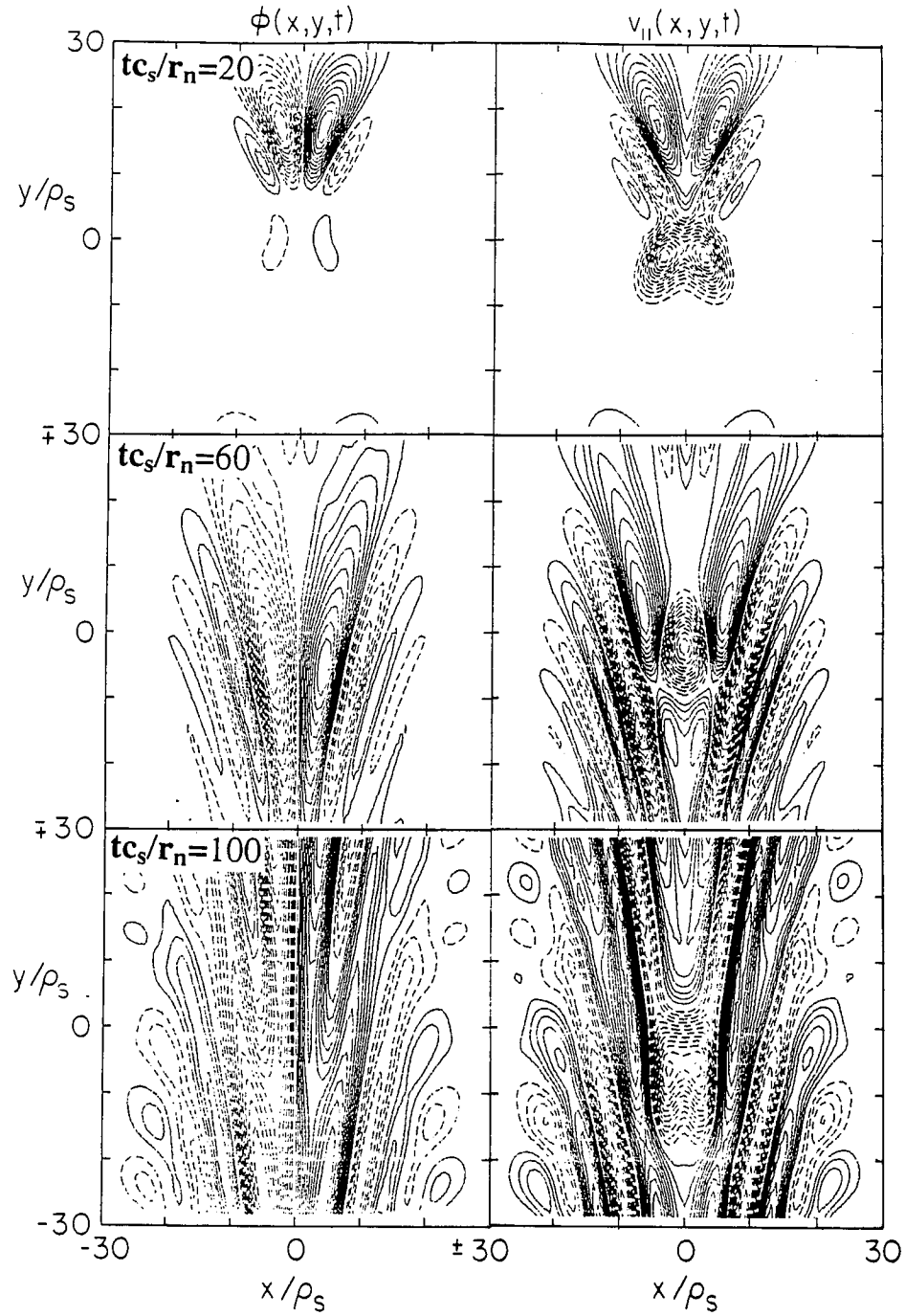


Figure 4.8: Contour plots of the electrostatic potential $\phi(x, y, t)$ and parallel velocity $v_{||}(x, y, t)$ with the parameters same as in Fig. 4.7, but $R_E \ll 1$.

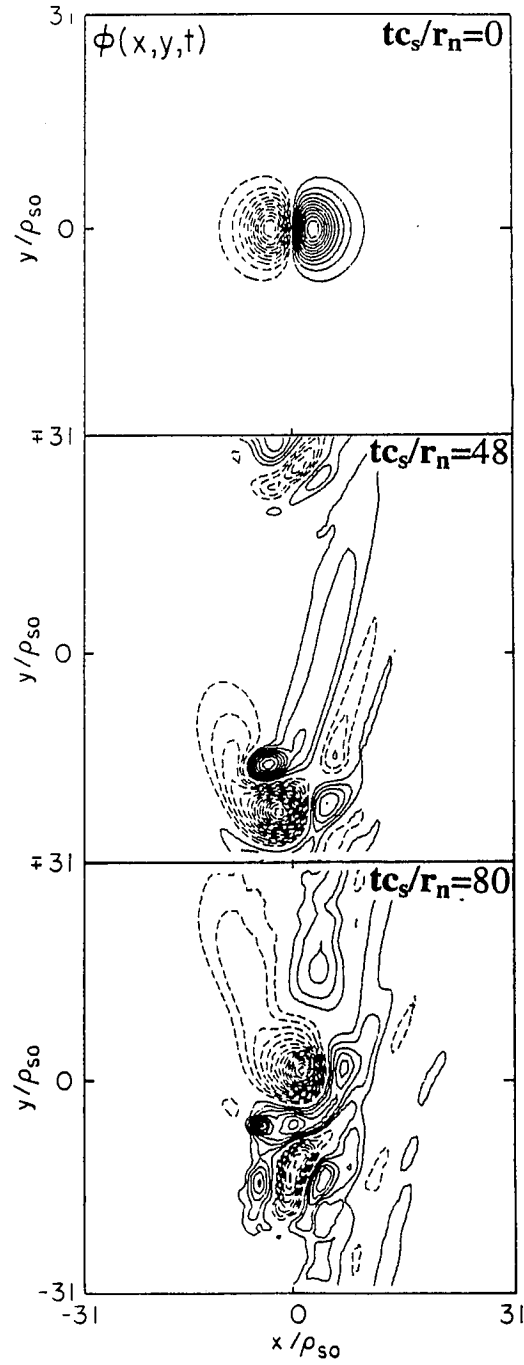


Figure 4.9: Interaction of the new dipole vortex presented in Sec. 4.3 with drift sheared flow.

Strong Magnetic Shear $r_n/L_s = 0.1$

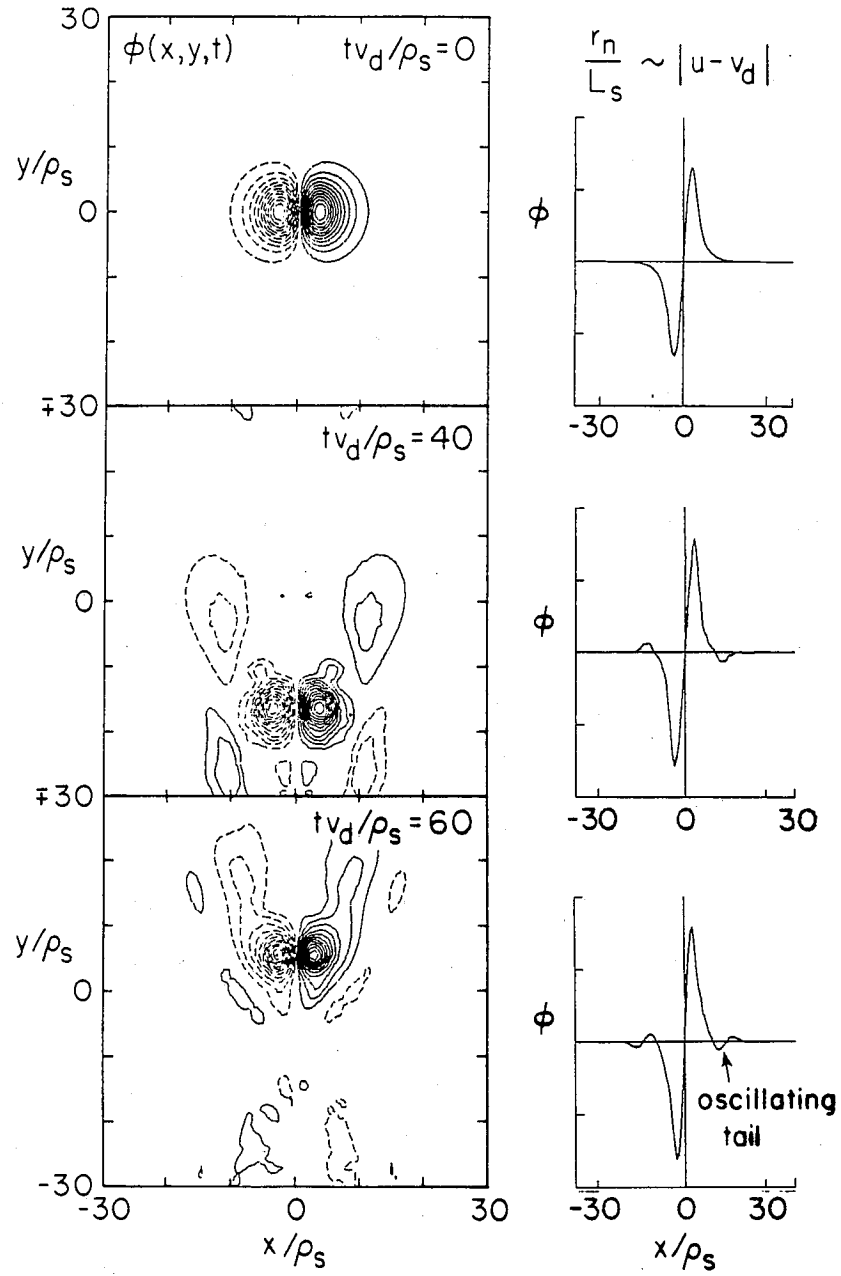


Figure 4.10: Radiation damping of the new vortex structure when $s \sim 1$ or $|u/v_d - 1| \sim S_1$.

4.6 Conclusion

Analytical and numerical studies of the effect of magnetic shear on drift wave vortices in inhomogeneous plasmas have been reported. Analytically we have derived a solitary vortex equation that includes the effects of density and temperature gradients and magnetic shear, and we have used a quasi-one-dimensional model to exhibit the main features of solitary vortices in sheared magnetic fields. The analysis shows that in a plasma with constant temperature and drift velocity, the presence of a small magnetic shear will cause the effective potential to change from a non-trapping to a trapping potential, which indicates the possible formation of solitary vortex structures with finite amplitudes. The solutions are shown to have the dipole-type symmetry. However, they are different from the well-known modon vortices, because the derivatives of their eigenfunctions are continuous to any order in the whole plane, also, the value of the center derivative $\varphi'(0)$ (measuring the internal flow velocity) and the vortex amplitudes form a banded continuous spectrum.

It is also shown that the presence of the magnetic shear intrinsically causes the solitary drift waves to couple to the ion acoustic waves. Thus the dipole solutions are not monotonically decreasing functions, instead, they have oscillating tails with monotonically decreasing amplitudes connecting to the core of vortices. This behavior is similar to the monopoles induced by the gradient of drift velocity in shearless magnetic fields studied in Chapter 3. The oscillating tails cause radiative damping of vortex energy. The damping is negligible if the amplitude $\varphi_m (\sim \sqrt{2}u^2k/S_1)$ of the dipole structure satisfies $\varphi_m > \sqrt{2}u/k$ given by $s < \sqrt{2}/2$ or $S_1 < uk^2$. For a weak effect of magnetic shear, this condition is consistent with that for the Larichev-Reznik's modon.

However, for shear above a small threshold value $s > s_c \approx 0.02$ as given in Fig. 4.4, we find that the nonlinearity of the v_{\parallel} induced by the shear and vorticity equations combine to produce a nonlinear restoring force proportional to $(S_1^2/2u^4)\varphi^3$ which gives the new dipole vortex structures when $s > 0.02$ or $S_1 > 0.03|u/v_d - 1|$. The nonlinear structures in the weakly sheared field greatly reduce the shear radiation expected in the linear drift wave-ion acoustic wave theory.

The numerical simulations performed in 2-D with the coupled vorticity and parallel mass flow equations consistently support the analysis. The simulations show that for a plasma with constant temperature and drift velocity in a magnetic field with small shear, the well-formed dipole vortices are stable and can last a long time without much damping when $|(u/v_d) - 1| > S_1$. However with the presence of a small temperature gradient, the dipole vortices become structurally unstable and are rapidly separated into monopole vortices, which is consistent with the results in previous chapters on the effect of finite inhomogeneities across the core of the vortex. Therefore we conclude that with constant temperature and drift velocity, the coherent structures of drift wave plasmas behave like dipole vortices in either shearless or sheared magnetic fields. But when the gradients of temperature and drift velocity exist, the solitary coherent structures take the form of monopole vortex structures rather than dipole structures.

Chapter 5

Formation of Drift Wave Vortices in Parallel Shear Flow Driven Turbulence

5.1 Introduction

In the previous chapters, we have studied the solitary coherent vortex structures of nonlinear drift waves in an inhomogeneous plasma background and in a sheared magnetic field. The physical systems considered in the previous chapters are conservative. In nature, however, a physical system is always associated with damping and/or driving forces. The solitary wave with finite dissipation will dissipate away in a relaxation process if there is no energy source. Thus studies of evolution of the coherent vortex structures in an unstable system is essential to understand the drift wave vortices and turbulence in nature.

During the past decades there have been comprehensive studies of the nonlinear dynamics of drift waves by various groups with different approaches. From these studies, many properties of drift wave turbulence have been obtained; for example: nonlinear saturation in an unstable system is initiated by the $\mathbf{E} \times \mathbf{B}$ drift [Horton, 1976], the frequency spectrum has a broad frequency component [Meiss and Horton, 1982; Terry and Horton, 1983], the wavenumber spectrum evolution is characterized by an inverse cascade [Hasegawa and Wakatani, 1983], the wavenumber spectrum obeys the Kolmogorov-Kraichnan power law k^{-3} [Kraichnan, 1967; Wakatani and Hasegawa, 1984], etc..

On the other hand, as pointed out in Chapter 1, there exist many nonlinear drift wave models, which describe plasma dynamics in various regimes and plasma geometries, that possess solitary vortex solutions. Thus it is expected that the nonlinear drift wave equations link strong turbulent motions to self-organized motions. The transition process from the turbulent state to the coherent structure has the following feature: the energy of the turbulent flow characterized by incoherent motion of many small scale vortices experiences the inverse cascade which appears as coalescing and pairing of the small scale vortices into large scale vortices. It has been shown by rotating water tank experiments [Sommeria *et al.*, 1988] and numerical simulations [Overman and Zabusky, 1982; Horton, 1989; Marcus, 1990; Tajima *et al.*, 1991] that the coalescence takes place when two vortices with like-signed vorticities interact, and the pairing is likely to happen when two vortices with opposite-signed vorticities and certain polarity are within a short distance from each other [Couder and Basdevant, 1986; Horton, 1989]. Thus it is anticipated that the continuous processes of coalescing and pairing may cause the formation of a single large scale coherent structure. Recently there have been different approaches proposed by several authors to explain the self-organization process [Hasegawa, 1985; Kadomtsev, 1987; Tsytovich and Shukla, 1991; Muhm *et al.*, 1991 and 1992].

In this chapter, as a paradigm of unstable drift wave system, we study the formation of coherent vortex structures in parallel shear flow driven turbulence. Analytically, we derive a model which incorporate the instability, and demonstrate the existence of a electrostatic dipole vortex solution in such a system. Numerically, we study the formation of the coherent vortex structure

via turbulence in the course of nonlinear development of the instability, that is, the so-called self-organization process.

The organization of this chapter as follows. In Sec. 5.2, we derive the nonlinear drift wave model equation with parallel shear flow driven instability, and then analyze the linear instability. The nonlinear solitary vortex solutions of the model are given in Sec. 5.3. In Sec. 5.4 we present the numerical simulation to show the evolution of the linear and nonlinear waves. Section 5.5 is devoted to summary and discussion.

5.2 Dynamical Equations and Analysis of Linear Instability

To derive the nonlinear evolution equation, we consider a physical system which is basically the same as that considered in Sec. 4.2 of Chapter 4, except now the mean ion flow velocity is no longer zero or a constant; instead we consider the velocity is a function of spatial variable x . Following the same procedure as that described in Sec. 4.2 of the preceding chapter, we are able to derive the system of the equations,

$$\begin{aligned} (1 - \nabla_{\perp}^2) \frac{\partial \delta \varphi}{\partial t} + v_d \frac{\partial \delta \varphi}{\partial y} + v_{0y}(x) (1 - \nabla_{\perp}^2) \frac{\partial \delta \varphi}{\partial y} - [\delta \varphi, \nabla_{\perp}^2 \delta \varphi] \\ = -\nabla_{\parallel} \delta v_{\parallel} - \mu_{\perp} \nabla_{\perp}^4 \delta \varphi, \end{aligned} \quad (5.1)$$

$$\frac{\partial \delta v_{\parallel}}{\partial t} + v_{0y}(x) \frac{\partial \delta v_{\parallel}}{\partial y} - \frac{\partial v_{0\parallel}}{\partial x} \frac{\delta \varphi}{\partial y} + [\delta \varphi, \delta v_{\parallel}] = -\nabla_{\parallel} \delta \varphi + \nu_{\perp} \nabla_{\perp}^2 \delta v_{\parallel}, \quad (5.2)$$

where

$$\nabla_{\perp} = \hat{\mathbf{x}} \frac{\partial}{\partial x} + \hat{\mathbf{y}} \frac{\partial}{\partial y},$$

$$\nabla_{\parallel} = \frac{\partial}{\partial z} + S(x)\partial/\partial y ,$$

$$[f , g] = \frac{\partial f}{\partial x} \frac{\partial g}{\partial y} - \frac{\partial f}{\partial y} \frac{\partial g}{\partial x} ,$$

μ_{\perp} and ν_{\perp} are dissipation coefficients.

The non-dimensional variables are

$$x , y = x/\rho_s , y/\rho_s ;$$

$$z = z/r_n ;$$

$$t = c_s t/r_n ;$$

$$v_{\parallel} = (r_n/\rho_s)(v_{\parallel}/c_s) ;$$

$$\varphi = (r_n/\rho_s)(e\Phi/T_e) .$$

For fluctuations localized on a rational surface at $x = x_0$, the mean ion flow velocity \mathbf{v}_{i0} may be expanded around the rational surface as

$$\mathbf{v}_{i0}(x) = \mathbf{v}_{i0}(x_0) + (x - x_0) \frac{\partial \mathbf{v}_{i0}(x = x_0)}{\partial x} + \dots$$

Now we keep only the first derivative term and assume

$$\mathbf{v}_{i0}(x_0) = 0 ,$$

$$\frac{\partial \mathbf{v}_{0\perp}(x = x_0)}{\partial x} = 0 ,$$

$$\frac{\partial v_{0\parallel}(x = x_0)}{\partial x} = v'_{0\parallel} = \text{const.} ,$$

that is, there exists sheared flow only in parallel mean ion motions. To further simplify the model, we consider the 2-D case, that is, the case of single rational surface.

With these considerations, Eqs. (5.1) and (5.2) become

$$(1 - \nabla^2) \frac{\partial \delta \varphi}{\partial t} + v_d \frac{\partial \delta \varphi}{\partial y} - [\delta \varphi, \nabla^2 \delta \varphi] = -\nabla_{\parallel} \delta v_{\parallel} - \mu_{\perp} \nabla^4 \delta \varphi, \quad (5.3)$$

$$\frac{\partial \delta v_{\parallel}}{\partial t} - v'_{0\parallel} \frac{\partial \delta \varphi}{\partial y} + [\delta \varphi, \delta v_{\parallel}] = -\nabla_{\parallel} \delta \varphi + \nu_{\perp} \nabla^2 \delta v_{\parallel}, \quad (5.4)$$

where $\nabla_{\parallel} = S(x) \partial / \partial y$ and $\nabla^2 = \nabla_{\perp}^2 = \partial^2 / \partial x^2 + \partial^2 / \partial y^2$.

The fluctuation energy balance equation associated with the set of Eqs. (5.3) and (5.4) is given by

$$\begin{aligned} \frac{\partial \mathcal{E}}{\partial t} + \nabla \cdot \left[\frac{v_d}{2} \delta \varphi^2 \hat{\mathbf{y}} - \delta \varphi \nabla \frac{\partial \delta \varphi}{\partial t} - \nabla^2 \delta \varphi (\hat{\mathbf{z}} \times \nabla \frac{\delta \varphi^2}{2}) + (\delta \varphi \delta v_{\parallel}) \hat{\mathbf{b}} \right] \\ = v'_{0\parallel} \delta v_{\parallel} \frac{\delta \varphi}{\partial y} - \mu_{\perp} |\nabla^2 \delta \varphi|^2 - \nu_{\perp} |\nabla \delta v_{\parallel}|^2, \end{aligned} \quad (5.5)$$

where the fluctuation energy density \mathcal{E} is defined as

$$\mathcal{E}(x, y, t) = \frac{1}{2} \left[\delta \varphi^2 + (\nabla \delta \varphi)^2 + \delta v_{\parallel}^2 \right],$$

and $\hat{\mathbf{b}} = \hat{\mathbf{z}} + S(x) \hat{\mathbf{y}}$ is unit vector of magnetic field as defined in Sec. 4.2.

In Eq. (5.5), the term in the square bracket on the left hand side (l.h.s.) is the energy flux, the term $v'_{0\parallel} \delta v_{\parallel} \delta \varphi / \partial y$ on the right hand side (r.h.s.) is the energy source of the system and the second and third terms on r.h.s. are sinks or energy dissipations.

In studying the linear stability of Eqs. (5.3) and (5.4), we only discuss the local linear stability theory in which k_{\parallel} is a constant. For the nonlocal case where k_{\parallel} is a function of x , one needs to solve the eigenvalue problem, which is detailed in Hamaguchi and Horton [1992] and is not considered here.

In the local approximation, we replace ∇_{\perp} and ∇_{\parallel} by constants $ik_x \hat{\mathbf{x}} + ik_y \hat{\mathbf{y}}$ and $ik_{\parallel} = iS_0 k_y$, respectively, where $S_0 = (r_n / L_s)(\lambda_x) / \rho_s$ and λ_x is a

typical wave length in the x direction. Then the dispersion relation of a linear wave is obtained from Eqs. (5.3) and (5.4),

$$\omega = \frac{B(k) \pm \sqrt{B(k)^2 - 4(1 + k^2) \left[k_y^2 S_0 (v'_{0\parallel} - S_0) - i\sigma v_d k_y k^2 - \sigma^2 k^6 \right]}}{2(1 + k^2)}, \quad (5.6)$$

where

$$B(k) = v_d k_y - i\sigma k^2(1 + 2k^2), \quad (5.7)$$

and it is assumed that $\sigma = \mu_{\perp} = \nu_{\perp}$ for simplicity.

The linear instability growth rate is obtained by taking the imaginary part of ω , $\gamma(k) = \text{Im}(\omega)$. In Fig. 5.1, the growth rate $\gamma(k)$ is plotted as a function of k_y for various values of k_x at $\sigma = 0.01$, $S_0 = 0.2$ and $v'_{0\parallel} = 0.7$. Figure 5.1 also shows that the wavenumber spectral structure of the growth rate is characterized by the finite bandwidth for the instability. Figure 5.2 shows the stable and unstable regions in S_0 - $v'_{0\parallel}$ space for $k_x = 0$, $k_y = 2.6$ which is the most unstable mode in Fig. 5.1.

Without using the local approximation, the spectra of growth rate obtained both by solving eigenvalue problem [Hamaguchi and Horton, 1992] and by kinetic analysis of linear instability [Horton *et al.*, 1992 (b)] are shown to have similar structures as that shown in Fig. 5.1.

5.3 Solitary Vortex Solutions

In this section we look for the stationary solutions of Eqs. (5.3) and (5.4) traveling with velocity u in the y direction,

$$\begin{aligned} \delta\varphi(x, y, t) &= \delta\varphi(x, y - ut), \\ \delta v_{\parallel}(x, y, t) &= \delta v_{\parallel}(x, y - ut). \end{aligned} \quad (5.8)$$

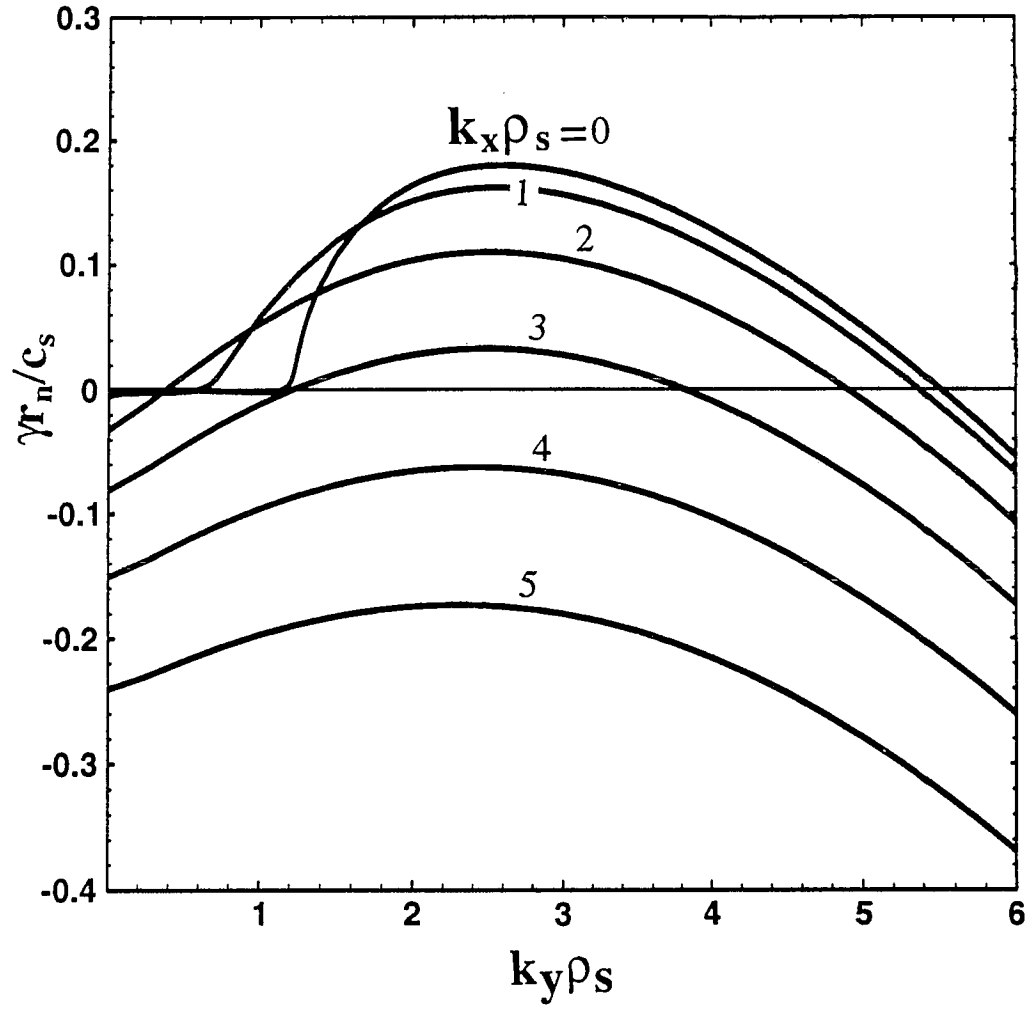


Figure 5.1: The growth rates $\gamma(k)(r_n/c_s)$ versus $k_y \rho_s$ for given $k_x \rho_s = 0-5$ in the case of $v'_{0\parallel} = 0, 7$, $S_0 = 0.2$ and $\sigma = 0.01$.

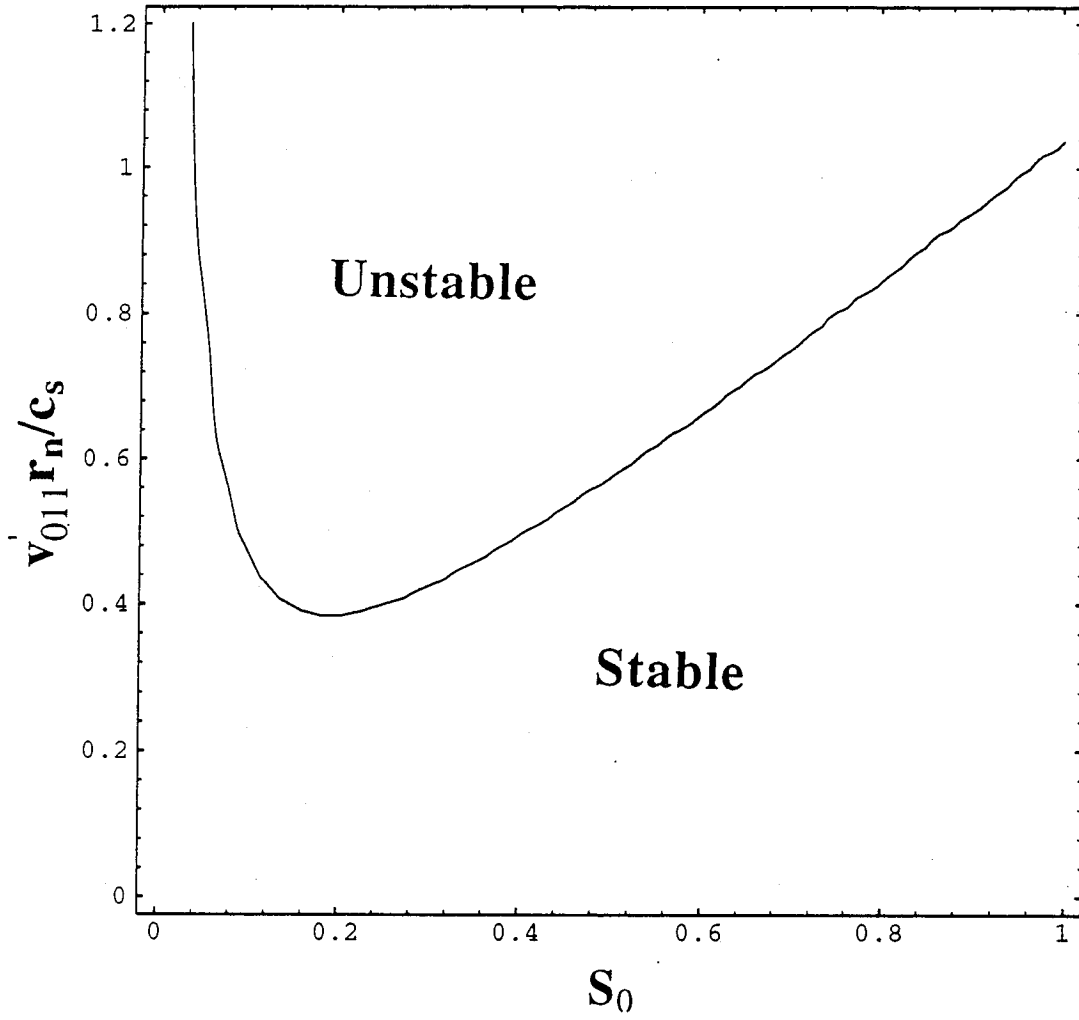


Figure 5.2: The stable and unstable regions in S_0 - $v'_{0||}$ space for the mode $k_x \rho_s = 0$, $k_y \rho_s = 2.6$ with $\sigma = 0.01$.

For simplicity, we use the local approximation and consider the dissipation to be small for large scale vortices, so that we replace ∇_{\parallel} with $S_0 \partial/\partial y$ where $S_0 = \text{const.}$ and set $\mu_{\perp} = \nu_{\perp} = 0$ in Eqs. (5.3) and (5.4). Upon inserting Eq. (5.8) into Eqs. (5.3) and (5.4), we can write the steady state equations as:

$$-u(1 - \nabla^2) \frac{\partial \delta \varphi}{\partial y} + v_d \frac{\delta \varphi}{\partial y} - [\delta \varphi, \nabla^2 \delta \varphi] = -S_0 \frac{\partial \delta v_{\parallel}}{\partial y}, \quad (5.9)$$

$$-u \frac{\partial \delta v_{\parallel}}{\partial y} - v'_{0\parallel} \frac{\partial \delta \varphi}{\partial y} + [\delta \varphi, \delta v_{\parallel}] = -S_0 \frac{\partial \delta \varphi}{\partial y}. \quad (5.10)$$

Equations (5.9) and (5.10) have dipole vortex solutions which are defined in two regions of x-y plane.

$$\text{Interior region: } x^2 + y^2 = r^2 < r_0^2,$$

$$\text{Exterior region: } x^2 + y^2 = r^2 > r_0^2,$$

where r_0 is a constant parameter characterizing the size of the vortex. The solutions must satisfy the following boundary conditions.

- (1) In the interior region, $\delta \varphi$ and δv_{\parallel} must be finite at $r = 0$,
- (2) In the exterior region, $\delta \varphi$ and $\delta v_{\parallel} \rightarrow 0$ as $r \rightarrow \infty$,
- (3) On the border between interior and exterior regions, where $r = r_0$, $\delta \varphi$, $\partial_r \delta \varphi$, $\nabla^2 \delta \varphi$ and δv_{\parallel} must be continuous.

The simplest solutions to satisfy the conditions are given as follows.

In the interior region ($r < r_0$):

$$\nabla^2 \delta \varphi = -p^2 \delta \varphi + a_1 x, \quad (5.11)$$

$$\delta v_{\parallel} = d \delta \varphi + a_2 x. \quad (5.12)$$

Substituting Eqs. (5.11) and (5.12) into Eqs. (5.9) and (5.10) yields

$$a_1 = u(1 + p^2) - v_d - S_0 d , \quad (5.13)$$

$$a_2 = S_0 - v'_{0\parallel} - u d . \quad (5.14)$$

In the exterior region ($r > r_0$):

$$\nabla^2 \delta\varphi = k^2 \delta\varphi , \quad (5.15)$$

$$\delta v_{\parallel} = b \delta\varphi , \quad (5.16)$$

where Eqs. (5.9) and (5.10) together with Eqs. (5.15) and (5.16) determine

$$b = \frac{S_0 - v'_{0\parallel}}{u} , \quad (5.17)$$

$$k^2 = 1 - \frac{v_d}{u} - \frac{S_0(S_0 - v'_{0\parallel})}{u^2} . \quad (5.18)$$

We remind that $v'_{0\parallel} > S_0$ is sufficient condition for instability according to Eq. (5.6).

Solving Eqs. (5.11) and (5.15), we get the solutions for $\delta\varphi$

$$\delta\varphi = \begin{cases} \left[-\frac{k^2 r_0}{p^2 r} \frac{J_1(pr)}{J_1(pr_0)} + \left(1 + \frac{k^2}{p^2} \right) \right] u r \cos \theta & (r < r_0) , \\ \frac{K_1(kr)}{K_1(kr_0)} u r_0 \cos \theta & (r > r_0) . \end{cases} \quad (5.19)$$

Imposing the matching condition (3), we obtain

$$d = \frac{u - v_d - u k^2}{S_0} = \frac{S_0 - v'_{0\parallel}}{u} = b , \quad (5.20)$$

$$a_2 = 0 , \quad (5.21)$$

and parameters p and k are related by

$$\frac{1}{kr_0} \frac{K_2(kr_0)}{K_1(kr_0)} = -\frac{1}{pr_0} \frac{J_2(pr_0)}{J_1(pr_0)} , \quad (5.22)$$

where J and K are Bessel and McDonald functions, respectively.

Equations (5.12) and (5.16) together with Eqs. (5.20) and (5.21) give solutions for δv_{\parallel} ,

$$\delta v_{\parallel} = \begin{cases} (S_0 - v'_{0\parallel}) \left[-\frac{k^2 r_0}{p^2 r} \frac{J_1(pr)}{J_1(pr_0)} + \left(1 + \frac{k^2}{p^2} \right) \right] r \cos \theta & (r < r_0) , \\ (S_0 - v'_{0\parallel}) \frac{K_1(kr)}{K_1(kr_0)} r_0 \cos \theta & (r > r_0) . \end{cases} \quad (5.23)$$

Equations (5.19) and (5.23) show that both $\delta\varphi$ and δv_{\parallel} have dipole vortex solutions with core size r_0 and constant speed u moving in the y direction. Figure 5.3(a) and (b) show 3-D plots and their contour plots of the dipole vortices for $\delta\varphi(x, y)$ and δv_{\parallel} , respectively.

For the vortex solutions to be localized or isolated, it requires that the speed u of the vortices to be within the bounds determined by $k^2(u) > 0$, where $k^2(u)$ is defined in Eq. (5.18) and is called as nonlinear dispersion relation, i.e.,

$$k^2(u) = 1 - \frac{v_d}{u} + \frac{S_0}{u^2} (v'_{0\parallel} - S_0) > 0 . \quad (5.24)$$

The allowed regions of the speed u for the localized nonlinear solitary wave solution are shown in Fig. 5.4 for given $v'_{0\parallel}$, and in Fig. 5.5 for given S_0 . From Fig. 5.5, we can see that when $v'_{0\parallel} \geq 1.43$ with $S_0 = 0.2$, the motion of the solitary vortices becomes totally dominant in the system.

It should be noted that with the local approximation the dipole solutions described in Eqs. (5.19) and (5.23) belong to modon type, and without

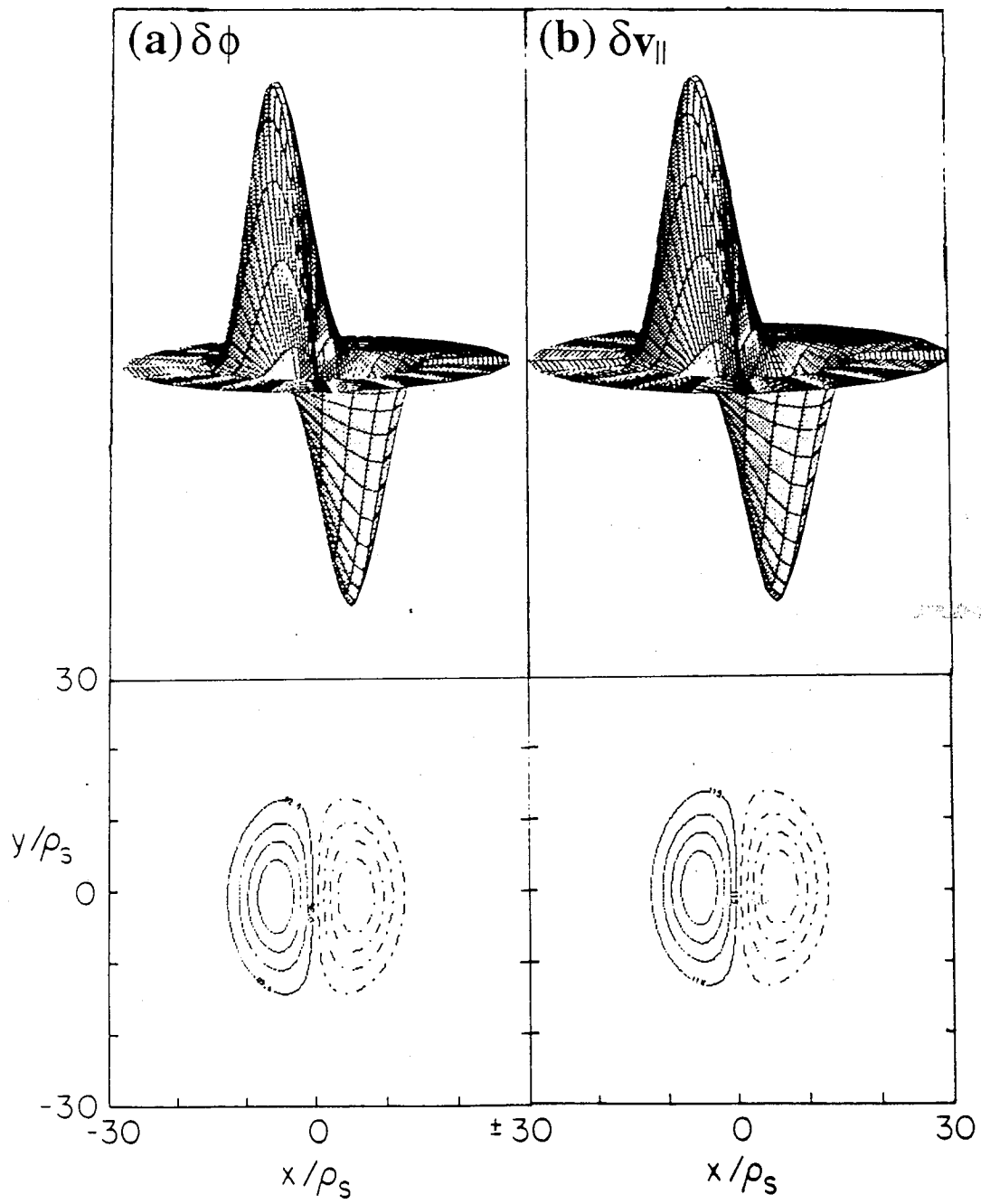


Figure 5.3: 3-D and contour plots of the stationary dipole vortex solutions given in Eqs. (5.19) and (5.23) for $u = -0.4$, $r_0 = 16$, $v'_{0||} = 0.7$ and $S_0 = 0.2$.

Solid and dashed lines in the contour plot represent the positive and negative values, respectively. (a) for $\delta\phi(x, y)$ and (b) for $\delta v_{||}(x, y)$.

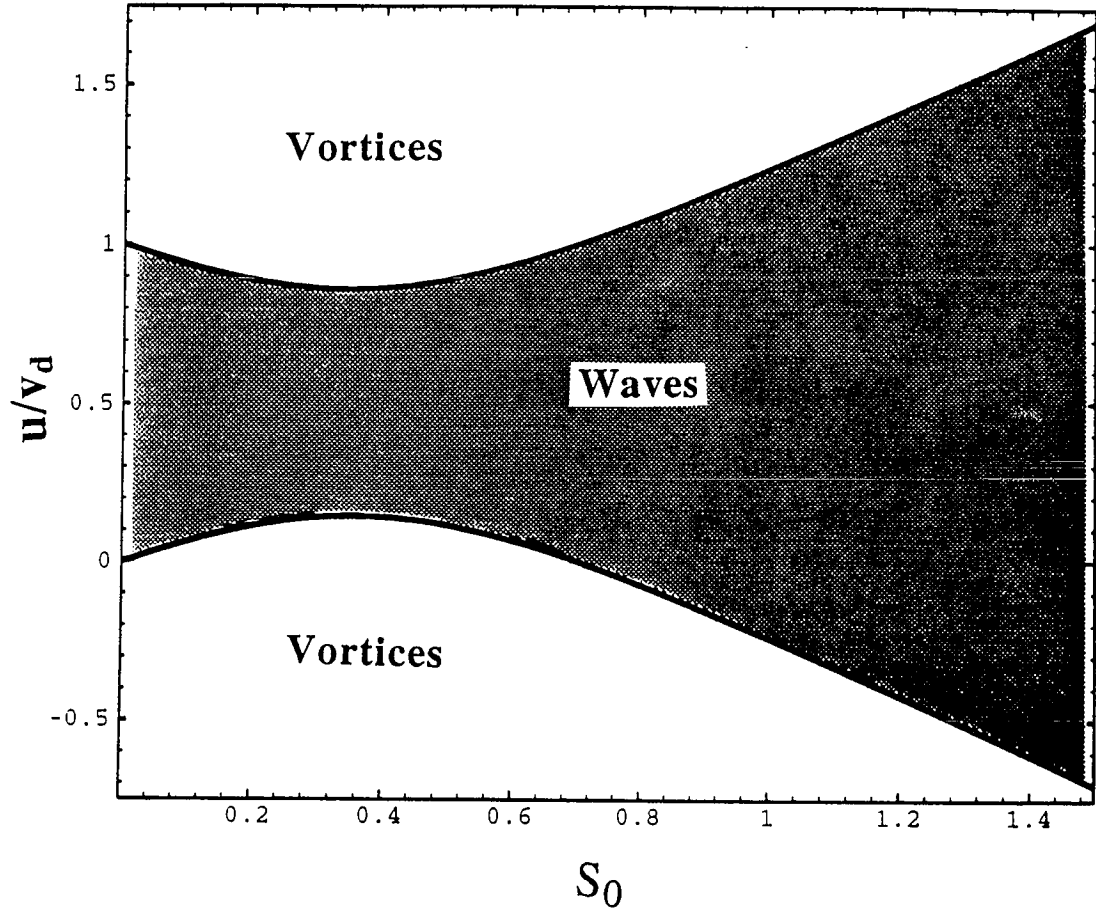


Figure 5.4: Plot of speed u versus S_0 for $v'_{0||} = 0.7$.

Allowed speeds for the solitary vortex solution are the unshaded regions. Linear drift waves have phase speeds in the shaded region.

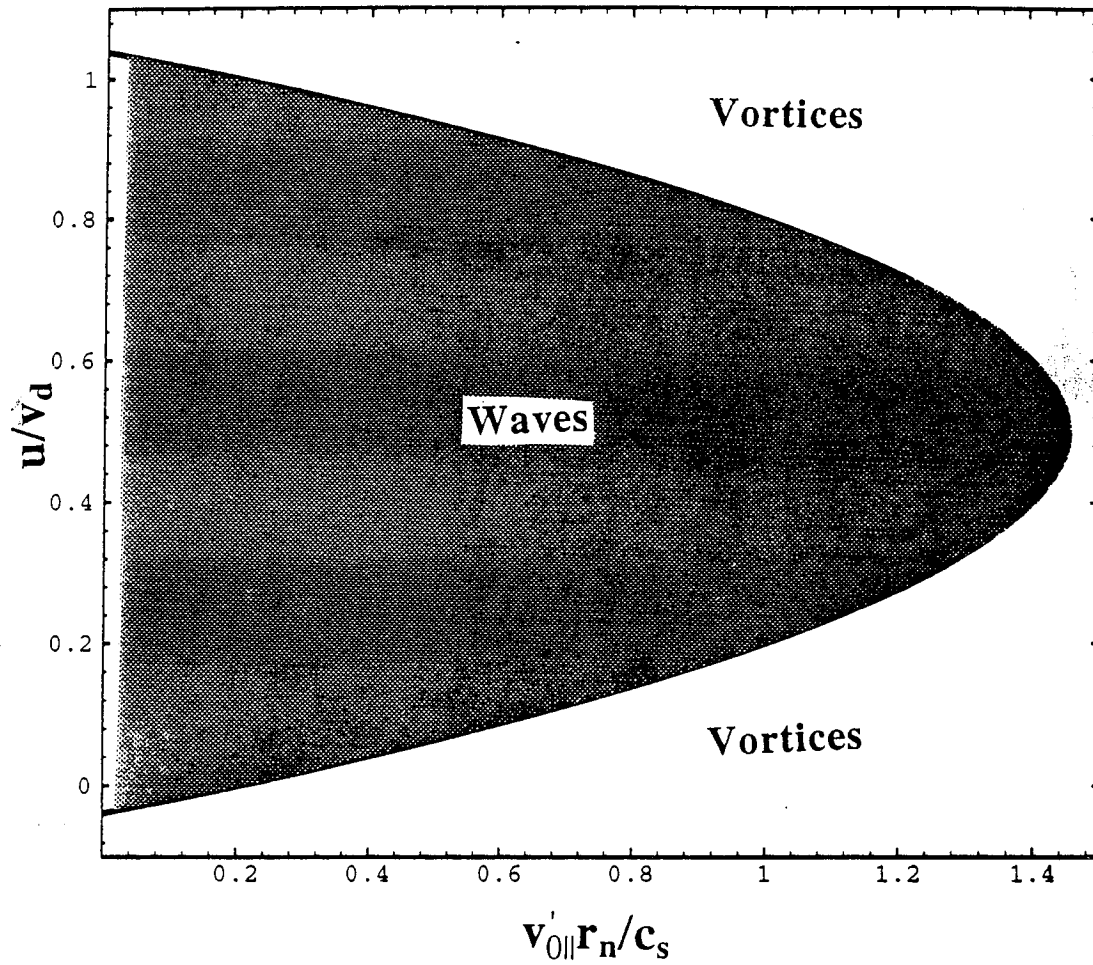


Figure 5.5: Plot of speed u versus $v'_{0||}$ for $S_0 = 0.2$.

Allowed speeds for the solitary vortex solution are the unshaded regions. Linear drift waves have phase speeds in the shaded region.

using local approximation, that is, when magnetic shear exists, a new kind of dipole vortex structure emerges. The detail studies of the new dipole vortex are given in Chapter 4.

5.4 The Simulations

In this section, we report and discuss the results of numerical simulation of the parallel sheared flow driven instability and establish a scenario for the instability evolution and formation of coherent vortex structures. The model equations are based on Eqs. (5.3) and (5.4) derived in Sec. 5.2. We numerically solve the set of equations in the two cases, The first case deals with the local mode in which k_{\parallel} and B_y are constants, and the other case is for the global mode in which k_{\parallel} and B_y are functions of x , that is, a case with presence of magnetic shear.

5.4.1 Local case

With the local approximation, in which $k_{\parallel} = S_0 k_y = \text{const.}$, Eqs. (5.3) and (5.4) become uniform in space. Therefore we can solve these equations with a periodic boundary condition. We Fourier transform Eqs. (5.3) and (5.4) with wavenumber vectors

$$\mathbf{k}_{\perp} = l\Delta k_x \hat{\mathbf{x}} + m\Delta k_y \hat{\mathbf{y}} ,$$

$$k_{\parallel} = S_0 m \Delta k_y ,$$

where l and m are integers and Δk_x and Δk_y are the minimum wavenumbers in the x and y directions, respectively. In the $k_x k_y$ space, Eqs. (5.3) and (5.4)

can be written as

$$(1 + k^2) \frac{\partial \delta \varphi_k}{\partial t} = -(iv_d k_y + \mu_\perp k^4) \delta \varphi_k + \left\{ [\delta \varphi, \nabla^2 \delta \varphi] \right\}_k - i S_0 k_y \delta v_{\parallel k}, \quad (5.25)$$

$$\frac{\partial \delta v_{\parallel k}}{\partial t} = i k_y (v'_{0\parallel} - S_0) \delta \varphi_k - \left\{ [\delta \varphi, \delta v_{\parallel}] \right\}_k - \nu_\perp k^2 \delta v_{\parallel k}, \quad (5.26)$$

where the Poisson-bracket $\left\{ [f, g] \right\}_k$ is evaluated by first transforming the functions f and g into x, y space as follows,

$$\begin{aligned} i k_x f_k &\longrightarrow \frac{\partial f}{\partial x} \quad \text{and} \quad i k_y f_k \longrightarrow \frac{\partial f}{\partial y}, \\ i k_x g_k &\longrightarrow \frac{\partial g}{\partial x} \quad \text{and} \quad i k_y g_k \longrightarrow \frac{\partial g}{\partial y}, \end{aligned}$$

then calculating the Poisson bracket in xy space by

$$P(x, y) = [f, g] = \frac{\partial f}{\partial x} \frac{\partial g}{\partial y} - \frac{\partial f}{\partial y} \frac{\partial g}{\partial x},$$

and finally transforming $P(x, y)$ into $k_x k_y$ space by using *FFT*. During the whole process, the truncation of k space is implemented.

The number of mesh points used in the simulation is typically 85×85 and $\Delta k_x = \Delta k_y = 0.1$. The method of the fifth and sixth order Runge-Kutta time stepping is used to do the time integrations of Eqs. (5.25) and (5.26). The stability of the numerical scheme is ensured by monitoring changes in conserved quantities of Eqs. (5.25) and (5.26) without viscosity terms.

We first started with many small amplitude waves as initial profiles for $\delta \varphi(x, y, t = 0)$ and $\delta v_{\parallel}(x, y, t = 0)$, and confirmed that the observed growth rate spectra in the simulation agree well with the theoretical linear growth rate spectra obtained in Sec. 5.2. The simulation with a higher resolution (170×170 grid points) confirmed the results obtained from the simulation of 85×85 grid

points, since as a result of the viscosity in Eqs. (5.25) and (5.26), short length scale waves are heavily damped and play no significant role in the physical system.

In the first case, we choose

$$\delta\varphi(x, y, t = 0) = \delta v_{\parallel}(x, y, t = 0) = A \sin(k_x x + k_y y)$$

as initial conditions in xy space, where

$$k_x = 4\Delta k_x, \quad k_y = 6\Delta k_y, \quad \Delta k_x = \Delta k_y = \frac{2\pi}{L_x} = 0.1$$

with the amplitude $A = 0.1$, $v'_{0\parallel} = 0.7$, $S_0 = 0.2$, $\mu_{\perp} = 0.01$, and $\nu_{\perp} = 0.02$. The evolution of contours of electric potential $\delta\varphi$ and parallel velocity δv_{\parallel} are shown in Figs. (5.6) and (5.7), respectively. The wave initially launched grows linearly first, followed by an excitation of higher k harmonic modes. At about $t = 230$, when the amplitude of the initially launched wave exceeds a value of about $\varphi_m \sim v_{\parallel m} \sim 0.2$, the nonlinear interactions among the modes become important and energy transfer to many modes erupts, which causes the wave to break up into many small vortices. Then the small vortices start to interact with each other and the coalescing and pairing processes emerge. As the result of coalescence, the small scale vortices fuse into larger scale ones, which, from the point of view of mode energy in k space, indicates occurring of inverse cascade of wave energy. The evolution of a typical wavenumber spectrum of energy is shown in Fig. 5.10. The continuous processes of coalescing and pairing result in formation of a single, large, isolated and stable dipole vortex structure with amplitude $\varphi_m \simeq 30$ which propagates towards negative y direction with a speed $u \sim 0.4$ in a rotating manner. From Figs. 5.4 and 5.5 we notice that

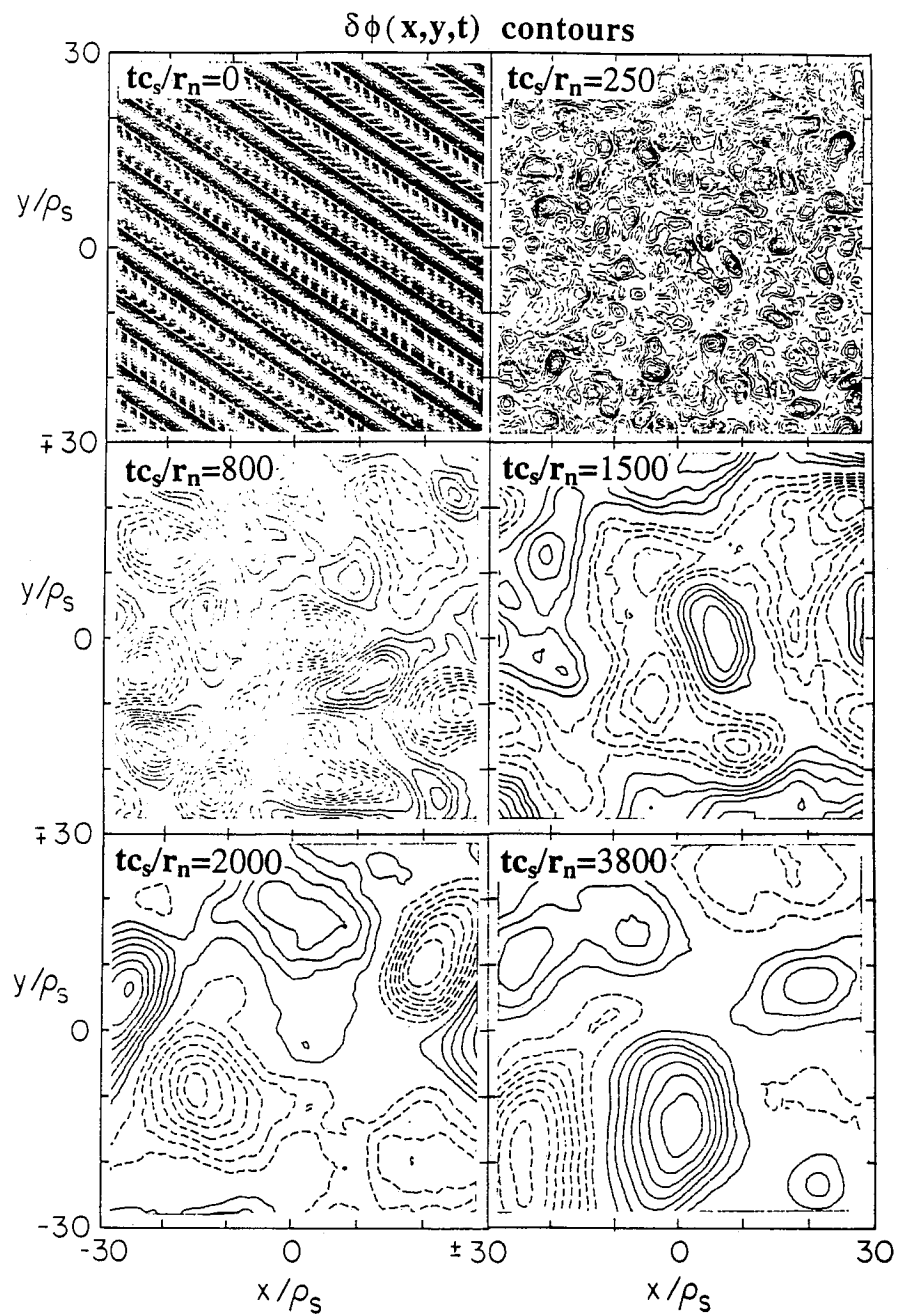


Figure 5.6: The time evolution of the contours of electric potential $\delta\phi(x,y,t)$ for $v'_{0\parallel} = 0.7$, $B_y/B_0 = S_0 = 0.2$, $\mu_{\perp} = 0.01$, and $\nu_{\perp} = 0.02$.

The solid and dashed lines represent the positive and negative values of the potential $\delta\phi$, respectively.

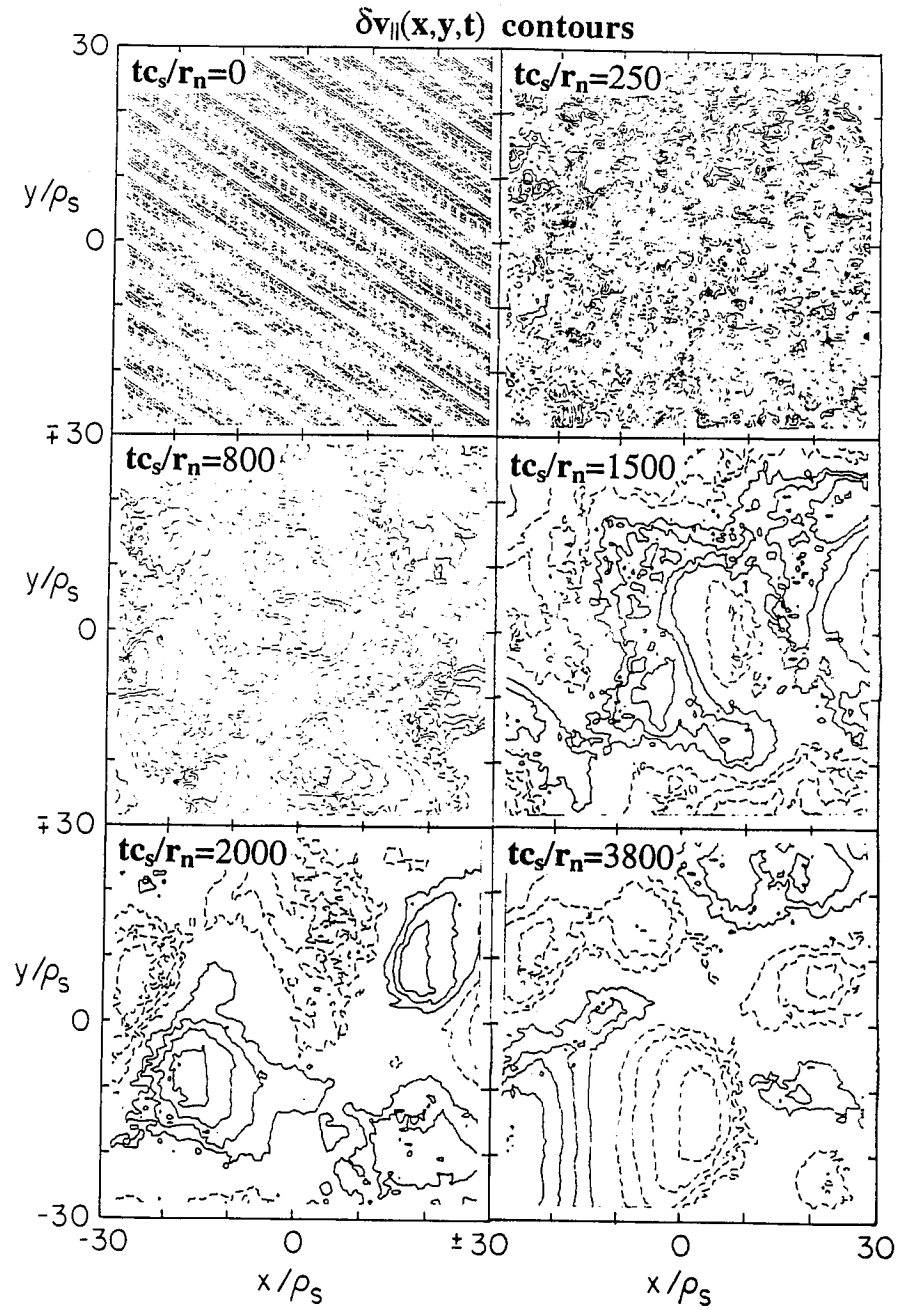


Figure 5.7: The time evolution of the contours of parallel velocity $\delta v_{\parallel}(x,y,t)$ for $v'_{0\parallel} = 0.7$, $B_y/B_0 = S_0 = 0.2$, $\mu_{\perp} = 0.01$, and $\nu_{\perp} = 0.02$.

The solid and dashed lines represent the positive and negative values of the parallel velocity δv_{\parallel} , respectively.

the speed of the observed dipole vortex structure is within the zone allowed for solitary vortex solutions.

In the second case, we start with a Gaussian monopole vortex for both $\delta\varphi$ and δv_{\parallel} ,

$$\delta\varphi(x, y, t = 0) = \delta v_{\parallel}(x, y, t = 0) = 0.7 \exp\left(-\frac{x^2 + y^2}{36}\right)$$

as initial perturbation and $v'_{0\parallel} = 0.6$, $S_0 = 0.2$, $\mu_{\perp} = \nu_{\perp} = 0.01$.

The initial monopole vortex is seen to break up into many small vortices and waves in the initial stage of the evolution during which the linear instability is dominated. At around $t = 100$, nonlinear effect sets in and the coalescing and pairing processes become the main processes of the evolution and as in the first case, the small vortices fuse into larger ones. The evolutions of $\delta\varphi$ and δv_{\parallel} are shown in Figs. 5.8 and 5.9, respectively.

Comparing the first case with the second case, we notice that the contours of $\delta\varphi$ and δv_{\parallel} at around time $t = 800$ in the first case shown in Figs. 5.6(c) and 5.7(c) have same patterns as those at the same time in the second case shown in Figs. 5.8(c) and 5.9(c), although the very different initial conditions for $\delta\varphi$ and δv_{\parallel} are used in each case. We also notice that the fusion process of smaller vortices into larger ones in the second case is significant slower than that in the first case. The reason for this may be due to a larger driven $v'_{0\parallel} = 0.7$ and damping $\mu_{\perp} = 0.01$ and $\nu_{\perp} = 0.02$ in the first case, comparing with $v'_{0\parallel} = 0.6$ and $\mu_{\perp} = \nu_{\perp} = 0.01$ in the second case. A larger driven force may supply more free energy and therefore enhance the feeding process of energy to coherent structure from random wave packets [Tsytovich and Shukla, 1991]. A larger damping force will enhance the relaxation process.

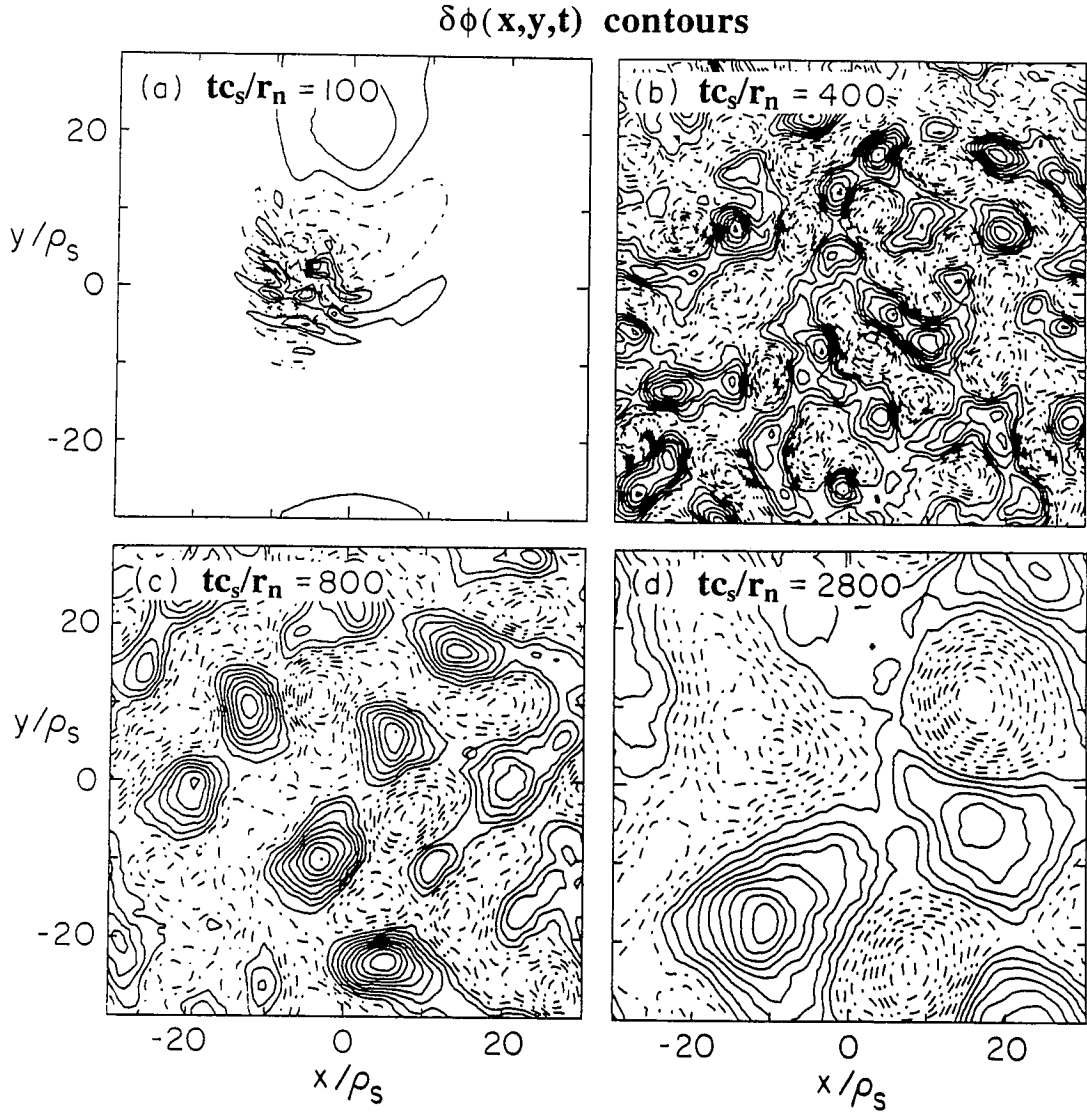


Figure 5.8: The time evolution of the contours of electric potential $\delta\phi(x,y,t)$ for $v'_{0\parallel} = 0.6$, $B_y/B_0 = S_0 = 0.2$, and $\mu_{\perp} = \nu_{\perp} = 0.01$.

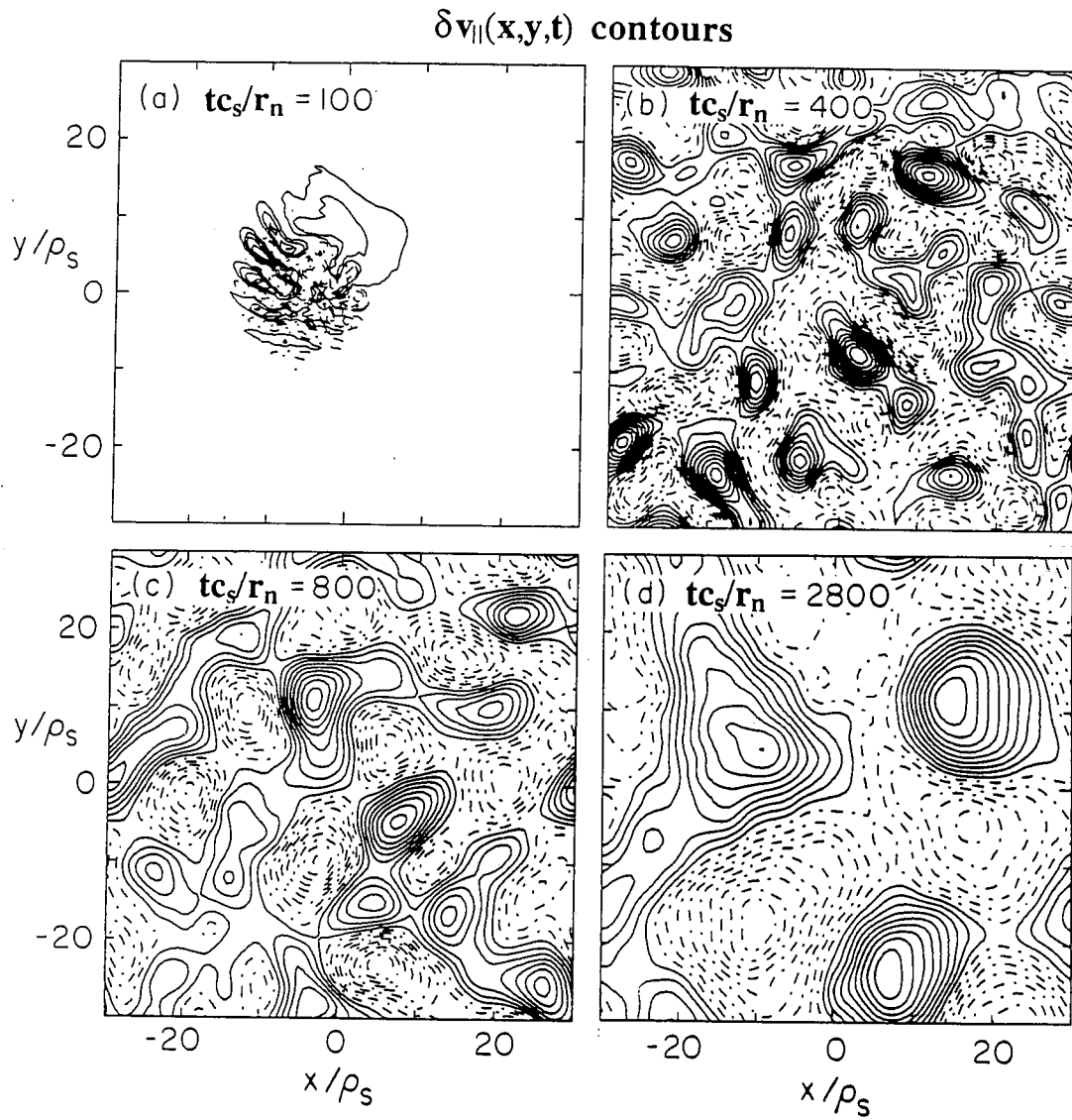


Figure 5.9: The time evolution of the contours of parallel velocity $\delta v_{\parallel}(x,y,t)$ for $v'_{0\parallel} = 0.6$, $B_y/B_0 = S_0 = 0.2$, and $\mu_{\perp} = \nu_{\perp} = 0.01$.

The self-organization has been observed during the relaxation process in a 3-D simulation study [Horiuchi and Sato, 1985].

The inverse cascade of energy during the fusion of small vortices into larger ones in the second case is clearly shown in Fig. 5.10, which features in the evolution of wavenumber spectrum of total energy, where time average energy spectra are defined as

$$E(k_x) = \sum_{k_y} E(k_x, k_y) \quad \text{and} \quad E(k_y) = \sum_{k_x} E(k_x, k_y) .$$

In the time interval of $50 < t \leq 250$ in Fig. 5.10(a) and (b), the peak energy appears around $k_x \rho_s \sim k_y \rho_s \sim 0.8$ and the peak energy level is order of 10^{-2} , while later in the time interval of $2250 < t \leq 2500$ in Fig. 5.10(c) and (d), the peak energy appears at $k_x \rho_s \sim 0.4$ and $k_y \rho_s \sim 0.15$ and the peak energy level increases to order of 10^{-1} . We also notice that in the later time interval the energy spectra have a steep drop-off at around $k_x \rho_s \sim k_y \rho_s \sim 0.5$.

In addition, the wavenumber spectrum of energy after a long-time evolution is shown to obey a power law,

$$\sum_{k_x} E(\mathbf{k}) \sim k_y^{-2 \pm \delta} \quad \text{and} \quad \sum_{k_y} E(\mathbf{k}) \sim k_x^{-2 \pm \delta} ,$$

in the intermediate range ($0.6 < k_{\perp} < 2.0$) and

$$\sum_{k_x} E(\mathbf{k}) \sim k_y^{-3 \pm \delta} \quad \text{and} \quad \sum_{k_y} E(\mathbf{k}) \sim k_x^{-3 \pm \delta} ,$$

in the inertial range ($2.0 < k_{\perp} < 5.0$) with $\delta \simeq 0.2$ to 0.3 . Here $k_{\perp} \simeq 2$ is the boundary between the two regions. We also notice that from Fig. 5.1 the largest growth rate is around $k_y \simeq 2$.

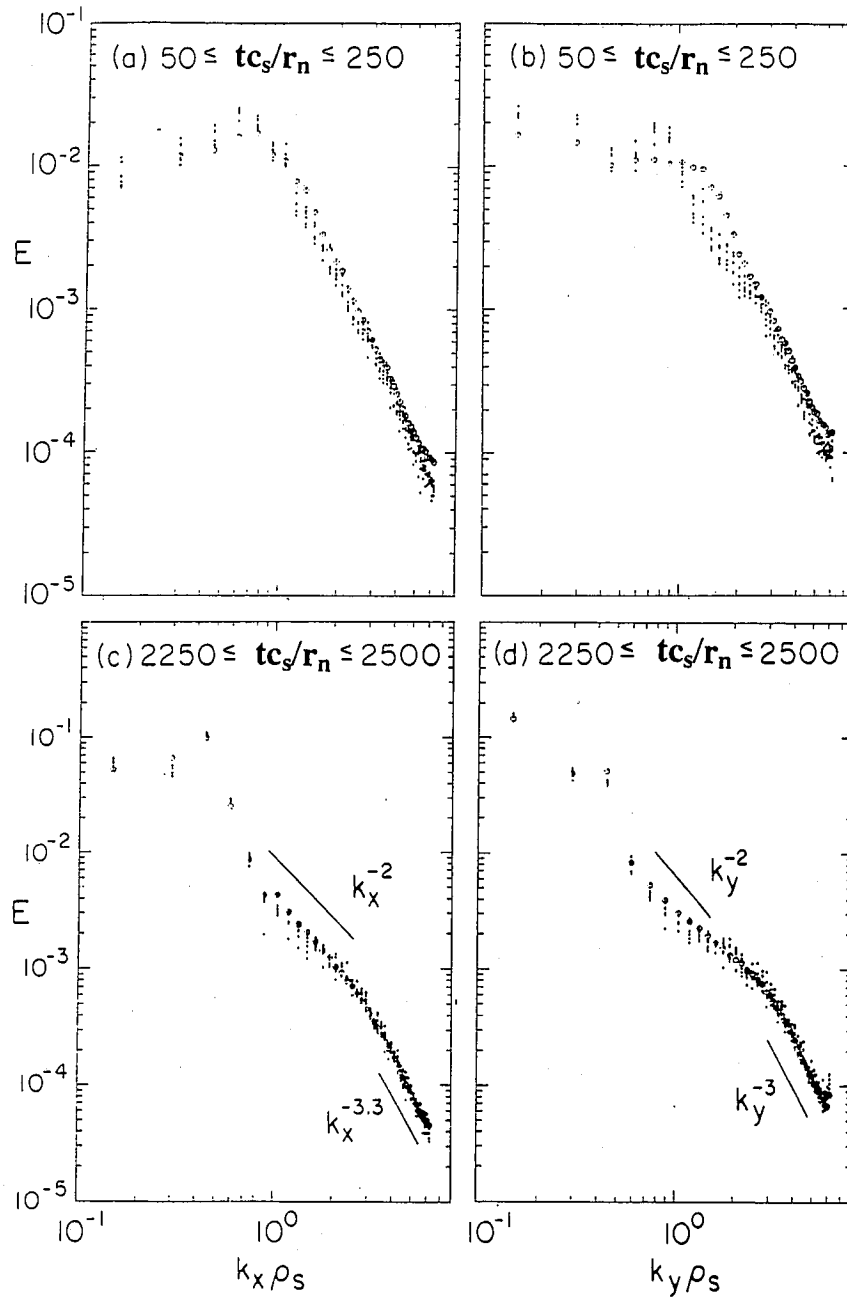


Figure 5.10: The wavenumber spectra of the time average total energy for a early time interval $50 \leq tc_s/r_n \leq 250$ and a later time interval $2250 \leq tc_s/r_n \leq 2500$ for the case in Figs. (5.8) and (5.9).

The dots represent the values of time average over every 10 time step in the last 50 time steps of the corresponding time interval. The circles represent the values of time average over the whole corresponding time interval.

In the xy space, the inverse cascade appears as coalescence of same signed smaller vortices to form larger coherent vortex structures. Thus, part of the free energy stored in the parallel sheared flow is transferred or fed into larger scale vortex structures through random wave packets [Tsytovich and Shukla, 1991] or small scale field [Muhm *et al.*, 1991 and 1992], and part of energy is coupled to small scale waves where it is absorbed by viscosity represented by μ_{\perp} and ν_{\perp} terms in Eqs. (5.25) and (5.26).

5.4.2 Nonlocal case

In the nonlocal case, periodic B_y is taken by allowing the tilt angle to vary as

$$\frac{B_y}{B_0} = S_m \sin\left(\frac{2\pi}{L_x}x\right),$$

so that k_{\parallel} ($= S_m \sin(2\pi x/L_x)k_y$) depends on the space variable x , where $L_x = 20\pi\rho_s$ is the simulation box length in x -direction. Fourier representation for the y variable and a finite difference method for the x variable are employed. The same numerical scheme as that described in Sec. 4.5 of the preceding chapter is used to evaluate the nonlinear terms and to do the time integration.

In this third case, the initial conditions are chosen as

$$\delta\varphi(x, y, t = 0) = \delta v_{\parallel}(x, y, t = 0) = A \sin(k_n x) \cos(6k_n y)$$

with the amplitude $A = 0.1$, $k_n = 2\pi/L_x = 0.1$ for $v'_{0\parallel} = 0.6$, $S_m = 0.4$, and $\mu_{\perp} = \nu_{\perp} = 0.01$. The time evolution of $\delta\varphi$ and δv_{\parallel} observed in this case is similar to the previous case: a fast linear growth is accompanied by formation of many small scale vortices, and followed by fusing of the small vortices into

larger ones. The contour plots of electric potential $\delta\varphi(x, y, t)$ and the parallel velocity $\delta v_{\parallel}(x, y, t)$ are presented in Figs. 5.11 and 5.12, respectively.

It should be noted that after the early nonlinear $\mathbf{E} \times \mathbf{B}$ trapping or phase mixing at time of order $tc_s/r_n \sim 100$ in the second case with a constant B_y , a slow coalescence process continues and the vortices continue to merge and grow in diameter. At the final time $tc_s/r_n \sim 2800$ in Figs. 5.8(d) and 5.9(d), the diameters of the vortices are order of $10\rho_s$. However, in the present nonlocal case with the sheared magnetic field, the growth of vortices stops at around $tc_s/r_n \sim 250$. The length scale of the turbulent vortices in this case is about order of $5\rho_s$. Thus the presence of the non-constant B_y field significantly reduces the strength of the turbulent mixing across the sheared flow layer of plasmas.

We also notice that the non-constant B_y field has a stabilizing effect. In Fig. 5.13 we show the energies as functions of time for $v'_{0\parallel} = 0.6$, $B_y/B_0 = 0.4 \sin(2\pi x/L_x)$, and $\mu_{\perp} = \nu_{\perp} = 0.01$, where $E_T = E_{\varphi} + E_{v_{\parallel}}$ is total energy; $E_{\varphi} = [\delta\varphi^2 + (\nabla\delta\varphi)^2]/2$; and $E_{v_{\parallel}} = \delta v_{\parallel}^2/2$. The total energy in this case clearly is shown saturated after $tc_s/r_n \sim 200$. With the driven $v'_{0\parallel}$ and damping μ_{\perp} and ν_{\perp} same as those in the case depicted in Fig. 5.13, and $B_y/B_0 = \text{constant} = 0.2$, we redo the experiment and find that the total energy level reaches same level at $tc_s/r_n \sim 200$ as that in Fig. 5.13, but in the current case the energy can not be saturated. The time development of energies for the current case is shown in Fig. 5.14.

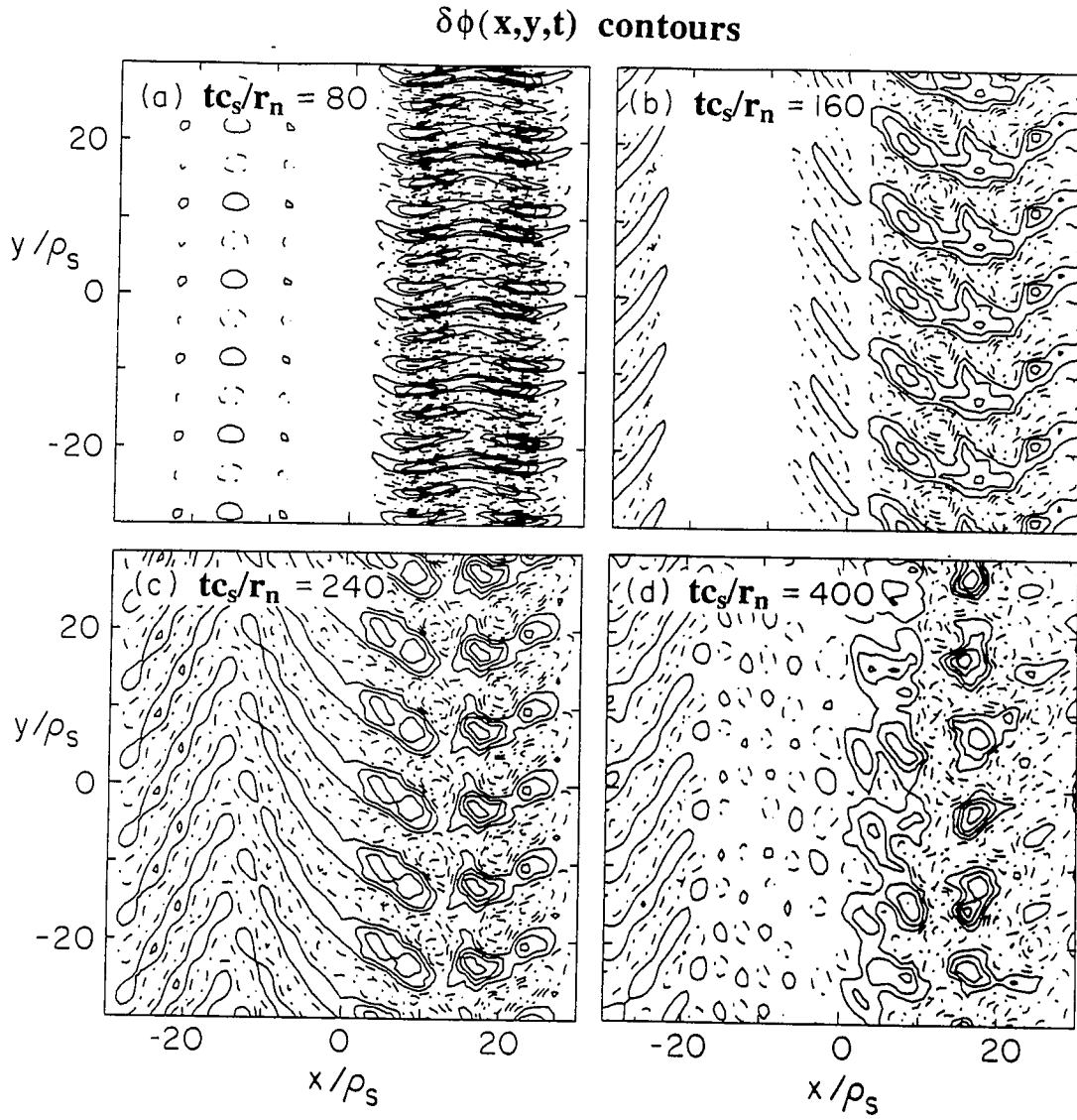


Figure 5.11: The time evolution of the contours of electric potential $\delta\phi(x,y,t)$ for $v'_{0\parallel} = 0.6$, $B_y/B_0 = 0.4 \sin(2\pi x/L_x)$, and $\mu_{\perp} = \nu_{\perp} = 0.01$.

The solid and dashed lines represent the positive and negative values of the potential $\delta\phi$, respectively.

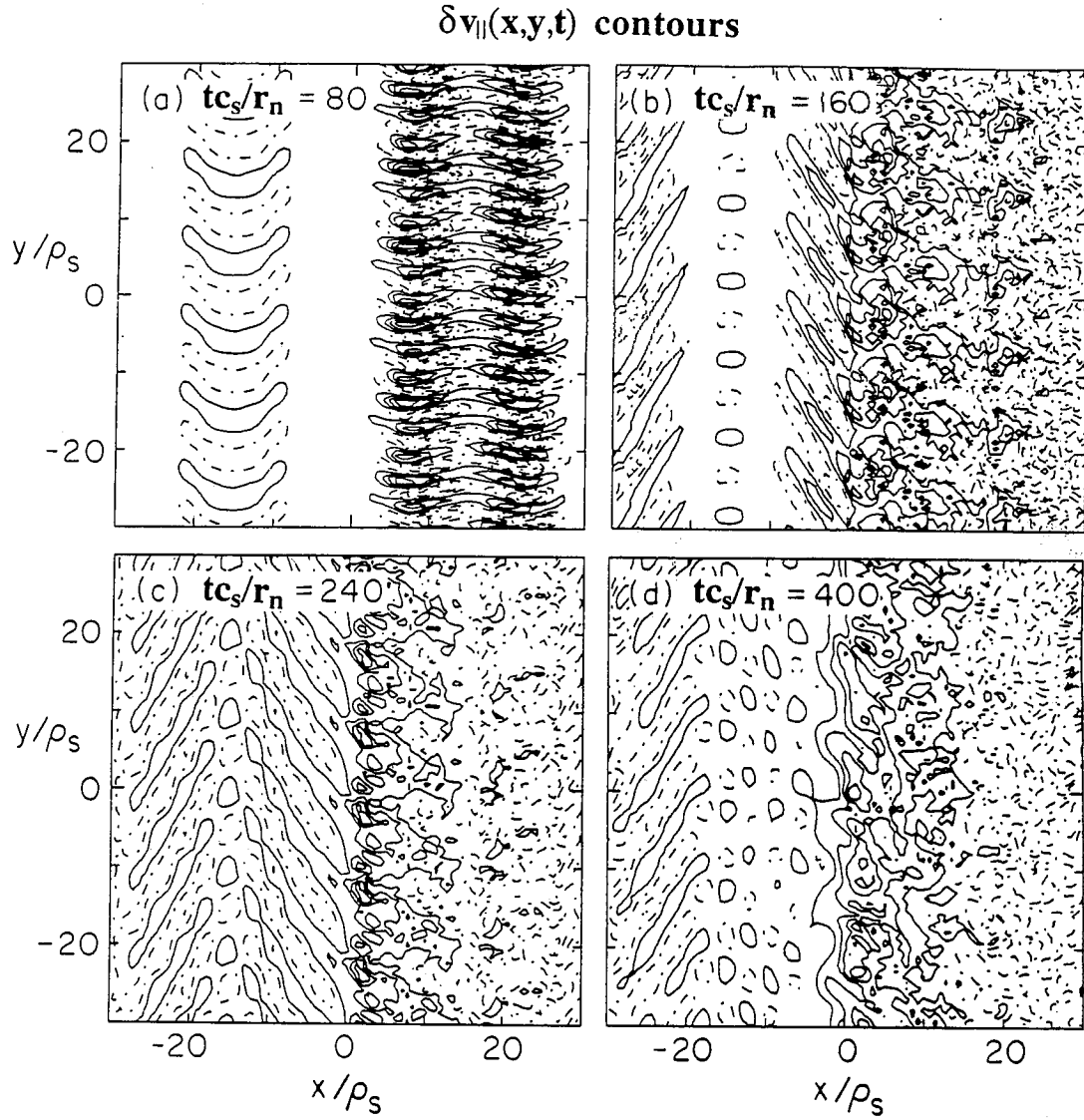


Figure 5.12: The time evolution of the contours of parallel velocity $\delta v_{\parallel}(x, y, t)$ for $v'_{0\parallel} = 0.6$, $B_y/B_0 = 0.4 \sin(2\pi x/L_x)$, and $\mu_{\perp} = \nu_{\perp} = 0.01$.

The solid and dashed lines represent the positive and negative values of the parallel velocity δv_{\parallel} , respectively.

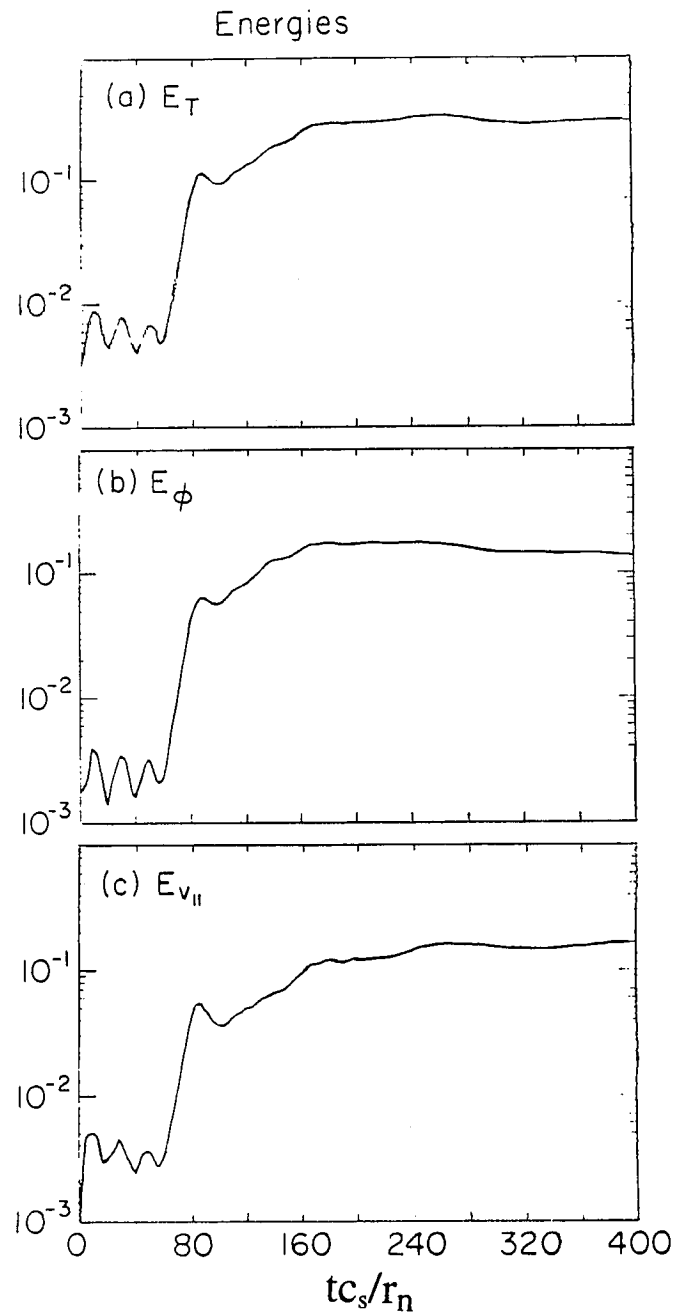


Figure 5.13: The time evolution of the energies for $v'_{0||} = 0.6$, $B_y/B_0 = 0.4 \sin(2\pi x/L_x)$, and $\mu_\perp = \nu_\perp = 0.01$.

E_T , E_ϕ , and $E_{v_{||}}$ represent the total, electric, and kinetic energy, respectively.

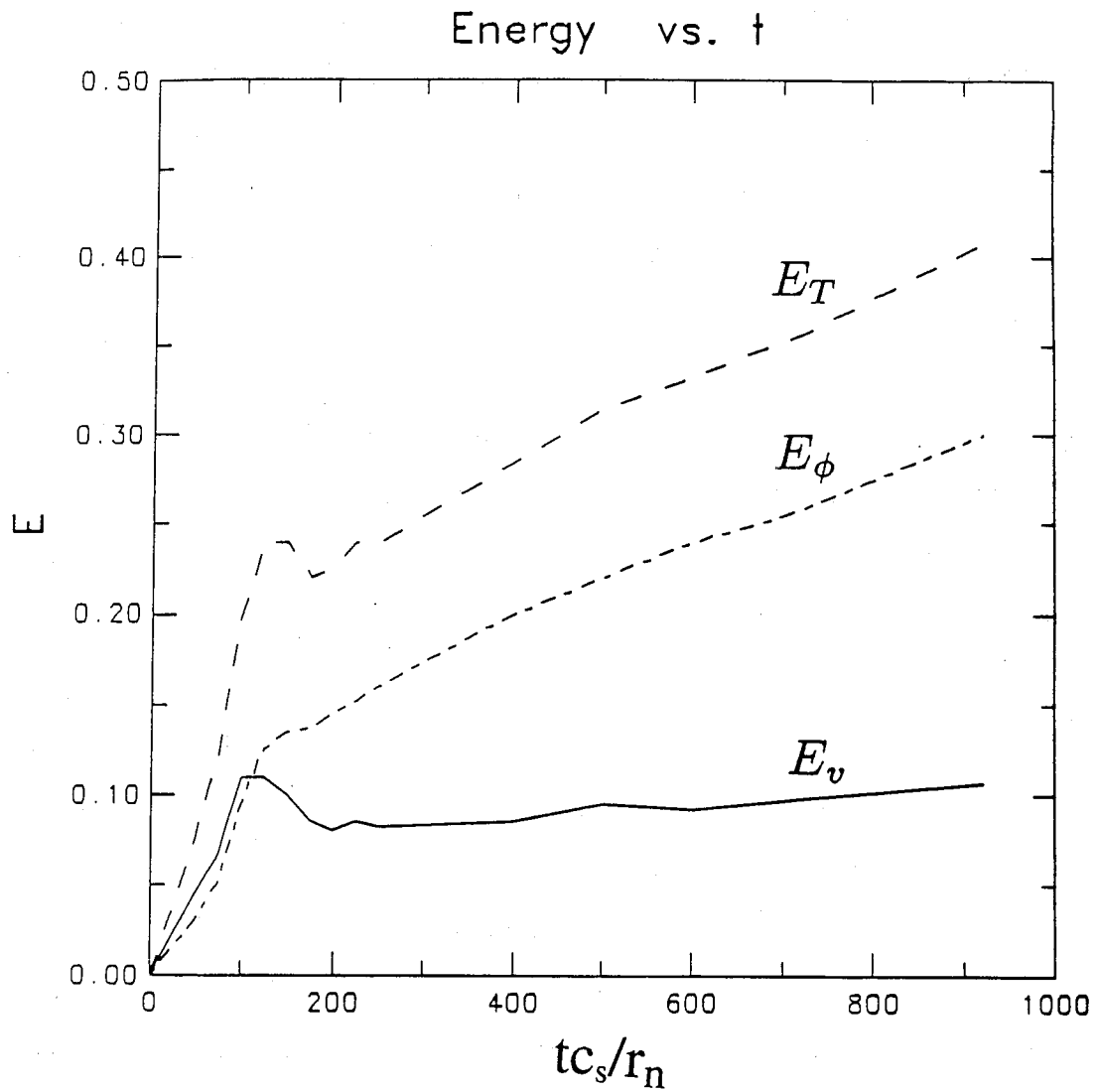


Figure 5.14: The time evolution of the energies for $v'_{0\parallel} = 0.6$, $B_y/B_0 = S_0 = 0.2$, and $\mu_\perp = \nu_\perp = 0.01$.

5.5 Summary and Discussion

In this chapter, we have studied the formation of a coherent structure through turbulence in the course of nonlinear development of the parallel or toroidal sheared flow driven drift instability. We have derived a model made of the coupled vorticity and parallel mass flow equations with effects of sheared flow and viscosity. The studies of linear instability show that the spectral structure of the growth rate is characterized by the finite bandwidth for the instability. Analytically, we have found the exact localized stationary dipole vortex solutions for the nonlinear equations describing the parallel sheared flow driven turbulence with finite constant B_y , or $k_{\parallel} = \text{const.}$. The dipole vortex solution is shown to be a generalization of the modon type given first by Larichev and Reznik [1976].

Numerical simulations based on the model equations are performed in the two-dimension. A scenario for the instability evolution has been established as follows. The initial exponential growth of a linear instability is followed by the excitation of many modes through nonlinear interaction. At the same time the waves break up into a random ensemble of many small scale vortices. Then the inverse cascade of the wave energy sets in, which in xy space appears as coalescing of same signed small vortices to form larger scale vortex structures and pairing of opposed signed vortices to form dipole type vortex structures. The coalescing process is repeated to give rise to a single large dipole type vortex structure which is similar to a modon. The energy needed to form the large vortex comes from the free energy stored in the sheared flow. Part of the free energy is transferred through the collective drift modes into the large vortex and part of the free energy goes to small scale modes by mode-coupling

process, where the energy is absorbed by viscosity.

The energy spectrum shows a steep drop-off at critical wavenumber $k_x \rho_s \sim k_y \rho_s \sim 0.5$ due to the strong inverse cascade and the formation of the large and long-lived vortices. The wavenumber spectrum of energy is found to obey a power law $E(k) \sim k^{-2 \pm 0.3}$ in intermediate range ($0.6 < k < 2$) and $E(k) \sim k^{-3 \pm 0.3}$ in inertial range ($2 < k < 5$).

The presence of magnetic shear significantly affects the instability evolution. We have found that magnetic shear hinders the inverse cascade process of the wave energy and thus the formation of large scale vortices. This is because the strength of the turbulent mixing across the sheared flow layer of plasmas is greatly reduced due to the shearing of the magnetic field structure and so that the free energy is easily absorbed by viscosity in the small scale modes before it is transferred to large scale structures.

Appendix A

Noncanonical Hamiltonian Structure

In this appendix, we systematically construct the invariants and develop Casimir noncanonical Hamiltonian structures of the system described by Eqs. (4.4) and (4.5) in Sec. 4.2 of Chapter 4.

The vorticity Eq. (4.4) and the parallel momentum Eq. (4.5) with the Boltzmann density distribution n given in Eq. (4.6) can be rewritten to order ϵ and ϵ^2 for $\partial/\partial z = 0$ as follows:

$$\frac{\partial q}{\partial t} + [\varphi, q] = S(x) \frac{\partial v_{\parallel}}{\partial y}, \quad (\text{A.1})$$

$$\frac{\partial v_{\parallel}}{\partial t} + [\varphi, v_{\parallel}] = -S(x) \frac{\partial \varphi}{\partial y}, \quad (\text{A.2})$$

where the potential vorticity $q(x, y, t) = \nabla^2 \varphi - \varphi/T(x) - \ell n(n_0(x))$.

The Hamiltonian is, from Eq. (4.11),

$$\begin{aligned} H(q, v_{\parallel}) &= \frac{1}{2} \int \left[\frac{\varphi^2}{T(x)} + (\nabla \varphi)^2 + v_{\parallel}^2 \right] dx dy \\ &= \frac{1}{2} \int \left(-q\varphi - \varphi \ell n_0 + v_{\parallel}^2 \right) dx dy, \end{aligned} \quad (\text{A.3})$$

where surface terms are neglected. Upon variation of H ,

$$\delta H = \int \left(-\varphi \delta q + v_{\parallel} \delta v_{\parallel} \right) dx dy,$$

and we obtain the functional derivative

$$\frac{\delta H}{\delta q} = -\varphi; \quad \frac{\delta H}{\delta v_{\parallel}} = v_{\parallel}. \quad (\text{A.4})$$

Equations (A.1) and (A.2) can be written in Hamiltonian form,

$$\frac{\partial q}{\partial t} = \{q, H\} , \quad (\text{A.5})$$

$$\frac{\partial v_{\parallel}}{\partial t} = \{v_{\parallel}, H\} , \quad (\text{A.6})$$

where the noncanonical Poisson bracket $\{F, G\}$ is defined as

$$\begin{aligned} \{F, G\} = \int \left\{ q \left[\frac{\delta F}{\delta q}, \frac{\delta G}{\delta q} \right] + (v_{\parallel} - \sigma(x)) \left(\left[\frac{\delta F}{\delta v_{\parallel}}, \frac{\delta G}{\delta q} \right] \right. \right. \\ \left. \left. + \left[\frac{\delta F}{\delta q}, \frac{\delta G}{\delta v_{\parallel}} \right] \right) \right\} dx dy , \end{aligned} \quad (\text{A.7})$$

where $\sigma(x) = \int^x S(x') dx'$.

It is easily shown that the Poisson bracket given by Eq. (A.7) is antisymmetric,

$$\{F, G\} = -\{G, F\} ,$$

and one can prove it satisfies Jacobi's identity,

$$\{E, \{F, G\}\} + \{F, \{G, E\}\} + \{G, \{E, F\}\} = 0 .$$

(A proof for essentially the same bracket can be found in Morrison and Hazeltine [1984].)

The Casimir invariants C of the Poisson bracket are defined by

$$\{C, D\} = 0 , \quad (\text{A.8})$$

where D is an arbitrary function. Substituting Eq. (A.8) into Eq. (A.7), we obtain

$$\begin{aligned} \{C, D\} = \int \left\{ q \left[\frac{\delta C}{\delta q}, \frac{\delta D}{\delta q} \right] + (v_{\parallel} - \sigma(x)) \left(\left[\frac{\delta C}{\delta v_{\parallel}}, \frac{\delta D}{\delta q} \right] \right. \right. \\ \left. \left. + \left[\frac{\delta C}{\delta q}, \frac{\delta D}{\delta v_{\parallel}} \right] \right) \right\} dx dy = 0 . \end{aligned} \quad (\text{A.9})$$

Using the identity,

$$\int f[g, h] dx dy = \int h[f, g] dx dy , \quad (\text{A.10})$$

we can rewrite Eq. (A.9) as

$$\begin{aligned} & \int \left\{ \frac{\delta D}{\delta q} \left[q , \frac{\delta C}{\delta q} \right] + \frac{\delta D}{\delta q} \left[(v_{\parallel} - \sigma(x)) , \frac{\delta C}{\delta v_{\parallel}} \right] \right. \\ & \left. + \frac{\delta D}{\delta v_{\parallel}} \left[(v_{\parallel} - \sigma(x)) , \frac{\delta C}{\delta q} \right] \right\} dx dy = 0 . \end{aligned} \quad (\text{A.11})$$

Since D is arbitrary its coefficient must vanish, and we can find two independent Casimirs, from Eq. (A.11)

$$C_1 = \int f[v_{\parallel} - \sigma(x)] dx dy ,$$

$$C_2 = \int qg[v_{\parallel} - \sigma(x)] dx dy ,$$

where f and g are arbitrary functions of their arguments. When $\partial/\partial z \neq 0$, it can be easily shown that

$$\hat{C}_1 = \int q dx dy dz ,$$

$$\hat{C}_2 = \int (v_{\parallel} - \sigma(x)) dx dy dz ,$$

$$\hat{C}_3 = \int q (v_{\parallel} - \sigma(x)) dx dy dz ,$$

survive.

BIBLIOGRAPHY

1. M. Abramowitz and I. A. Stegun, *Handbook of Mathematical Functions with Formulas, Graphs, and Mathematical Tables*, (Dover, New York, 1965), pp. 260–263.
2. S. V. Antipov, M. V. Nezlin, E. N. Snezhkin, and A. S. Trubnikov, *Zh. Eksp. Teor. Fiz.* **82**, 145 (1982), [*Sov. Phys. JETP* **55**, 85 (1982)].
3. S. V. Antipov, M. V. Nezlin, V. K. Rodionov, E. N. Snezhkin, and A. S. Trubnikov, *Zh. Eksp. Teor. Fiz.* **84**, 1357 (1983), [*Sov. Phys. JETP* **57**, 786 (1983)].
4. R. A. Antonova, B. P. Zhvaniya, D. G. Lominadze, D. I. Nanobashvili, and V. I. Petviashvili, *Sov. Phys. JETP Lett.* **37**, 651 (1983).
5. N. S. Buchel'nikova, R. A. Salimov and Yu. I. Edelman, *Zh. Eksp. teor. Fiz.* **52**, 837 (1967), [*Sov. Phys. JETP* **25**, 548 (1967)].
6. J. G. Charney, *Geophys. Public. Kosjones Nors. Videnshap. Akad. Oslo.* **17**, 3 (1948).
7. Y. Couder and C. Basdevant, *J. Fluid Mech.* **173**, 225 (1986).
8. J. F. Drake, J. M. Finn, P. Guzdar, V. Shapiro, V. Shevchenko, F. Waelbroeck, A. B. Hassam, C. S. Liu, R. Sagdeev, *Phys. Fluids B* **4**, 488 (1992).
9. H. Ertel, *Meteorolol. Z.* **59**, 227 (1942).
10. G. R. Flierl, V. D. Larichev, J. C. McWilliams, and G. M. Reznik, *Dyn. Atmos. Ocean* **5**, 1 (1980).

11. S. Hamaguchi and W. Horton, *Phys. Fluids B* **4**, 319 (1992).
12. A. Hasegawa and K. Mima, *Phys. Rev. Lett.* **39**, 205 (1977).
13. A. Hasegawa and K. Mima, *Phys. Fluids* **21**, 87 (1978).
14. A. Hasegawa, C. G. MacLennan, and Y. Kodama, *Phys. Fluids* **22**, 2122 (1979).
15. A. Hasegawa, *J. Phys. Soc. Jpn.* **52**, 1930 (1983).
16. A. Hasegawa and M. Wakatani, *Phys. Rev. Lett.* **50**, 682 (1983).
17. A. Hasegawa, *Advances in Phys.* **34**, 1 (1985).
18. H. W. Hendel, T. K. Chu and P. A. Politzer, *Phys. Fluids* **11**, 2426 (1968).
19. J. R. Holton, *Geophys. Fluids Dynamics* **2**, 323 (1971).
20. S. Horiata and M. Sato, *J. phys. Soc. Jpn.* **56**, 2611 (1987).
21. R. Horiuchi and T. Sato, *Phys. Rev. Lett.* **55**, 211 (1985).
22. W. Horton, *Phys. Rev. Lett.* **37**, 1269 (1976).
23. W. Horton, *Phys. Fluids* **29**, 1491 (1986).
24. W. Horton, J. Liu, J. D. Meiss, and J. E. Sedlak, *Phys. Fluids* **29**, 1004 (1986).
25. W. Horton, T. Tajima, and T. Kamimura, *Phys. Fluids* **30**, 3485 (1987).
26. W. Horton, *Phys. Fluids B* **1**, 524 (1989).
27. W. Horton, X. N. Su, and P. J. Morrison, *Sov. J. Plasma Phys.* **16**, 562 (1990).

28. ^(a)W. Horton, D. Lindberg, X. N. Su, J. Liu, and P. J. Morrison, *Numerical Simulations of Turbulence Problem of Self-Organization*, Proceedings of Workshop on Theory of Fusion Plasmas, Varenna, Italy, August, 1992.
29. ^(b)W. Horton, J. Q. Dong, X. N. Su and T. Tajima, *Ion Mixing in the Plasma Sheet Boundary Layer by Drift Instabilities*, (1992) (Submitted to J. Geophys. Res.)
30. M. Hossian, G. Vahala, and D. Montgomery, Phys. Fluids **28**, 3074 (1985).
31. T. Huld, A. H. Nielsen, H. L. Pecseli and J. Juul Rasmussen, Phys. Fluids B **3**, 1609 (1991).
32. D. Jovanovic and W. Horton, *Quasi-Three Dimensional Electron Holes in Magnetized Plasmas*, Univ. of Texas IFS Rept.# 548 (1992).
33. B. B. Kadomtsev, Comments Plasma Phys. Controlled Fusion **11**, 153 (1987).
34. M. Kono and E. Miyashita, Phys. Fluids **31**, 326 (1988).
35. R. H. Kraichnan, Phys. Fluids **10**, 1417 (1967).
36. V. P. Lakhin, A. B. Mikhailovskii and O. G. Onishchenko, Phys. Lett. A **199**, 348 (1987).
37. V. P. Lakhin, A. B. Mikhailovskii and O. G. Onishchenko, Plasma Phys. Controlled Fusion **30**, 457 (1988).
38. V. D. Larichev and G. M. Reznik, Oceanology **16**, 547 (1976).
39. E. W. Laedke and K. H. Spatschek, Phys. Fluids **31**, 1492 (1988).

40. J. Liu and W. Horton, *Phys. Fluids* **29**, 1828 (1986).
41. W. Magnus and F. Oberhettinger, *Formulas and Theorems for the Special Functions of Mathematical Physics*, (Chelsea, New York, 1949) (translated from the German by J. Wermer), p. 118.
42. M. Makino, T. Kamimura, and T. Taniuti, *J. Phys. Soc. Jpn.* **50**, 980 (1981).
43. P. S. Marcus, *J. Fluid Mech.* **215**, 393 (1990).
44. J. C. McWilliams and N. J. Zabusky, *Geophys. Astrophys. Dynam.* **19**, 207 (1982).
45. S. D. Meyers, J. Sommeria and H. L. Swinney, *Physica D* **37**, 515 (1989).
46. J. D. Meiss and W. Horton, *Phys. Rev. Lett.* **48**, 1362 (1982).
47. J. D. Meiss and W. Horton, *Phys. Fluids* **25**, 1838 (1982).
48. J. D. Meiss and W. Horton, *Phys. Fluids* **26**, 990 (1983).
49. L. A. Mikhailovskaya, *Fiz. Plazmy* **12**, 879 (1986), [*Sov. J. Plasma Phys.* **12**, 507 (1986)].
50. A. B. Mikhailovskii, G. D. Aburdzheniya, O. G. Onishchenko, and S. E. Sharpov, *Phys. Lett.* **100A**, 503 (1984).
51. A. B. Mikhailovskii, G. D. Aburdzheniya, O. G. Onishchenko, and A. P. Churikov, *Phys. Lett.* **101A**, 263 (1984).
52. D. Montgomery, L. Turner, and G. Vahala, *Phys. Fluids* **21**, 757 (1978).
53. P. J. Morrison, J. D. Meiss, and J. R. Cary, *Physica* **11D**, 324 (1984).

54. P. J. Morrison and R. D. Hazeltine, *Phys. Fluids* **27**, 886 (1984).
55. A. Muhm, A. M. Pukhov, K. H. Spatschek, and V. Tsytovich, *Comments Plasma Phys. Controlled Fusion* **14**, 287 (1991).
56. A. Muhm, A. M. Pukhov, K. H. Spatschek, and V. Tsytovich, *Phys. Fluids B* **4**, 336 (1992).
57. M. V. Nezlin, *Usp. Fiz. Nauk* **150**, 3 (1986), [*Sov. Phys. Usp.* **29**, 807 (1986)].
58. J. Nycander, *Phys. Fluids B* **1**, 1788 (1989).
59. E. A. Overman and N. J. Zabusky, *Phys. Fluids* **25**, 1297 (1982).
60. V. P. Pavlenko and V. I. Petviashvili, *Sov. J. Plasma Phys.* **9**, 603 (1983).
61. V. P. Pavlenko and V. B. Tazanov, *Zh. Eksp. Teor. Fiz.* **91**, 517 (1986), [*Sov. Phys. JETP* **64**, 304 (1986)].
62. J. Pedlosky, *Geophysical Fluid Dynamics*, (Springer Verlag, New York, 1979), pp. 38-42.
63. V. I. Petviashvili, *Fiz. Plazmy* **3**, 270 (1977), [*Sov. J. Plasma Phys.* **3**, 150 (1977)].
64. V. I. Petviashvili, *Pis'ma Zh. Eksp. Teor. Fiz.* **32**, 632 (1980), [*JETP Lett.* **32**, 619 (1980)].
65. N. A. Phillips, *Tellus* **17**, 295 (1965).
66. G. W. Platzman, *Quart. J. Meteor. Roy. Soc.* **94**, 225 (1968).
67. C. G. Rossby, *J. Marine Res.* **2**, 38 (1939).

- 68. R. Z. Sagdeev, V. D. Shapiro, and V. I. Shevchenko, *Sov. Astro. Lett.* **7**, 279 (1981).
- 69. C. E. Seyler Jr., Y. Salu, D. Montgomery, and G. Knorr, *Phys. Fluids* **18**, 803 (1975).
- 70. P. K. Shukla, D. Anderson, M. Lidak and H. Wilhelmsson, *Phys. Rev. A* **31**, 1946 (1985).
- 71. P. K. Shukla, K. H. Spatschek, and R. Balescu, *Phys. Lett.* **107A**, 461 (1985).
- 72. P. K. Shukla, M. Y. Yu, and R. A. Varma, *Phys. Fluids* **28**, 1719 (1985).
- 73. P. K. Shukla, M. Y. Yu, and R. A. Varma, *Phys. Lett.* **109A** 322, (1985).
- 74. J. Sommeria, S. D. Meyers and H. L. Swinney, *Nature* **331**, 689 (1988).
- 75. K. H. Spatschek, E. W. Laedke, Chr. Marquardt, S. Musher, and H. Wenk, *Phys. Rev. Lett.* **64**, 3027 (1990).
- 76. X. N. Su, W. Horton, P. J. Morrison and V. P. Pavlenko, *Effect of Scalar Nonlinearity on the Dipole Vortex Solution*, Univ. of Texas IFS Rept.# 328, (1988).
- 77. X. N. Su, W. Horton, and P. J. Morrison, *Phys. Fluids B* **3**, 921 (1991).
- 78. X. N. Su, W. Horton, and P. J. Morrison, *Phys. Fluids B* **4**, 1238 (1992).

- 79. C. M. Surko and R. E. Slusher, *Phys. Rev. Lett.* **40**, 400 (1983).
- 80. T. Tajima, W. Horton, P. J. Morrison, J. Schutkeker, T. Kamimura, K. Mima, and Y. Abe, *Phys. Fluids B* **3**, 938 (1991).
- 81. T. Taniuti and A. Hasegawa, *Physica Scripta* **T2/2**, 529 (1982).
- 82. C. Temperton, *J. Comput. Phys.* **19**, 317 (1975).
- 83. P. W. Terry and W. Horton, *Phys. Fluids* **26**, 106 (1983).
- 84. V. N. Tsytovich and P. K. Shukla, *Comments Plasma Phys. Controlled Fusion*, **14**, 217 (1991).
- 85. M. Wakatani and A. Hasegawa, *Phys. Fluids* **27**, 611 (1984).
- 86. G. P. Williams, *J. Atmos. Sci.* **35**, 1399 (1978).
- 87. G. P. Williams, *J. Atmos. Sci.* **42**, 1237 (1985).

